

Washington University in St. Louis

## Washington University Open Scholarship

---

All Theses and Dissertations (ETDs)

---

1-1-2011

### Mechanisms of Brain Region-Specific Amyloid-beta Deposition

Adam Bero

*Washington University in St. Louis*

Follow this and additional works at: <https://openscholarship.wustl.edu/etd>

---

#### Recommended Citation

Bero, Adam, "Mechanisms of Brain Region-Specific Amyloid-beta Deposition" (2011). *All Theses and Dissertations (ETDs)*. 553.

<https://openscholarship.wustl.edu/etd/553>

This Dissertation is brought to you for free and open access by Washington University Open Scholarship. It has been accepted for inclusion in All Theses and Dissertations (ETDs) by an authorized administrator of Washington University Open Scholarship. For more information, please contact [digital@wumail.wustl.edu](mailto:digital@wumail.wustl.edu).

WASHINGTON UNIVERSITY IN ST. LOUIS

Division of Biology and Biomedical Sciences

Neurosciences

Dissertation Examination Committee:

David M. Holtzman, Chairperson

David L. Brody

Marc I. Diamond

Jin-Moo Lee

Steve Mennerick

Marcus E. Raichle

Mechanisms of Brain Region-Specific Amyloid- $\beta$  Deposition

by

Adam William Bero

A dissertation presented to the  
Graduate School of Arts and Sciences  
of Washington University in  
partial fulfillment of the  
requirements for the degree  
of Doctor of Philosophy

December 2011

Saint Louis, Missouri

copyright by

Adam William Bero

2011

## ABSTRACT OF THE DISSERTATION

### Mechanisms of Brain Region-Specific Amyloid- $\beta$ Deposition

by

Adam William Bero

Doctor of Philosophy in Neurosciences

Washington University in St. Louis, 2011

David M. Holtzman, M.D., Chairperson

Alzheimer's disease (AD) is the most common cause of dementia. A fundamental feature of AD is brain region-specific deposition of extracellular amyloid plaques principally comprised of the amyloid- $\beta$  (A $\beta$ ) peptide. Using mouse models of cerebral A $\beta$  deposition, we examined molecular, cellular and systems-level mechanisms that regulate brain region-specific A $\beta$  accumulation and aggregation. Parallel studies using *in vivo* multiphoton microscopy and *in vivo* microdialysis revealed that modest pharmacological reduction of soluble interstitial fluid (ISF) A $\beta$  levels was associated with a dramatic reduction in amyloid plaque formation and growth. We found that ISF A $\beta$  concentrations in several brain regions of APP transgenic mice prior to the onset of plaque deposition were proportional to the degree of subsequent plaque deposition and with the concentration of lactate, a marker of neuronal activity. Moreover, we found that physiological modulation of endogenous neuronal activity by vibrissal manipulation was sufficient to modulate ISF A $\beta$  levels and amyloid plaque growth dynamics. Using a

novel optical intrinsic signal imaging approach, we found that bilateral functional connectivity magnitude in APP/PS1 mice prior to plaque deposition was proportional to the amount of regional plaque deposition in aged APP/PS1 mice. Furthermore, we found that bilateral functional connectivity was reduced in normal aging and was markedly exacerbated by A $\beta$  deposition. Together, these data suggest that endogenous neuronal activity and functional connectivity may regulate region-specific A $\beta$  plaque deposition. These data advance our understanding of the mechanisms by which the intrinsic metabolic and functional organization of the brain may contribute to AD pathogenesis.

## **Acknowledgements**

I would first like to acknowledge the enthusiastic support and guidance I have received from my mentor, David Holtzman, throughout the duration of my thesis work. Dave, it has been an honor to count myself as a graduate student in your lab. Thanks for everything.

I would like to thank the National Institutes of Health and the Hope Center for Neurological Disorders at Washington University School of Medicine for generous financial support of the work described herein.

I am indebted to all members of my thesis committee for their valuable contributions to the experiments described herein as well as my professional and scientific development. Specifically, Marc Raichle has inspired me to think beyond disciplinary boundaries and our discussions never failed to lift my spirits.

I am also grateful for the mentorship I received from Dr. Cara Wellman during my undergraduate career at Indiana University. Cara served as my Honors Thesis mentor at IU and holds the (perhaps dubious) distinction of sparking my interest in basic neuroscience research.

To the members of the Holtzman lab, thank you for the conversations, the arguments and the laughs. Joe and Philip, I will miss our discussions (both academic and absurd) and our nights spent “celebrating”. Cheers, Goodfellows.

The friendships I have made during my graduate student career have lessened the collective blow of many failed experiments. Until the day amyloid deposits overwhelm

my cognitive reserve, I will not forget the holiday parties, the float trips or the impromptu happy hours.

To Cailin, our relationship has meant the world to me. Over the last 5 years, you have made every good moment better and every bad moment tolerable. I love you.

The unconditional love and support of my family has been a constant in my life. My parents instilled in me the value of a strong work ethic and self-belief that have catalyzed my academic success. And Zack, thanks for helping to preserve my humility and what remains of my social aptitude. I dedicate this thesis to my family.

<b>Table of Contents</b>	<b>Page</b>
Abstract of the dissertation .....	ii
Acknowledgements.....	iv
Table of Contents.....	vi
Figure list.....	viii
Publication list.....	xi

## **Chapter 1. Introduction and Perspective**

Alzheimer's disease.....	2
Amyloid- $\beta$ peptide and amyloid plaque deposition.....	3
Mouse models of A $\beta$ plaque deposition.....	5
Neuronal activity and ISF A $\beta$ metabolism.....	7
Default-mode network and A $\beta$ deposition.....	9
Functional connectivity and A $\beta$ deposition.....	11

## **Chapter 2. Characterizing the appearance and growth of amyloid plaques in APP/PS1 mice**

Preface.....	14
Abstract.....	15
Introduction.....	16
Materials and Methods.....	18
Results.....	25
Discussion.....	30
Figures.....	34

## **Chapter 3. Neuronal activity regulates the regional vulnerability to amyloid- $\beta$ deposition**

Preface.....	52
Abstract.....	53
Introduction.....	54
Materials and Methods.....	56
Results.....	65
Discussion.....	75

Figures.....	80
--------------	----

#### **Chapter 4. Bidirectional relationship between functional connectivity and amyloid- $\beta$ deposition in mouse brain**

Preface.....	96
Abstract.....	97
Introduction.....	98
Materials and Methods.....	100
Results.....	106
Discussion.....	110
Figures.....	114

#### **Chapter 5. Conclusions and future directions**

Summary.....	122
Super-resolution examination of AD pathogenesis.....	125
Mechanisms of functional connectivity disruption in AD.....	127
Concluding remarks.....	130
<b>References.....</b>	<b>131</b>

<b>Figure list</b>	<b>Page</b>
2.1 Serial <i>in vivo</i> multiphoton microscopy demonstrates growth of individual amyloid plaques.....	34
2.2 Amyloid plaques exhibit age- and size-related growth under thinned-skull window preparations.....	35
2.3 Open-skull cranial window preparations are associated with extensive gliosis.....	37
2.4 $\gamma$ -secretase inhibition suppresses plaque growth and new plaque formation.....	39
2.5 $\gamma$ -secretase inhibition reduces plaque load in 6 month-old APP/PS1 mice.....	41
2.6 $\gamma$ -secretase inhibition results in modest decreases in ISF A $\beta$ levels in cortex.....	42
S2.1 Schematic representation of open- and thinned-skull cranial window preparations.....	44
S2.2 Laser power does not affect plaque size determination.....	45
S2.3 Ten month-old APP/PS1 mice do not exhibit significant average plaque growth.....	47
S2.4 Frequency distribution plots indicate that plaque growth dynamics are related to animal age and skull window preparation.....	48
S2.5 $\gamma$ -secretase inhibition does not alter plaque growth in 10 month-old APP/PS1 mice.....	49
S2.6 Compound E transiently reduces ISF A $\beta$ concentration.....	50
3.1 Distribution of A $\beta$ and amyloid plaque deposition in Tg2576 mouse brain.....	80

3.2	Steady-state ISF A $\beta$ concentrations in young Tg2576 mice before plaque deposition are associated with the level of region-specific plaque deposition in aged Tg2576 mice.....	81
3.3	Neuronal activity regulates ISF lactate concentration <i>in vivo</i> .....	83
3.4	Steady-state ISF lactate levels in young Tg2576 mice are closely associated with regional ISF A $\beta$ levels in young Tg2576 mice and plaque deposition in aged Tg2576 mice.....	84
3.5	Vibrissal activity regulates ISF A $\beta$ levels <i>in vivo</i> .....	85
3.6	Diurnal fluctuation of ISF A $\beta$ is closely associated with ISF lactate levels.....	87
3.7	Vibrissal deprivation reduces amyloid plaque growth and formation <i>in vivo</i> .....	88
S3.1	Regional ISF A $\beta$ and lactate levels in wild-type (B6SJL) mice.....	89
S3.2	Time course of picrotoxin and tetrodotoxin treatment on ISF A $\beta_{x-40}$ and lactate levels in hippocampus.....	90
S3.3	ISF A $\beta_{x-40}$ clearance rates across brain regions of young Tg2576 mouse brain.....	91
S3.4	APP expression and processing are not associated with regional ISF A $\beta$ levels or plaque deposition.....	92
S3.5	Glial activation in barrel cortex following long-term vibrissae deprivation.....	94
4.1	fcOIS reveals regional differences in bilateral functional connectivity magnitude in APP/PS1 mice prior to A $\beta$ plaque deposition.....	114
4.2	fcOIS reveals regional differences in bilateral functional connectivity magnitude in young wild-type mice .....	115
4.3	Regional bilateral functional connectivity magnitude in young APP/PS1	

	mice is closely associated with regional plaque deposition in older APP/PS1 mice .....	116
4.4	A $\beta$ plaque deposition is associated with decreased functional connectivity magnitude in multiple brain systems of older APP/PS1 mice.....	118
4.5	Normal aging is associated with decreased functional connectivity magnitude in retrosplenial cortex.....	119
4.6	Regional A $\beta$ plaque deposition is associated with degree of age-related decline in bilateral functional connectivity.....	120

## Publication list

1. **Bero AW\***, Bauer AQ\*, Stewart FR, White BR, Cirrito JR, Raichle ME, Culver JP, Holtzman DM (in preparation) Bidirectional relationship between functional connectivity and amyloid- $\beta$  deposition in mouse brain.  
\*These authors contributed equally to this work
2. **Bero AW**, Yan P, Roh JH, Cirrito JR, Stewart FR, Raichle ME, Lee JM, Holtzman DM (2011) Neuronal activity regulates the regional vulnerability to amyloid- $\beta$  deposition. *Nat Neurosci* 14(6):750-6
3. Zeng LH, **Bero AW**, Zhang B, Holtzman DM, Wong M (2010) Modulation of astrocyte glutamate transporters decreases seizures in a mouse model of Tuberous Sclerosis Complex. *Neurobiol Dis* 37(3):764-71
4. Yan P\*, **Bero AW\***, Cirrito JR, Xiao Q, Hu X, Wang Y, Gonzales E, Holtzman DM, Lee JM (2009) Characterizing the appearance and growth of amyloid plaques in APP/PS1 mice. *J Neurosci* 29(34):10706-14  
\*These authors contributed equally to this work
5. Yuede CM, Zimmerman SD, Dong H, Kling MJ, **Bero AW**, Holtzman DM, Timson BF, Csernansky JG (2009) Effects of voluntary and forced exercise on plaque deposition, hippocampal volume, and behavior in the Tg2576 mouse model of Alzheimer's disease. *Neurobiol Dis* 35(3):426-32

## **Chapter 1.**

### **Introduction and perspective**

## **Alzheimer's disease**

Alzheimer's disease (AD) is the most common cause of dementia. It is estimated that over 26 million individuals worldwide suffer from AD, including over 10% of individuals  $\geq 65$  years of age and nearly 50% of individuals  $\geq 85$  years of age (Thies and Bleiler, 2011). Given that no treatment that halts or reverses the progression of AD is available, and that the number of AD cases and associated costs are projected to quadruple by the year 2050, a greater understanding of the molecular mechanisms of AD pathogenesis is urgently needed.

Short-term memory dysfunction is an early and essential feature of cognitive decline in AD. At initial clinical presentation, short-term memory dysfunction is typically accompanied by deficits in executive function, attention and problem-solving. As the disease progresses into successive stages of severity, changes such as personality alteration, language dysfunction and a reduced capacity to perform activities of daily living gradually emerge. Following the onset of clinical symptoms, the time course of AD dementia averages 7-10 years and culminates uniformly in death.

The first reported case of AD was described by Alois Alzheimer at the 37<sup>th</sup> Conference of South-West German Psychiatrists in Tübingen, Germany in November of 1906. There, Alzheimer described his clinicopathological evaluation of Auguste Deter, a patient who presented with a "peculiar" dementia at 51 years of age. Upon her death at age 55, Alzheimer utilized the Bielschowsky silver impregnation technique to visualize "miliary foci" and "striking changes of the neurofibrils" throughout Deter's cerebral cortex (Alzheimer et al., 1995). These pathologies, later described as amyloid plaques

and neurofibrillary tangles, respectively, constitute the principle neuropathological hallmarks of AD.

### **Amyloid- $\beta$ peptide and amyloid plaque deposition**

Several decades after Alois Alzheimer's initial description, cerebrovascular amyloid deposits and intraparenchymal extracellular amyloid plaques isolated from AD brain were discovered to be principally composed of aggregated forms of the amyloid- $\beta$  ( $A\beta$ ) peptide (Glenner & Wong, 1984; Masters et al., 1985).  $A\beta$  is a 38-43 amino acid peptide of unknown function that is derived from normal metabolism of amyloid precursor protein [APP; (Haass et al., 1992; Seubert et al., 1992; Shoji et al., 1992)]. APP is a type I transmembrane protein that is predominantly expressed in neurons in the central nervous system and is sequentially cleaved by two proteases,  $\beta$ -secretase (Vassar et al., 1999) and  $\gamma$ -secretase (De Strooper et al., 1998), to generate  $A\beta$ . Alternative APP cleavage by the  $\alpha$ -secretase protease occurs within the  $A\beta$  sequence and thus precludes  $A\beta$  generation (Lammich et al., 1999). Intramembranous  $\gamma$ -secretase cleavage of APP at various amino acid residues at the C-terminus of the  $A\beta$  sequence produces  $A\beta$  peptides of varying amino acid length and aggregation propensity. Of these,  $A\beta_{1-40}$  is the most abundant  $A\beta$  species in the brain and cerebrospinal fluid. Present at only 5-10% of the concentration of  $A\beta_{1-40}$ ,  $A\beta_{1-42}$  is nonetheless regarded as the primary pathogenic  $A\beta$  species as it is more hydrophobic and thus more likely to self-aggregate and seed amyloid plaque deposition (Hasegawa et al., 1999; Kim et al., 2007). Under normal conditions,  $A\beta$  is released by neurons in a soluble form and can be measured in the plasma and cerebrospinal fluid of cognitively normal individuals throughout life (Fagan et al., 2006). During AD pathogenesis, soluble  $A\beta$  aggregates into higher-order species such as soluble

oligomers and insoluble amyloid plaques in a concentration-dependent manner (Meyer-Luehmann et al., 2003). Amyloid plaque deposition in AD is associated with myriad types of neurotoxicity, including neuritic dystrophy (Brendza et al., 2005; Meyer-Luehmann et al., 2008), disrupted brain metabolism (Klunk et al., 2004; Sperling et al., 2009), decreased functional connectivity (Supekar et al., 2008; Hedden et al., 2009; Sheline et al., 2010a; Drzezga et al., 2011), neuroinflammation (Bolmont et al., 2008; Meyer-Luehmann et al., 2008), neurofibrillary tangle formation (Bolmont et al., 2007), and synaptic and neuronal loss (Jack et al., 2009).

In the years since the identification of A $\beta$  as the primary constituent of amyloid plaques in AD brain, genetic, biochemical and neurobiological evidence has mounted to suggest that A $\beta$  accumulation and aggregation initiate a pathogenic cascade of molecular events that ultimately culminate in symptomatic AD (Selkoe, 2000; Hardy and Selkoe, 2002). “Sporadic”, “late-onset” (age > 60 years) AD (LOAD) accounts for ~99% of symptomatic AD cases. Of the several genes in which mutations have been reported to modulate susceptibility to LOAD, the apolipoprotein E (*APOE*)  $\epsilon$ 4 allele confers the greatest risk and decreases average age of dementia onset by 10-20 years (Corder et al., 1993; Saunders et al., 1993). In contrast, the *APOE*  $\epsilon$ 2 allele confers protection and reduces risk of LOAD development (West et al., 1994). Consistent with the amyloid cascade hypothesis, CSF and amyloid imaging data suggest that cognitively normal middle-aged to elderly *APOE*  $\epsilon$ 4 carriers exhibit lower CSF A $\beta$ <sub>1-42</sub> levels, greater brain amyloid deposition and reduced brain glucose metabolism relative to noncarriers (Reiman et al., 1996; Sunderland et al., 2004; Reiman et al., 2009; Morris et al., 2010).

In a small percentage (~1%) of AD cases (familial AD, FAD), the disease is inherited in a fully-penetrant, autosomal dominant manner and dementia typically manifests between 30 and 60 years of age. Missense mutations in the coding sequence of *APP* were the first mutations identified to segregate with FAD or CAA (Levy et al., 1990; Van Broeckhoven et al., 1990; Goate et al., 1991). Since then, several mutations in *APP*, *PSEN1* and *PSEN2* have been found to result in FAD (Holtzman et al., 2011). Importantly, all identified FAD-linked mutations either increase total A $\beta$  levels, A $\beta$ 42 levels or increase A $\beta$  aggregation propensity (Holtzman et al., 2011).

Using positron emission tomography (PET), amyloid deposition in human brain can be directly assessed *in vivo* through systemic infusion of a radiolabeled compound that readily crosses the blood-brain barrier and binds specifically to amyloid plaques (Klunk et al., 2004). Amyloid deposition in human brain can also be indirectly assessed through analysis of A $\beta$ <sub>1-42</sub> levels in cerebrospinal fluid (CSF); CSF A $\beta$ <sub>1-42</sub> concentration is significantly reduced in AD and likely reflects sequestration of soluble A $\beta$  into parenchymal plaques (Fagan et al., 2006). Furthermore, biomarkers such as high CSF tau/A $\beta$ 42 and elevated brain amyloid deposition are predictive of conversion from cognitive normalcy to very mild dementia (Fagan et al., 2007; Morris et al., 2009; Craig-Schapiro et al., 2010) and from mild cognitive impairment to AD (Hansson et al., 2006). As cerebral amyloid plaque deposition begins 10-15 years prior to the onset of clinical symptoms (Perrin et al., 2009), preclinical detection of amyloid pathology using physiological fluid and neuroimaging biomarkers will likely represent a critical component of future AD diagnosis, treatment and prevention.

### **Mouse models of A $\beta$ plaque deposition**

Identification of mutations that result in FAD has greatly facilitated generation of AD mouse models. Though existing mouse models do not recapitulate the full complement of pathology present in human AD brain (Ashe and Zahs, 2010), they have provided valuable insights into specific components of AD pathogenesis.

Transgenic overexpression of human *APP* containing one or more FAD-linked mutations is sufficient to induce age-related A $\beta$  plaque deposition in mouse brain. One such mouse model, Tg2576 (*APP<sup>swe</sup>*), expresses the 695 amino acid form of human *APP* containing the K670N/M671L FAD mutation under the transcriptional regulation of the hamster prion protein promoter (Hsiao et al., 1996). In Tg2576 mice, transgenic APP expression in neurons and astrocytes is approximately 5.5 fold greater than expression of endogenous murine APP. Parenchymal A $\beta_{1-40}$  and A $\beta_{1-42}$  levels are increased by ~5 and 14-fold, respectively (Hsiao et al., 1996; Kawarabayashi et al., 2001). A $\beta$  plaque deposition begins between 9-10 months of age and is associated with the onset of learning and memory deficits (Hsiao et al., 1996). Importantly, A $\beta$  plaque deposition in Tg2576 mouse brain exhibits regional specificity similar to that observed in human AD brain. Therefore, the Tg2576 mouse model represents a useful tool with which to examine the cellular and molecular mechanisms underlying brain region-specific A $\beta$  plaque deposition.

Though mutations in *PSEN1* account for the majority of FAD cases (Holtzman et al., 2011), transgenic overexpression of human PSEN1 containing FAD-linked mutations does not induce A $\beta$  plaque deposition in mouse brain. However, coexpression of mutant human *PSEN1* and *APP* transgenes in bitransgenic mice can hasten the onset and rate of cerebral A $\beta$  plaque deposition relative to singly transgenic APP mutant mice (Borchelt et

al., 1997; Holcomb et al., 1998; Lamb et al., 1999; Jankowsky et al., 2004). Accordingly, A $\beta$  plaque deposition begins between 4-5 months of age in *APP<sup>Swe</sup>/PS1 $\Delta$ E9* (APP/PS1) bitransgenic mice. The degree of acceleration of A $\beta$  plaque deposition is proportional to the increase in the A $\beta$  42:40 ratio induced by mutant PSEN1 (Jankowsky et al., 2004). Though the mechanisms are unclear, regional differences in A $\beta$  plaque deposition are less robust in APP/PS1 compared to Tg2576 mice.

### **Neuronal activity and ISF A $\beta$ metabolism**

Following its intracellular generation, A $\beta$  is secreted into the extracellular fluid of the brain in soluble form (Haass et al., 1992; Seubert et al., 1992; Shoji et al., 1992). Given that amyloid plaques are extracellular structures, and that A $\beta$  aggregation is concentration-dependent (Hasegawa et al., 1999; Meyer-Luehmann et al., 2003), the concentration of soluble A $\beta$  within the brain extracellular fluid is hypothesized to represent a key determinant of whether and when A $\beta$  will aggregate *in vivo*. Therefore, several reports have sought to elucidate the mechanisms that regulate A $\beta$  release into the brain extracellular fluid. In 1992, two reports demonstrated that pharmacological activation of cell-surface M1 or M3 muscarinic acetylcholine receptor subtypes increased release of APP derivatives in cell culture (Buxbaum et al., 1992; Nitsch et al., 1992). In the following year, these findings were extended by the demonstration that electrical depolarization of rat hippocampal slices increased release of APP derivatives and that electrical stimulation-induced APP derivative release was prevented by the addition of tetrodotoxin, a voltage-gated sodium channel blocker (Nitsch et al., 1993). Using APP transgenic mice and rat organotypic hippocampal slices infected with human APP, Kamenetz and colleagues later showed that a pharmacological increase of neuronal

activity by picrotoxin, a GABA<sub>A</sub> receptor antagonist, increased A $\beta$  generation and secretion while a decrease in neuronal activity by tetrodotoxin decreased A $\beta$  generation and secretion (Kamenetz et al., 2003). However, the role of neuronal activity in A $\beta$  formation and secretion *in vivo* remained unknown.

To test the hypothesis that neuronal activity directly regulates A $\beta$  secretion into the extracellular fluid *in vivo*, Cirrito and colleagues in our laboratory utilized a novel A $\beta$  microdialysis technique (Cirrito et al., 2003) to sample A $\beta$  concentration in the brain interstitial fluid (ISF) of awake, behaving mice while performing electrical or pharmacological manipulation of neuronal activity (Cirrito et al., 2005). Consistent with findings showing that APP is axonally transported from entorhinal cortex to hippocampus via the perforant pathway (Buxbaum et al., 1998), and that perforant pathway lesions reduce hippocampal A $\beta$  plaque deposition in APP transgenic mice (Lazarov et al., 2002; Sheng et al., 2002), Cirrito and colleagues found that acute electrical stimulation of the perforant pathway increased ISF A $\beta$  levels in hippocampus of APP transgenic mice within minutes (Cirrito et al., 2005). Moreover, they found that hippocampal infusion of tetrodotoxin via reverse microdialysis reversibly reduced ISF A $\beta$  and EEG amplitude and that pharmacological inhibition of synaptic vesicle exocytosis via tetanus toxin reduced ISF A $\beta$  levels. Finally, they used organotypic hippocampal slice culture to show that stimulation of synaptic vesicle exocytosis increased ISF A $\beta$  levels in the absence of action potentials, suggesting that synaptic activity directly regulates ISF A $\beta$  concentration *in vivo* (Cirrito et al., 2005). Consistent with *in vitro* reports showing that cell-surface APP is internalized by clathrin-mediated endocytosis (Nordstedt et al., 1993) and that APP is cleaved by  $\beta$ -secretase and  $\gamma$ -secretase within early and late endosomes to produce

A $\beta$  (Vassar et al., 1999; Lah and Levey, 2000), the majority (~70%) of synaptic A $\beta$  secretion *in vivo* was later demonstrated to require clathrin-mediated endocytosis (Cirrito et al., 2008).

Recent reports from our laboratory have demonstrated that certain behavioral and environmental manipulations regulate ISF A $\beta$  levels at least in part through modulation of neuronal activity. For instance, acute and chronic restraint stress increase hippocampal ISF A $\beta$  levels in APP transgenic mice and stress-induced increases in ISF A $\beta$  levels are prevented by local infusion of tetrodotoxin (Kang et al., 2007). Consistent with previous reports suggesting that wakefulness is associated with increased cerebral glucose utilization and synaptic potentiation compared to sleep (Vyazovskiy et al., 2008b; Vyazovskiy et al., 2008a; Gilestro et al., 2009), our laboratory has also demonstrated that hippocampal ISF A $\beta$  levels exhibit diurnal fluctuation in both APP transgenic and wild-type mice (Kang et al., 2009). Moreover, acute sleep deprivation increases ISF A $\beta$  levels in hippocampus while chronic sleep deprivation exacerbates A $\beta$  plaque deposition (Kang et al., 2009). However, whether physiological neuronal activity regulates ISF A $\beta$  levels remains unclear.

### **Default-mode network and A $\beta$ deposition**

Much of the knowledge gained from human neuroimaging comes from experiments in which a task-induced change in neural activation is measured relative to a resting-state control condition. Using this approach, one can visualize localized stimulus-induced changes in brain activation and thus relate brain topography to function (Petersen et al., 1988; Buckner et al., 1999). However, given that the resting human brain

consumes 20% of the body's energy and that task-related increases in brain activation are minor (< 5%) relative to resting brain metabolism, most of the knowledge gained from human neuroimaging comes from examination of a small fraction of total brain activity. Indeed, an early study of cerebral energy metabolism found no significant change in global brain metabolism during performance of a challenging arithmetic problem relative to a quiet resting state (Sokoloff et al., 1955).

In cognitively normal adults, it is now well-established that a specific set of brain regions, including medial prefrontal, lateral parietal, posterior cingulate/retrosplenial cortices, is preferentially activated during undirected mentation and is deactivated during task performance. As activity in this neural network is most robust in the absence of a task, this subset of brain regions was termed the “default-mode network” (Raichle et al., 2001; Raichle and Mintun, 2006; Raichle and Snyder, 2007). Activity in the default-mode network is typically ascribed to self-referential thinking, autobiographical memory retrieval and planning for future events (Buckner et al., 2008). Importantly, as resting-state brain metabolism accounts for the majority of total brain metabolism, default-mode network activity is hypothesized to account for the majority of total brain activity.

A fundamental feature of AD is the deposition of extracellular A $\beta$  plaques in specific brain regions. However, the mechanism by which specific brain regions are rendered vulnerable to A $\beta$  plaque deposition in AD remains unknown. To begin to address this issue, Randy Buckner and colleagues used functional magnetic resonance imaging (fMRI) to show that the distribution of resting-state brain metabolism in cognitively normal young adults is closely associated with the topology of amyloid plaque deposition in AD (Buckner et al., 2005). This discovery was recently extended by

data suggesting that the distribution of resting-state aerobic glycolysis (defined as glucose utilization in excess of that used for oxidative phosphorylation despite sufficient oxygen to completely metabolize glucose to carbon dioxide and water) in cognitively normal adult brain is region-specific (Vaishnavi et al., 2010) and that the distribution of resting-state aerobic glycolysis in cognitively normal adults exhibits a strong spatial correlation with amyloid plaque deposition in AD (Vlassenko et al., 2010). However, despite evidence of a close spatial relationship between brain energy metabolism and A $\beta$  deposition in human brain, the mechanisms by which specific brain regions are rendered vulnerable to A $\beta$  plaque deposition in AD remain unknown. Given the near proportionality between neuronal energy consumption and neurotransmitter cycling *in vivo* (Hyder et al., 2006), and given that evidence from our laboratory and others suggests that neuronal activity directly regulates ISF A $\beta$  levels *in vitro* and *in vivo* (Kamenetz et al., 2003; Cirrito et al., 2005; Cirrito et al., 2008), one possibility is that regional differences in resting-state neuronal activity regulate the regional specificity of A $\beta$  plaque deposition through long-term modulation of ISF A $\beta$  concentration.

### **Functional connectivity and A $\beta$ deposition**

In 1995, Biswal and colleagues observed that spontaneous fluctuations in the resting-state BOLD signal measured in left sensorimotor cortex of cognitively normal adults were correlated in time specifically with spontaneous fluctuations in right sensorimotor cortex (Biswal et al., 1995). Such temporal coherence of neural activity in spatially distinct brain regions, termed “functional connectivity”, is now recognized as an intrinsic component of normal brain metabolism (Fox and Raichle, 2007).

Recent large-scale resting-state functional connectivity MRI (fcMRI) and diffuse spectrum imaging data suggest that certain areas of human brain contain disproportionately high levels of functional and structural connectivity (Hagmann et al., 2008; Buckner et al., 2009). Intriguingly, several of these cortical “hubs” are located in regions of the default-mode network. Given that brain regions that comprise the default-mode network are those most susceptible to amyloid plaque deposition in AD, there exists a striking spatial correspondence between areas of elevated resting-state functional connectivity in cognitively normal brain and the pattern of amyloid plaque deposition in AD (Buckner et al., 2009). Moreover, recent reports have demonstrated that functional connectivity within the default-mode network is disrupted in AD (Supekar et al., 2008; Zhang et al., 2009), cognitively normal adults who harbor significant brain amyloid plaque deposition (Hedden et al., 2009; Drzezga et al., 2011) and in normal aging (Andrews-Hanna et al., 2007).

Examination of the relationships between functional connectivity, A $\beta$  plaque deposition and normal aging would be greatly facilitated by the ability to measure systems-level functional connectivity in genetically and pharmacologically tractable model systems. However, given that the small size of mouse brain requires an exceptionally high signal-to-noise ratio to sufficiently resolve region-specific BOLD signal fluctuations, the relationship between functional connectivity, amyloid plaque deposition and normal aging remains unknown.

## **Chapter 2.**

**Characterizing the appearance and growth of amyloid plaques in APP/PS1 mice**

## **PREFACE**

The work in this chapter was published in the August 26, 2009 issue of *The Journal of Neuroscience*. Adam W. Bero and Ping Yan (laboratory of Jin-Moo Lee) contributed equally to this work.

## ABSTRACT

Amyloid plaques are primarily composed of extracellular aggregates of amyloid- $\beta$  (A $\beta$ ) peptide and are a pathological signature of Alzheimer's disease. However, the factors that influence the dynamics of amyloid plaque formation and growth *in vivo* are largely unknown. Using serial intravital multiphoton microscopy through a thinned-skull cranial window in APP/PS1 transgenic mice, we found that amyloid plaques appear and grow over a period of weeks before reaching a mature size. Growth was more prominent early after initial plaque formation: plaques grew faster in 6-month-old compared with 10-month-old mice. Plaque growth rate was also size-related, as smaller plaques exhibited more rapid growth relative to larger plaques. Alterations in interstitial A $\beta$  concentrations were associated with changes in plaque growth. Parallel studies using multiphoton microscopy and *in vivo* microdialysis revealed that pharmacological reduction of soluble extracellular A $\beta$  by as little as 20–25% was associated with a dramatic decrease in plaque formation and growth. Furthermore, this small reduction in A $\beta$  synthesis was sufficient to reduce amyloid plaque load in 6-month-old but not 10-month-old mice, suggesting that treatment early in disease pathogenesis may be more effective than later treatment. In contrast to thinned-skull windows, no significant plaque growth was observed under open-skull windows, which demonstrated extensive microglial and astrocytic activation. Together, these findings indicate that individual amyloid plaque growth *in vivo* occurs over a period of weeks and may be influenced by interstitial A $\beta$  concentration as well as reactive gliosis.

## INTRODUCTION

Amyloid- $\beta$  ( $A\beta$ ) is a 38-43 amino acid peptide that is produced in neurons by the sequential proteolytic cleavage of the amyloid precursor protein (APP) by  $\beta$ -secretase and  $\gamma$ -secretase (Selkoe, 2001). Under normal conditions,  $A\beta$  is secreted into the extracellular space [interstitial fluid (ISF)] of the brain, where it is found in soluble form throughout life (Cirrito et al., 2003). Aggregation of  $A\beta$  into compact amyloid plaques is associated with local neuritic dystrophy (Knowles et al., 1999; D'Amore et al., 2003; Lombardo et al., 2003; Brendza et al., 2005; Garcia-Alloza et al., 2006; Meyer-Luehmann et al., 2008), neuronal and astrocytic calcium dysregulation (Busche et al., 2008; Kuchibhotla et al., 2008; Kuchibhotla et al., 2009) and disruption of cortical synaptic integration (Stern et al., 2004) and is widely considered to represent a necessary factor in Alzheimer's disease (AD) pathogenesis (Hardy and Selkoe, 2002). *In vitro* studies of  $A\beta$  aggregation kinetics demonstrate that  $A\beta$  monomers polymerize to form higher order aggregates in a concentration-dependent manner (Burdick et al., 1992). Although similar aggregation steps are believed to occur during plaque pathogenesis in the AD brain, the dynamics of this process *in vivo* are not well understood. Since amyloid deposits are primarily present in the extracellular space of the brain, the concentration of soluble  $A\beta$  in the ISF is likely a key determinant of  $A\beta$  aggregation. This hypothesis is supported by transplantation studies in which wild-type neural grafts in APP transgenic hosts developed amyloidosis, suggesting that host-derived soluble  $A\beta$  diffused through the ISF and seeded amyloid formation in the graft (Meyer-Luehmann et al., 2003). However, a direct relationship between soluble, extracellular  $A\beta$  and amyloid plaque growth dynamics *in vivo* has not been demonstrated.

Since  $\beta$ -secretase and  $\gamma$ -secretase activity is necessary for A $\beta$  generation, drug discovery efforts have aimed to inhibit these enzymes to halt or reverse the progression of amyloid pathology in AD. However,  $\gamma$ -secretase is also required for the proteolysis of a multitude of other type 1 transmembrane proteins including Notch (De Strooper et al., 1999), ErbB4 (Ni et al., 2001) and CD44 (Lammich et al., 2002). Thus, complete inhibition of this enzyme is associated with significant mechanism-based toxicity, including atrophy of the thymus and altered intestinal cell differentiation (Wong et al., 2004). Interestingly, genetic reduction of  $\gamma$ -secretase activity throughout life by as little as 30% is sufficient to attenuate amyloid pathology in a mouse model of AD while limiting toxicity (Li et al., 2007). However, it is not known whether, and to what extent, transient pharmacological reduction of extracellular A $\beta$  is associated with altered amyloid plaque growth dynamics in adult animals.

Given the overwhelming evidence that A $\beta$  accumulation is necessary for AD pathogenesis, it is critical to understand the mechanisms that govern A $\beta$  plaque formation and growth *in vivo*. To this end, we used serial *in vivo* multiphoton microscopy to monitor the growth of individual plaques over time and *in vivo* microdialysis to determine the relationship between ISF A $\beta$  concentration and amyloid plaque growth in *APP<sup>swe</sup>/PS1 $\Delta$ E9* (APP/PS1) transgenic mice.

## **MATERIALS AND METHODS**

### **Animals.**

Male and female *APP<sup>swe</sup>/PS1<sup>ΔE9</sup>* mice (Jankowsky et al., 2004; Savonenko et al., 2005); APP/PS1; The Jackson Laboratory) were aged to  $6 \pm 0.5$  or  $10 \pm 0.5$  months for multiphoton microscopy experiments and  $3 \pm 0.5$  months for *in vivo* microdialysis experiments. All experimental protocols were approved by the Animal Studies Committee at Washington University.

### **Open-skull cranial window surgery.**

Open-skull cranial windows were prepared on the day of the first imaging session as previously described (Bolmont et al., 2008; Meyer-Luehmann et al., 2008). Briefly, mice were anesthetized under volatile isoflurane (2% induction, 1.5% maintenance), and the skin and periosteum were removed to expose the skull. Lines forming a square (6 mm) were drilled into the skull surface using a high-speed drill (Fine Science Tools), and a pair of angled forceps was used to remove the circumscribed region of skull without damaging the dura mater. A glass coverslip (8 mm in diameter) was placed over the open-skull region and was sealed to the skull with dental cement. A 2-mm-high wall of dental cement was constructed around the coverslip to create a water-immersion chamber for subsequent imaging (supplemental Fig. 1A).

### **Thinned-skull cranial window surgery.**

Thinned-skull cranial windows were prepared on the day of the first imaging session as previously described (Christie et al., 2001; Tsai et al., 2004). Briefly, mice were

anesthetized (as described above), and the skin and periosteum were removed to expose the skull. A high-speed drill and microsurgical blade (Surgistar) were used to thin the skull until the skull window was transparent and displayed flexibility. Pial vasculature was clearly visualized through the window and served as a guide to repeatedly locate the same sites in the brain at subsequent imaging sessions (supplemental Fig. 1B). Two thinned-skull windows (each 0.8–1.0 mm in diameter) were prepared on each animal.

### **Multiphoton microscopy.**

To examine plaque growth, individual plaques were observed longitudinally. Twenty-four hours before each imaging session, animals were injected intraperitoneally with methoxy-X04 (5 mg/ml in 10% DMSO, 45% propylene glycol, and 45% saline), a fluorescent compound that crosses the blood–brain barrier and binds to amyloid plaques (Klunk et al., 2002). The animal was anesthetized and mounted on a custom-built stereotaxic apparatus (Brendza et al., 2005). For thinned-skull window preparations, a small ring of molten bone wax was applied to the skull surrounding the perimeter of the window to create a chamber for water immersion. The skull window was placed directly under the objective lens on a two-photon microscope [LSM 510 META NLO system (Carl Zeiss Inc.) with a Chameleon Ti: Sapphire laser (Coherent Inc.)]. To image methoxy-X04-labeled plaques, two-photon fluorescence was generated with 750 nm excitation, and fluorescent emission was detected in the range of 435–485 nm. A 10× water-immersion objective [numerical aperture (NA) = 0.33, Zeiss] was used to create a site map during initial imaging and a 40× water-immersion objective (NA = 0.75, Zeiss) was used for detailed analysis of individual plaques. A z-stack image series was acquired from the skull surface to a depth of ~200 μm into cortex. Incremental z-step distance was

10  $\mu\text{m}$  under the 10 $\times$  objective and 5  $\mu\text{m}$  under the 40 $\times$  objective. At the conclusion of each imaging session, the animal was removed from the stage and the scalp was sutured. To examine plaque growth over time, the same sites for each animal were imaged on day 0 and day 7, 28, or 90. To determine whether laser intensity might impact plaque size determination, a visual field containing multiple plaques was repeatedly imaged using increasing laser power (14–20%) while detection gain and amplification parameters were held constant (supplemental Fig. 2A,B). No significant differences were found between the different laser intensities.

### **Image analysis.**

Collapsed *z*-stack images for each individual plaque were measured by cross-sectional area and intensity using SigmaScan Pro Image Analysis Software (Systat Software) with a preset threshold (threshold = mean + 4 \* SD) (supplemental Fig. 2C,D). Plaques were excluded from analysis if they were located on the edge of the thinned-skull window, if they exhibited a fluorescence intensity less than the mean intensity of an adjacent background region, or if the images were affected by motion artifacts (from heartbeat or respiration).

### **Double immunofluorescence.**

To compare microglial and astrocytic activation in cortex under open- and thinned-skull window preparations, animals were transcardially perfused with 0.9% saline followed by 4% paraformaldehyde in 0.01 M PBS immediately after the second multiphoton imaging session. Brains were removed and postfixed in 4% paraformaldehyde for an additional 4 h. Coronal free-floating sections (50  $\mu\text{m}$ ) were cut on a cryostat. Sections were incubated

overnight at 4°C in a combination of rabbit anti-Iba1 (1:1000; Wako Chemicals) and mouse anti-GFAP monoclonal antibody (1:1000; Sigma). A secondary antibody mixture of Cy3-conjugated donkey anti-rabbit IgG (1:800; Jackson ImmunoResearch Laboratories) and Alexa Fluor 488-conjugated donkey anti-mouse IgG (1:400; Invitrogen) was applied. Sections were washed, mounted, and examined using a confocal microscope (Zeiss LSM).

### **Compound E treatment.**

To examine the effect of reduced A $\beta$  concentration on plaque growth dynamics, mice were treated with either vehicle or the potent  $\gamma$ -secretase inhibitor, Compound E (3 mg/kg; Axxora) daily for 7 or 28 d (Grimwood et al., 2005). To examine the effect of Compound E on ISF A $\beta$  levels, mice were treated with either a single dose of 3 mg/kg Compound E (i.p.) or treated daily with vehicle or 3 mg/kg Compound E for 7 d.

### **Amyloid plaque load quantification.**

To determine the effect of Compound E treatment on overall cortical amyloid plaque load, 6- and 10-month-old animals were treated with vehicle or Compound E (3 mg/kg, i.p.) daily for 28 d. Mice were subsequently transcardially perfused with 0.9% saline followed by 4% paraformaldehyde in 0.01 M PBS. Brains were dissected, fixed with 4% paraformaldehyde, cryosectioned (50- $\mu$ m-thick slices), and stained with 100  $\mu$ M X-34 in staining buffer (40% ethanol/60% PBS, pH 10) for 20 min and differentiated with staining buffer three times, each, for 2 min to visualize compact plaques (Styren et al., 2000). Cortical plaque load was expressed as percentage of cortical area covered by X-34-positive staining.

### ***In vivo* microdialysis.**

*In vivo* microdialysis used to measure A $\beta$  in the brain ISF of awake, freely behaving mice was performed as previously described (Cirrito et al., 2003; Cirrito et al., 2005; Kang et al., 2007; Cirrito et al., 2008). One day before drug treatment, guide cannulae (BR-style, Bioanalytical Systems) were stereotaxically implanted into the left barrel cortex (at bregma, 2.0 mm lateral to midline, and 1.0 mm below the dura mater at a 32° angle) of APP/PS1 mice under isoflurane volatile anesthesia. After guide cannula implantation, a 2 mm microdialysis probe [BR-2, 38 kDa MWCO (molecular weight cutoff membrane), Bioanalytical Systems] was inserted through the guide cannula so the microdialysis membrane was contained entirely within the barrel cortex. Mice were allowed to recover from anesthesia and were housed in a Return Cage system (Bioanalytical Systems) with *ad libitum* access to food and water for the remainder of the experiment. The microdialysis probe was connected to a syringe pump (Stoelting Co.) and artificial CSF (aCSF), containing (in mM) 1.3 CaCl<sub>2</sub>, 1.2 MgSO<sub>4</sub>, 3 KCl, 0.4 KH<sub>2</sub>PO<sub>4</sub>, 25 NaHCO<sub>3</sub>, and 122 NaCl, pH 7.35, was continuously perfused through the microdialysis probe at a constant flow rate of 0.7  $\mu$ l/min. Artificial CSF contained 0.15% bovine serum albumin to limit nonspecific loss of A $\beta$ . Dialysis samples were collected using a refrigerated fraction collector (SciPro Inc.) into polypropylene tubes for subsequent measurements of A $\beta$ <sub>1-x</sub>, A $\beta$ <sub>x-40</sub>, or A $\beta$ <sub>x-42</sub> by ELISA, as described below. Mice were treated intraperitoneally with either a single dose of Compound E (3 mg/kg) or daily with vehicle or Compound E (3 mg/kg) for 7 d. In single-dose experiments, baseline levels of ISF A $\beta$  were defined as the mean concentration of A $\beta$  8 h before drug treatment. Because artifactual fluctuations in ISF A $\beta$  levels are occasionally observed 3–4 d after insertion of

the microdialysis probe (our unpublished observations), we chose to monitor ISF A $\beta$  levels during days 5, 6, and 7 of treatment in multiple-dose experiments. Based on our finding that ISF A $\beta$  levels collected 16–24 h after a single dose of Compound E did not differ from pretreatment baseline levels, baseline levels of ISF A $\beta$  in multiple-dose experiments were defined as the mean concentration of A $\beta$  from hours 16–24 after each injection of Compound E. After each experiment, animals were killed.

### **A $\beta$ ELISA assay.**

Microdialysis samples were analyzed for A $\beta_{1-x}$ , A $\beta_{x-40}$ , or A $\beta_{x-42}$  using species-specific sandwich ELISAs. Briefly, A $\beta_{1-x}$ , A $\beta_{x-40}$ , and A $\beta_{x-42}$  were captured using monoclonal antibodies targeted against amino acids 13-28 (m266), 35-40 (HJ2), or 33-42 (21F12) of A $\beta$ , respectively. The antibodies m266, 21F12, and 3D6 were gifts from Eli Lilly. For A $\beta_{1-x}$  assays, a biotinylated N-terminal domain monoclonal antibody (3D6B) followed by streptavidin-poly-HRP-20 was used to detect (Fitzgerald). For A $\beta_{x-40}$  and A $\beta_{x-42}$  assays, a biotinylated central domain monoclonal antibody (HJ5.1B) followed by streptavidin-poly-HRP-40 was used to detect (Fitzgerald). All assays were developed using Super Slow ELISA TMB (Sigma) and read on a Bio-Tek FL-600 plate reader at 650 nm.

### **Statistical analysis.**

Longitudinal changes in cross-sectional area of individual plaques were analyzed using paired *t* tests. Differences in average fold increase of amyloid plaques at multiple time points as a function of imaging interval were analyzed using a one-way ANOVA followed by Dunn's *post hoc* test. To assess differences in individual plaque growth as a function of drug treatment, the fold increase of mean plaque size was analyzed using a

paired *t* test (SigmaStat statistical software v 2.0, Systat Software). Group differences in percentage area covered by X-34-positive staining were analyzed by Student's *t* tests. In microdialysis experiments, time point comparisons of ISF A $\beta$  levels were performed using one- and two-way ANOVAs followed by Bonferroni *post hoc t* tests. Differences in mean ISF A $\beta$  levels between groups were compared using a paired *t* test (GraphPad Prism v 4.0). All data in figures represent mean  $\pm$  SEM. In all tests, the level of significance was set at  $p \leq 0.05$ .

## RESULTS

### **Amyloid plaques exhibit age- and size-related growth under thinned-skull windows**

Using serial intravital multiphoton microscopy, individual amyloid plaques were imaged through thinned-skull cranial windows over 7, 28, and 90 d intervals in 6- and 10-month-old APP/PS1 transgenic mice. In 6-month-old mice, plaque size increased significantly over 7, 28, and 90 d intervals (Figs. 1, 2A–C; supplemental Fig. 4A,C). Over a 7 d interval, 21% of plaques grew by at least twofold, with a maximum of fourfold growth (Fig. 2A; supplemental Fig. 4A). Over a 28 d interval, 62% of plaques increased by twofold or more, with a maximum of sixfold growth (Fig. 2B; supplemental Fig. 4A,C). Notably, the average fold increase in plaque size over a 90 d period was no greater than that observed over the 28 d period, suggesting that plaques adopted a stable size before these two imaging time points (Fig. 2C,D; supplemental Fig. 4A). Although the net effect of plaque dynamics indicated average plaque growth, there was a great deal of variability. Indeed, many plaques remained stable during the observed time intervals and rare examples of plaque regression were also evident (supplemental Fig. 4B). In contrast to plaque growth observed in 6-month-old animals, plaques imaged in 10-month-old mice did not exhibit significant growth over 7 or 90 d periods (Fig. 2D). Plaque growth was also related to plaque size, as smaller plaques exhibited a greater growth rate compared with larger plaques regardless of animal age (Fig. 2E). Consistent with these findings, plaques sampled in 6-month-old mice exhibited a smaller mean size than 10-month-old mice and showed greater mean growth (supplemental Fig. 3C). Moreover, newly formed plaques were significantly smaller than preexisting plaques (supplemental Fig. 3D). Thus, individual amyloid plaque growth *in vivo* is related to animal age and plaque size.

## **Open-skull cranial window preparations do not show plaque growth and are associated with extensive gliosis**

In contrast to the robust plaque growth observed under thinned-skull window preparations, plaques imaged in 6-month-old APP/PS1 mice under open-skull cranial window preparations did not exhibit significant growth but did show some evidence of regression over a 28 d interval (Fig. 2*F*; supplemental Fig. 4*C*). These findings are consistent with two recent two-photon studies using open-skull windows (Bolmont et al., 2008; Meyer-Luehmann et al., 2008). Technical differences between the two window types are shown in supplemental Figure 1, and include open (craniotomy)- versus closed-skull preparations, size differences (6 mm diameter in open-skull vs <0.8 mm in closed-skull windows), and the presence of a foreign body (coverslip) in open-skull windows versus none in closed-skull windows. To examine functional consequences of the different cranial window types, we performed a comparative analysis of microglial and astrocytic activation under thinned- and open-skull window preparations. Seven days after open-skull surgery, extensive microglial activation (Iba-1 immunostain, Fig. 3*A*) was present in cortex under the open-skull window, whereas activated microglia were largely absent in the contralateral control hemisphere. Astrocytic activation (GFAP immunostain, Fig. 3*B*) was also abundant in cortex under the open-skull window but rare in contralateral control cortex. Even at low power, extensive immunostaining is visible in the region immediately below the cranial window. In contrast, microglial and astrocytic activation occurred only immediately surrounding plaques under thinned-skull window preparations and was indistinguishable from the respective contralateral control hemispheres (Fig. 3*C,D*). These results indicate that open-skull, but not thinned-skull,

window preparations are associated with extensive cortical gliosis and suggest that reactive glial activation may underlie the suppressed plaque growth dynamics observed under open-skull window preparations. Our findings are consistent with those of Dr. W. G. Bao, who has reported increased gliosis under open-skull windows associated with altered dynamics in synaptic spine behavior (Xu et al., 2007). Thus, for the remaining multiphoton studies, all experiments were performed using thinned-skull windows.

### **$\gamma$ -Secretase inhibition suppresses plaque growth and new plaque appearance *in vivo***

To assess the effects of reduced A $\beta$  production on longitudinal growth of individual plaques, we measured plaque growth in 6- and 10-month-old APP/PS1 mice treated with either the potent  $\gamma$ -secretase inhibitor, Compound E (3 mg/kg), or vehicle daily for 7 or 28 d ( $n = 4$ /group). Compound E suppressed plaque growth in 6-month-old mice over 7 and 28 d intervals (Fig. 4). Treatment for 28 d in 6-month-old animals also dramatically attenuated the appearance of new plaques:  $0.4390 \pm 0.1391$  new plaques per mm<sup>3</sup> in vehicle-treated versus  $0.0506 \pm 0.0339$  in Compound E-treated mice (Student's  $t$  test,  $*p \leq 0.05$ ). In contrast, plaques imaged in 10-month-old mice did not exhibit significant growth over the 7 or 90 d interval regardless of drug treatment (supplemental Fig. 5). Importantly, although Compound E treatment was sufficient to dramatically decrease plaque growth, it did not induce regression in average plaque size.

To determine whether suppressed growth of individual plaques was reflective of changes in overall plaque burden, 6- and 10-month-old APP/PS1 mice were treated with Compound E (3 mg/kg) or vehicle daily for 28 d ( $n = 8$ /group); mice were killed, brains were sectioned and immunostained, and compact plaque load was determined.

Compound E reduced X-34-positive cortical plaque burden by 23% in 6-month-old mice compared with vehicle-treated controls (Fig. 5). No difference was detected in 10-month-old mice, similar to findings recently reported (Garcia-Alloza et al., 2009). These results indicate that modest  $\gamma$ -secretase inhibition was sufficient to decrease amyloid plaque load and size when administered during the plaque growth phase and suggest that longitudinal growth of individual amyloid plaques is a fundamental mechanism by which plaque load increases in AD. Of note, individual plaque growth measured by multiphoton microscopy ( $n = 4$ ) is a much more sensitive measure than average grouped plaque burden measures ( $n = 8$ ).

**Modest reduction in ISF A $\beta$  concentration is associated with a dramatic reduction in amyloid plaque growth *in vivo***

We next performed *in vivo* microdialysis experiments to determine the extent to which this dose of Compound E affects ISF A $\beta$  concentrations. Three-month-old APP/PS1 mice were treated with a single dose of Compound E (3 mg/kg) while cortical *in vivo* microdialysis was performed to directly measure ISF A $\beta$  levels in living mice. Compound E treatment decreased ISF A $\beta_{1-x}$  by 27% during the first 8 h after treatment and had no effect during the remaining 16 h of sample collection ( $n = 6$ ; supplemental Fig. 6A,B). To determine the effect of 7 d treatment with Compound E on ISF A $\beta$ , we treated 3-month-old APP/PS1 mice with Compound E (3 mg/kg) or vehicle for 7 d and performed microdialysis during the final 3 d of drug treatment. Compound E treatment decreased ISF A $\beta_{x-40}$  and A $\beta_{x-42}$  levels by 41% ( $n = 4$ /group) and 44% ( $n = 4$ /group), respectively, during the first 8 h after injection compared with controls (Fig. 6A,B). A $\beta_{x-40}$  and A $\beta_{x-42}$  levels exhibited more modest reductions during hours 8–16 after Compound E

treatment and were no different from controls during the final 8 h after injection (Fig. 6A,B). Expressed as relative levels over a 24 h period, Compound E reduced ISF A $\beta_{x-40}$  levels by 22% ( $n = 4/\text{group}$ ) and A $\beta_{x-42}$  by 25% ( $n = 4/\text{group}$ ) compared with controls (Fig. 6C). Together, these results suggest that a modest decrease in ISF A $\beta$  levels may be sufficient to arrest amyloid plaque growth *in vivo*.

## DISCUSSION

Amyloid plaques, primarily composed of aggregated A $\beta$ , exist in the extracellular space of the brain and are a pathological hallmark of AD. However, the factors that govern the formation and growth of plaques in the living brain are unknown. In the present study, we used serial *in vivo* multiphoton microscopy in APP/PS1 mice to directly quantify amyloid plaque formation and growth *in vivo*. We found that although many plaques remained stable in size at both ages examined, plaques imaged in 6-month-old APP/PS1 mice exhibited robust growth relative to plaques found in 10-month-old mice, suggesting that plaque growth is more prominent early in disease pathogenesis. This finding is consistent with reports of biphasic development of plaque load in APP transgenic mice; compact plaque load is reported to increase with age (Sturchler-Pierrat et al., 1997; Wengenack et al., 2000; Jack et al., 2005; Braakman et al., 2006; Harigaya et al., 2006) before stabilizing at later disease stages (Gordon et al., 2002). Plaque load stabilization has also been hypothesized to occur in human AD patients, as amyloid burden does not correlate with disease duration (Hyman et al., 1993; Engler et al., 2006) and plaque burden in a subset of patients with mild cognitive impairment is indistinguishable from AD patients (Lopresti et al., 2005; Price et al., 2005; Mintun et al., 2006). Our study also indicated that plaque growth was related to plaque size, as smaller plaques exhibited greater rates of growth compared with larger plaques, regardless of age.

We also found that treatment with the  $\gamma$ -secretase inhibitor, Compound E, markedly decreased the appearance of new plaques and growth of preexisting plaques in APP/PS1 mice. This suppression in plaque appearance and growth was reflected in a decrease in total plaque burden in parallel cross-sectional studies. To determine the extent to which

Compound E treatment reduced soluble extracellular A $\beta$  levels *in vivo*, we used *in vivo* microdialysis to measure ISF A $\beta$  levels in APP/PS1 mice treated with Compound E. Chronic dosing of Compound E over a 7 d period decreased ISF A $\beta_{x-40}$  and A $\beta_{x-42}$  levels by only 20–25% over a 24 h period. That reduced extracellular A $\beta$  concentration is associated with inhibition of amyloid plaque growth but not plaque regression is consistent with previous data obtained using transgenic mice that overexpress mutant APP under the regulation of a tetracycline-responsive promoter. Inhibition of mutant APP expression for 6 months after plaque formation arrested the progression of amyloid pathology but did not reduce overall plaque burden (Jankowsky et al., 2005). A more recent report demonstrated that 3 weeks of treatment with an orally active  $\gamma$ -secretase inhibitor did not reduce size of existing plaques in APP/PS1 mice (Garcia-Alloza et al., 2009). Together, these studies suggest that a kinetic disequilibrium between A $\beta$  plaque aggregation and dissociation may exist *in vivo*.

The hypothesis that soluble extracellular A $\beta$  concentration is a key determinant of A $\beta$  aggregation *in vivo* is supported by data demonstrating that areas of the brain that ultimately develop plaque pathology have higher basal ISF A $\beta$  levels early in life relative to brain regions that do not develop pathology (Cirrito et al., 2003). Moreover, intracerebral injection of A $\beta$ -containing brain extract from human AD patients or APP transgenic mice induces cerebral amyloidosis in APP transgenic mice in a concentration-dependent manner (Meyer-Luehmann et al., 2003). Although correlative, the present study is the first demonstration of the relationship between soluble ISF A $\beta$  and amyloid plaque growth *in vivo*. Moreover, it is the first report that this relationship can be modulated with pharmacological intervention. That a modest reduction of ISF A $\beta$  levels

is associated with inhibition of amyloid plaque growth and attenuation of new plaque formation is consistent with recent data demonstrating that a 30% reduction in  $\gamma$ -secretase activity, as seen with knocking out  $\gamma$ -secretase components throughout life, can attenuate plaque burden in a mouse model of AD (Li et al., 2007). Thus, partial  $\gamma$ -secretase inhibition may be sufficient to arrest amyloid plaque progression in AD.

A number of potential therapeutic implications follow from the results of the present study. First, the observation that  $\gamma$ -secretase inhibition can prevent growth of existing plaques and attenuate new plaque formation, but not induce plaque regression suggests that anti-A $\beta$  treatments may be most efficacious if administered early in disease pathogenesis. This hypothesis is supported by our cross-sectional study, showing that 28 d Compound E treatment reduced amyloid plaque load in 6-month-old APP/PS1 mice, but not in 10-month-old mice. Moreover, our finding that a modest reduction in soluble, extracellular A $\beta$  is associated with a dramatic reduction in plaque growth and formation may have important implications for drug dosing and pharmacodynamic effects of anti-A $\beta$  therapeutics to be used in clinical trials.

Our present observations of individual plaque growth over a period of weeks are in contrast to a recent report which showed that plaques reach a mature size within 24 h after appearance (Meyer-Luehmann et al., 2008). We hypothesized that these differences might be due to different techniques used to create transcranial windows. We used a small (<0.8 mm diameter) closed thinned-skull window in our experiments, in contrast to the larger (6 mm diameter) open-skull (craniotomy) window used by Meyer-Luehmann et al. (2008) (see supplemental Fig. 1A,B). A direct comparison of plaque growth using these two techniques revealed robust growth under thinned-skull window preparations,

but no significant growth under open-skull preparations. In addition, the open-skull preparation was associated with extensive cortical microglial and astrocytic activation, which was largely absent under the thinned-skull window. These findings are consistent with a previous comparison of these two techniques, which demonstrated that the open-skull window resulted in significant reactive gliosis and an alteration of dendritic spine dynamics compared with the closed thinned-skull window (Xu et al., 2007). Coupled with previous reports implicating reactive gliosis in plaque size maintenance and regression (Gordon et al., 2002; Wyss-Coray et al., 2003; El Khoury et al., 2007; Takata et al., 2007; Bolmont et al., 2008), this may explain the discrepancy between the findings using the two different techniques.

In summary, our results suggest that individual amyloid plaques grow over a period of weeks and that the rate of plaque growth is related to disease stage, plaque size, gliosis, and soluble extracellular A $\beta$  concentration. Thus, growth of individual plaques may be a fundamental mechanism by which plaque load increases in AD. Furthermore, the present results suggest that a decrease in ISF A $\beta$  levels by as little as 20–25% at key time points in plaque development may be sufficient to prevent the progression of amyloid pathology.

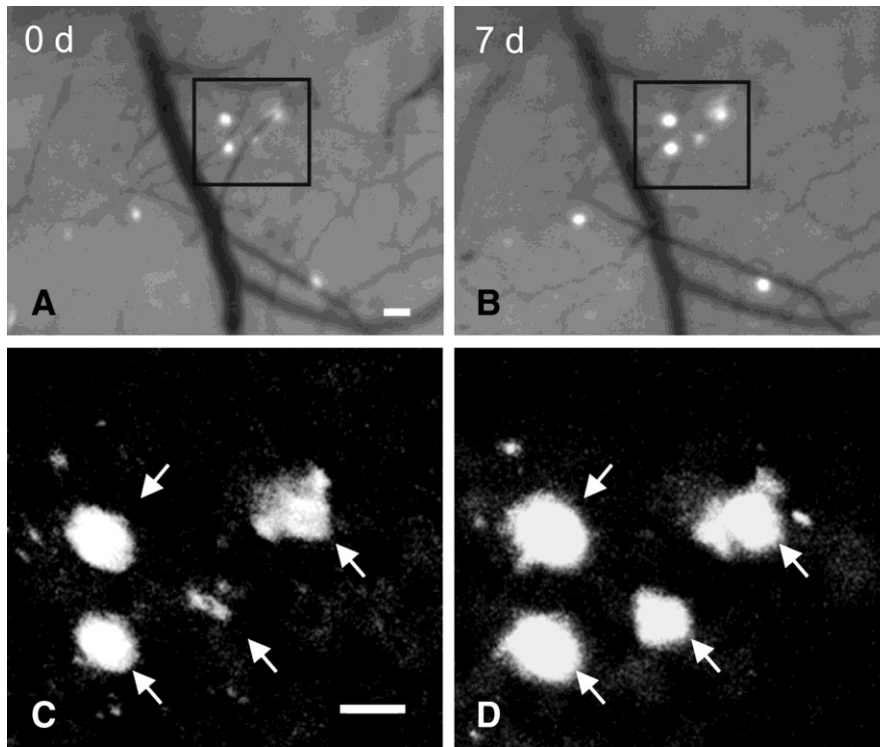


**Figure 1. Serial *in vivo* multiphoton microscopy demonstrates growth of individual amyloid plaques.** (A, B) Epifluorescence micrographs of 4 plaques labeled with methoxy-X04 and imaged over a 7-day interval in the brain of a 6 month-old APP/PS1 mouse. (C, D) Multiphoton micrographs of those same 4 plaques illustrate growth of individual plaques over time. Scale bars: 20 $\mu$ m.

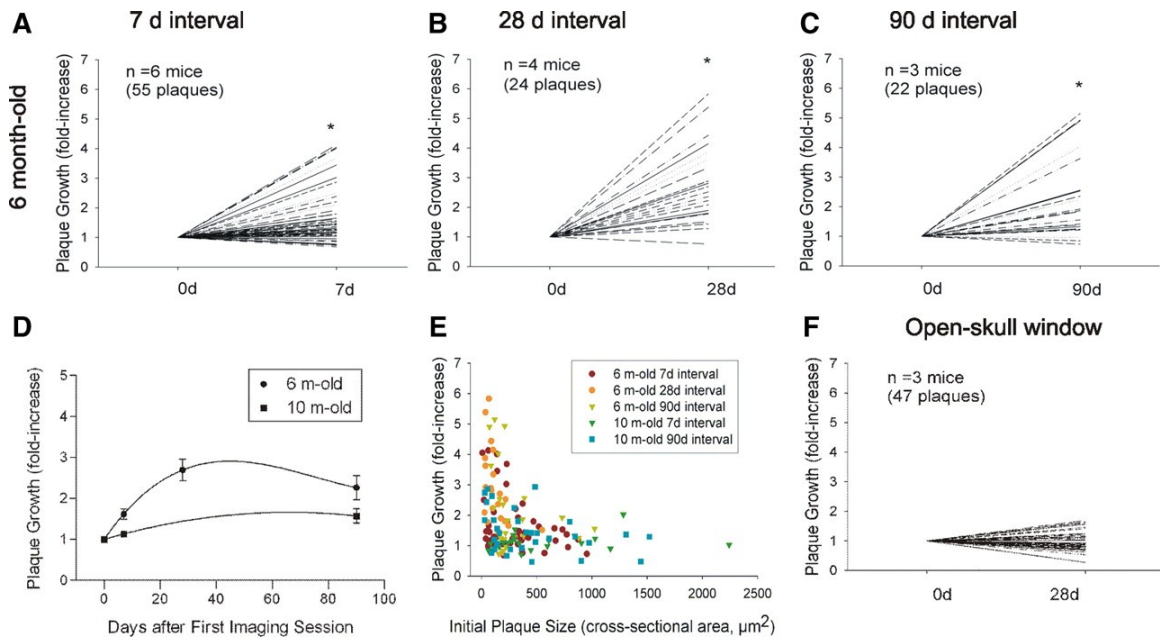


**Figure 2. Amyloid plaques exhibit age- and size-related growth under thinned-skull**

**window preparations.** Using serial intravital multiphoton microscopy, individual

plaques were labeled with methoxy-X04 and imaged at multiple time points. Plaque growth was expressed as fold-increase in cross-sectional area relative to initial plaque

size. (A-C) In 6 month-old APP/PS1 mice, plaques exhibited significant growth over 7-,

28- and 90-day intervals (Paired t-test,  $*=p \leq 0.05$ ). (D) Time course of plaque growth in 6

and 10 month-old mice. In 6 month-old animals, the average fold-increase in plaque size over a 28-day period was significantly greater than that observed over a 7-day period.

There was no difference between average fold-increase over a 28-day period compared to that over a 90-day period (one-way ANOVA followed by Dunn's post-hoc test,

$*=p \leq 0.05$ ). Plaques imaged in 10 month-old animals did not exhibit significant plaque

growth at either the 7- or 90-day interval (Paired t-test). (E) Average plaque growth is

plotted as a function of initial plaque size. Regardless of animal age, smaller plaques

grew at a greater rate compared to larger plaques. (*F*) Plaques imaged in 6 month-old animals under open-skull window preparations did not exhibit significant growth over a 28-day interval.

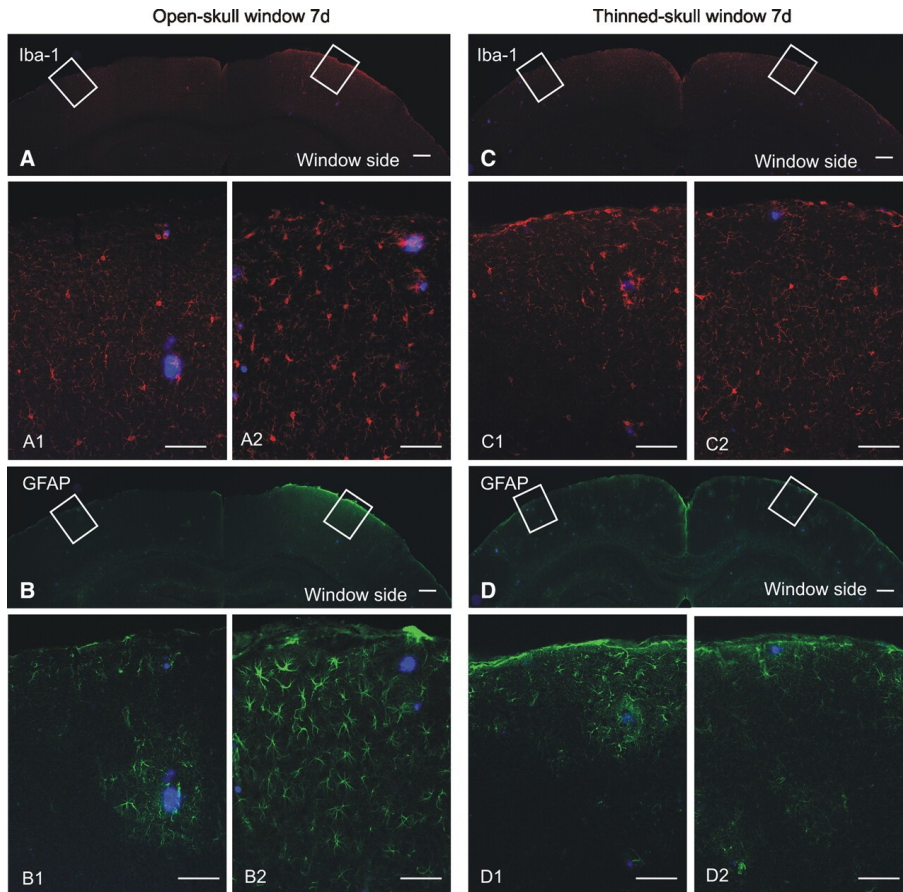


**Figure 3. Open-skull cranial window preparations are associated with extensive gliosis.** (A) Low-magnification image of Iba-1 immunofluorescence (red) illustrates extensive microglial activation in cortex under the open-skull cranial window but not in contralateral control cortex. High-power micrographs colabeled for methoxy-X04-positive plaques (blue) reveal little microglial activation in control hemisphere (A1), but robust microglial activation under the open-skull window (A2). (B) Low magnification image of GFAP immunofluorescence (green) demonstrates extensive activation of astrocytes in cortex under the open-skull cranial window. High-power micrographs illustrate astrocytic activation only in the immediate vicinity of plaques in control cortex

(*B1*), while robust astrocytic activation is present throughout cortex under the open-skull window (*B2*). (*C*) Iba-1-positive microglia are not abundantly visible at low-magnification under a thinned-skull cranial window preparation. High-power micrographs illustrate rare microglial activation in control cortex (*C1*) and under the thinned-skull window (*C2*). (*D*) Astrocytic activation is not robust at low-magnification under a thinned-skull window preparation. Astrocytic activation is rare in control cortex (*D1*) and under the thinned-skull window (*D2*). Scale bars: *A-D*, 200  $\mu\text{m}$ ; *A1-D2*, 50  $\mu\text{m}$ .

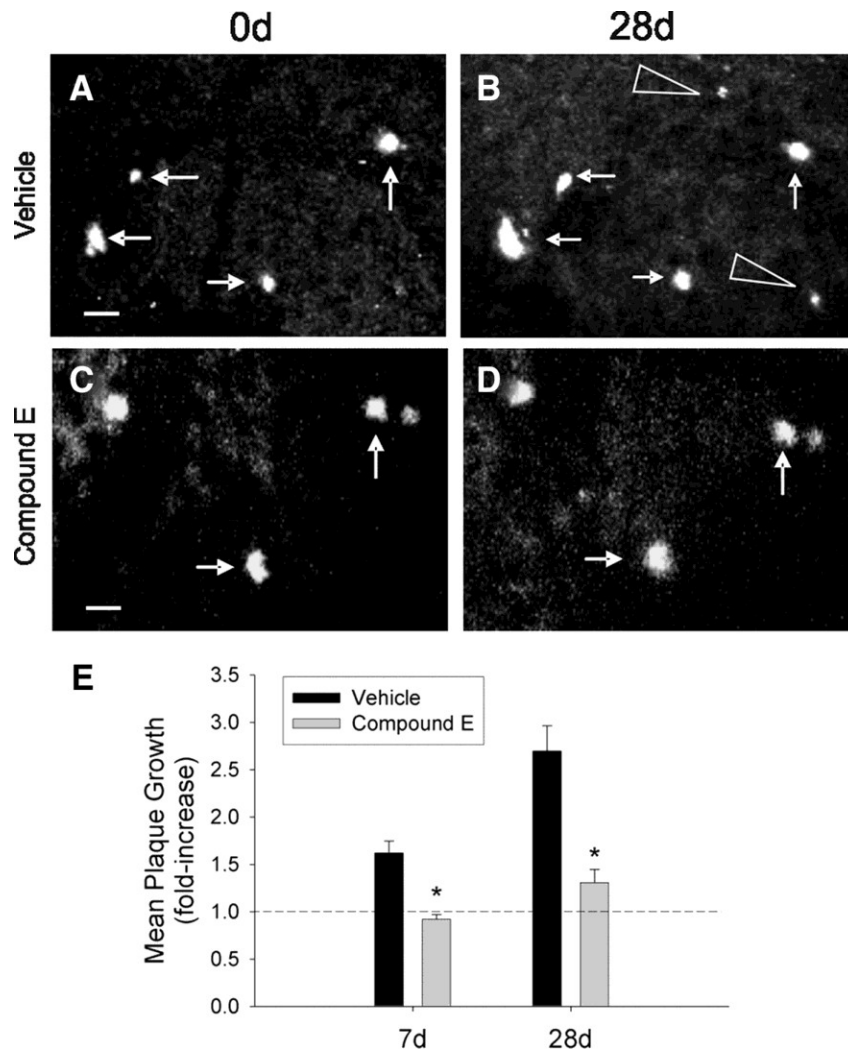


**Figure 4.  $\gamma$ -secretase inhibition suppresses plaque growth and new plaque formation.** (A, B) Representative multiphoton micrographs of plaques imaged at a 28-day interval in a vehicle-treated 6 month-old APP/PS1 mouse illustrate growth of existing plaques (arrows) and appearance of new plaques (arrow heads). (C, D) Plaque growth was suppressed in mice treated with the  $\gamma$ -secretase inhibitor, Compound E (3 mg/kg, i.p). All images are collapsed z-stack images (100-120  $\mu$ m thick). (E) Plaques imaged in vehicle-treated mice exhibited significant growth over 7- and 28-day intervals, while

plaque growth was attenuated in Compound E-treated mice. ( $n=4$  mice/group; Student's t-test, \*  $p \leq 0.05$ ). The dotted line indicates no growth, and scale bars = 20  $\mu\text{m}$ .

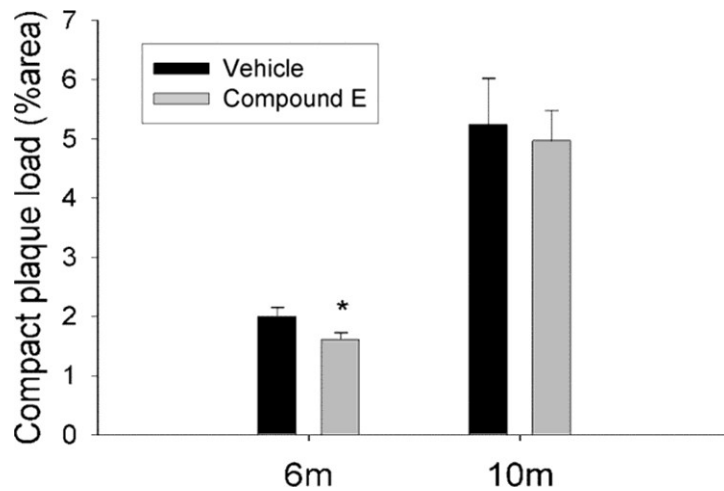


**Figure 5.  $\gamma$ -secretase inhibition reduces plaque load in 6 month-old APP/PS1 mice.**

Six and 10 month-old APP/PS1 mice were treated daily with Compound E (3 mg/kg, i.p.) or vehicle for 28 days. Compound E reduced X-34-positive cortical plaque load by 23% in 6 month-old animals compared to vehicle-treated controls. No difference was present between groups in 10 month-old animals ( $n=8$  mice/group; Student's t-test,  $*=p\leq 0.05$ ).

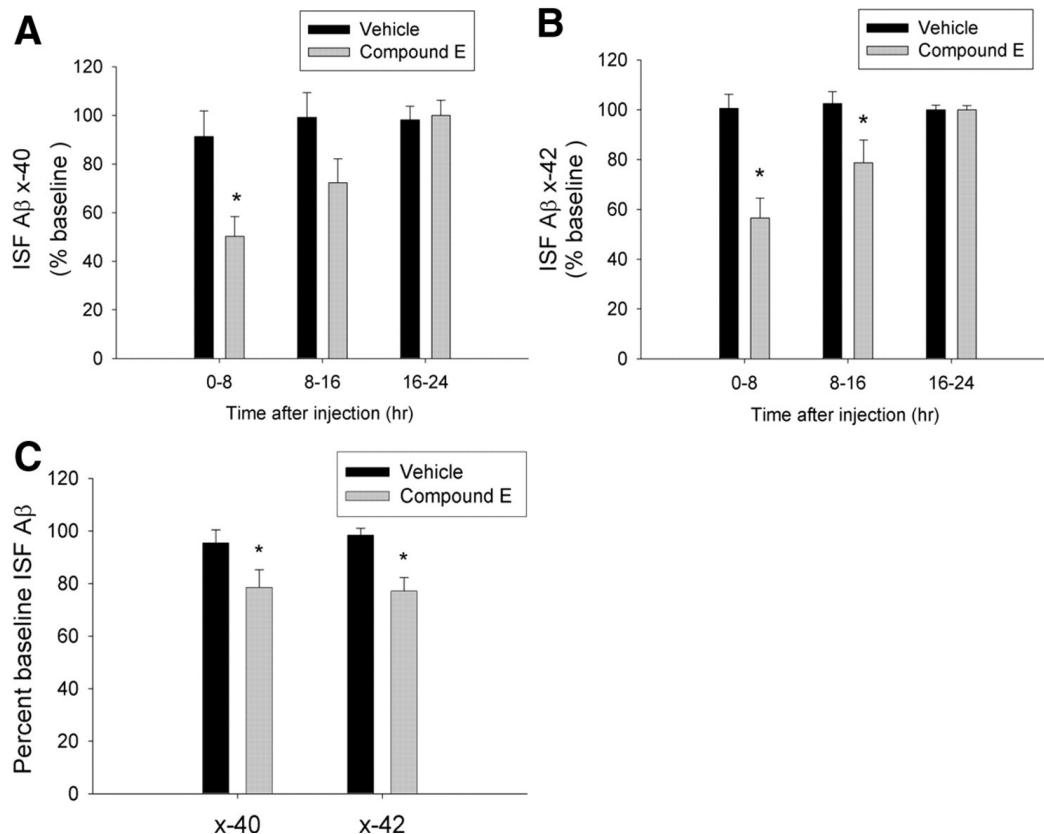
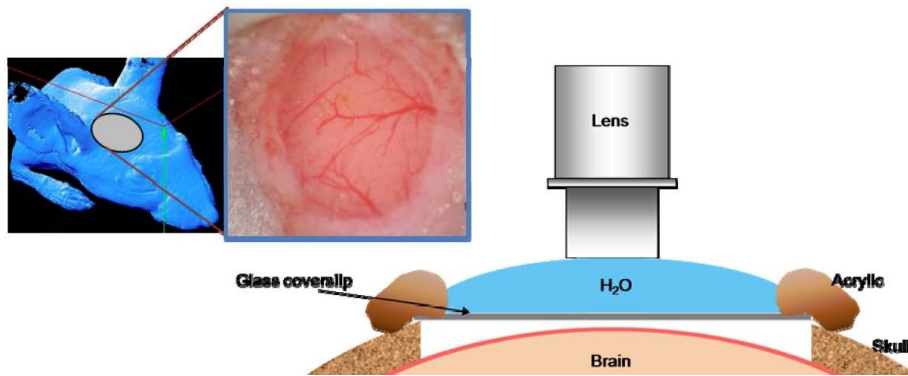


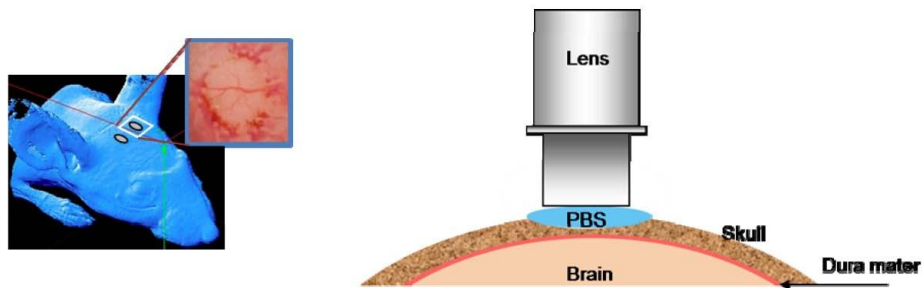
**Figure 6.  $\gamma$ -secretase inhibition results in modest decreases in ISF A $\beta$  levels in cortex.** Three month-old APP/PS1 mice were treated daily with Compound E (3 mg/kg, i.p.) or vehicle for 7 days. *In vivo* microdialysis was performed to measure ISF A $\beta_{x-40}$  and A $\beta_{x-42}$  in cortex throughout the final 3 days of drug treatment. (A, B) Compound E reduced ISF A $\beta_{x-40}$  and A $\beta_{x-42}$  levels by 42% and 44%, respectively, during the first 8 hours after each treatment compared to vehicle-treated controls. ISF A $\beta_{x-40}$  and A $\beta_{x-42}$  exhibited more modest decreases during hours 8-16 after Compound E treatment and were no different from controls during hours 16-24 ( $n=4$ /group, two-way ANOVA with post-hoc Bonferroni tests;  $*=p \leq 0.05$ ). (C) Expressed as relative levels over 24 hours,

mice treated with Compound E for 7 days exhibited a 22% decrease in ISF  $A\beta_{x-40}$  and a 25% decrease in  $A\beta_{x-42}$  compared to controls ( $n=4$ /group; Paired t-test;  $*=p\leq 0.05$ ).

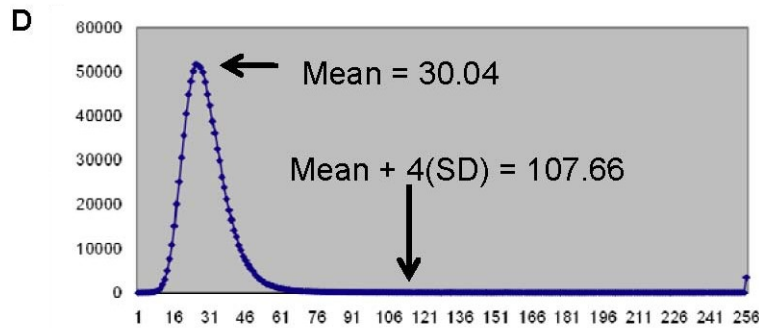
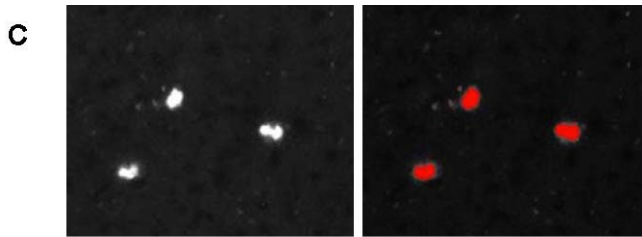
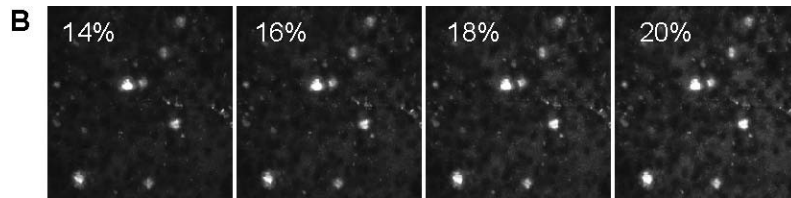
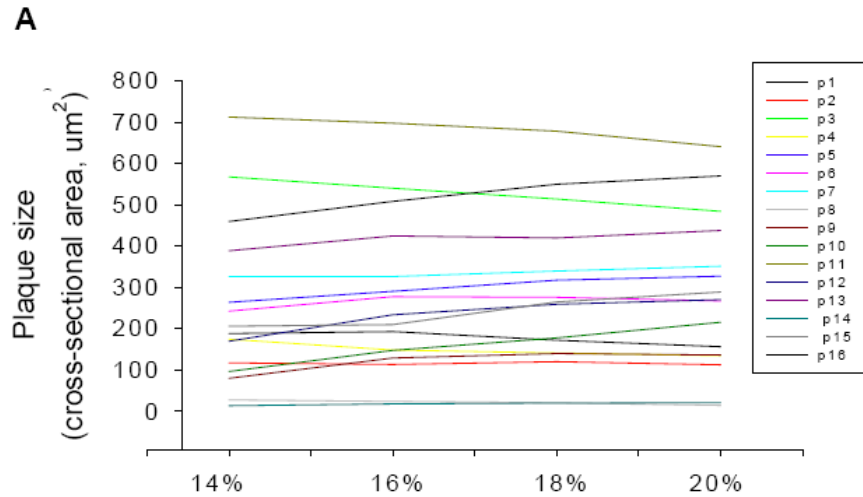
### **A Open-skull cranial window preparation**



### **B Thinned-skull window preparation**



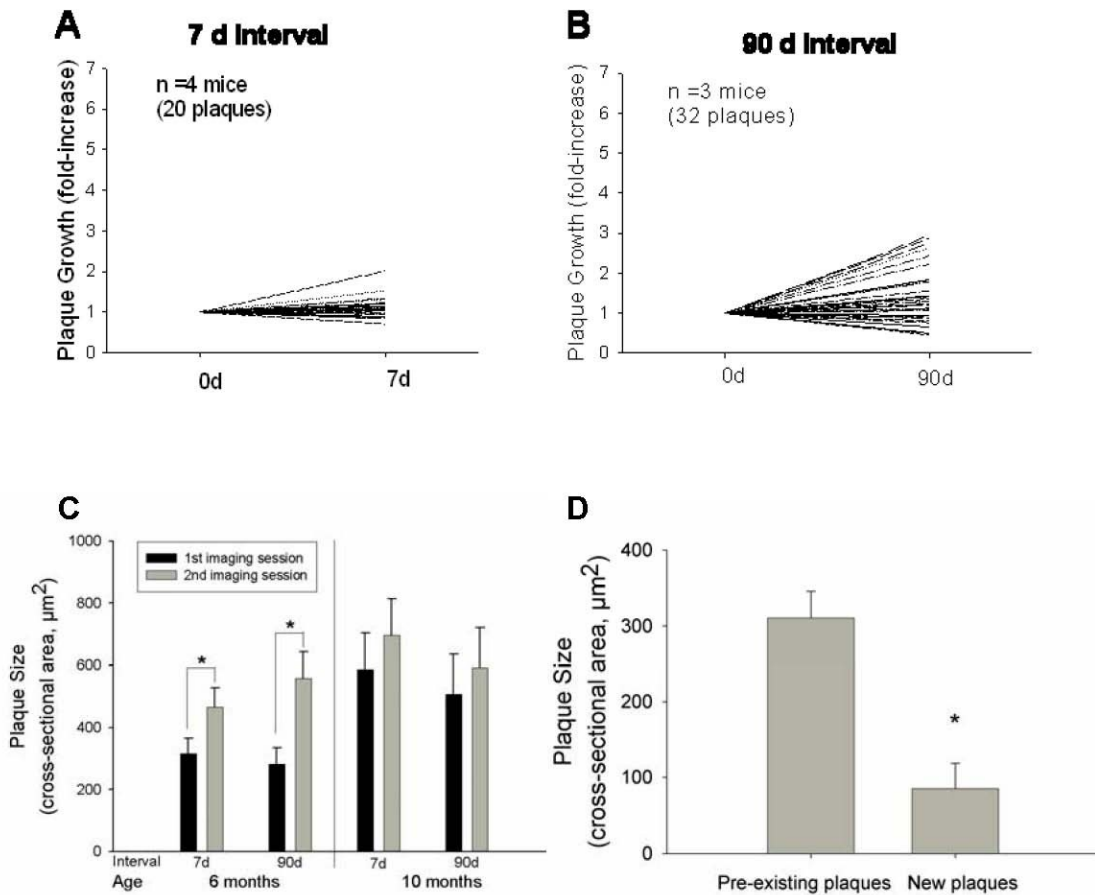
**Supplemental figure 1. Schematic representation of open- and thinned-skull cranial window preparations.** (A) In open-skull cranial window preparations, a craniotomy is performed to remove a large (6 mm diameter) section of skull. A glass coverslip is placed over the resultant window and acrylic is used to cement the coverslip in place. (B) In thinned-skull cranial window preparations, a small (< 0.8 mm diameter) section of skull is thinned using a high-speed drill and microknife until transparent. (Insets) In each preparation, the pial vasculature is clearly visible through the cranial window and serves as a guide to facilitate locating the same plaque over multiple imaging sessions.



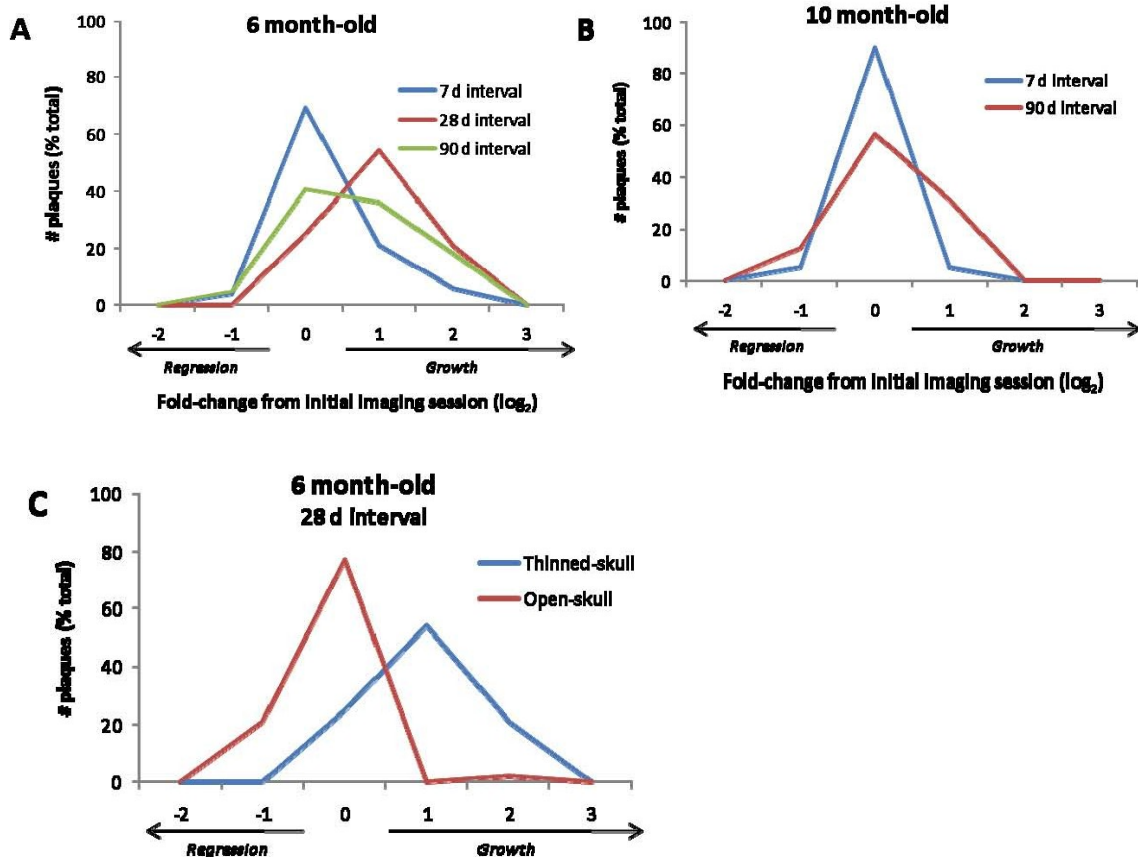
**Supplemental figure 2. Laser power does not affect plaque size determination. (A)**

Several high power fields containing multiple plaques were repeatedly imaged using increasing laser power (14-20%) while detection gain and amplification parameters were

held constant. No significant differences in plaque size determination were present across laser intensities. (B) Representative micrographs illustrate no difference in average plaque size as a function of laser power. (C, D). A pre-set threshold (threshold = mean + 4\*(standard deviation); Sigmascan Pro Image Analysis software) was used to capture methoxy-X04-labeled plaques while excluding background staining in all cross-sectional area calculations.



**Supplemental figure 3. Ten month-old APP/PS1 mice do not exhibit significant average plaque growth.** (A) Average plaque growth was not significant at 7-day or (B) 90-day intervals in 10 month-old APP/PS1 mice. (C) Average absolute plaque size sampled in 6 month-old mice appeared smaller than that in 10 month-old mice and plaques imaged in 6 month-old mice showed greater mean growth than those imaged in 10 month-old mice. (D) Newly formed plaques are significantly smaller than pre-existing plaques in 6 month-old animals imaged at a 28-day interval ( $n=4$  mice/group; Student's t-test,  $*=p\leq 0.05$ ).



**Supplemental figure 4. Frequency distribution plots indicate that plaque growth**

**dynamics are related to animal age and skull window preparation.** (A) Plaques

imaged under thinned-skull window preparations in 6 month-old APP/PS1 mice exhibited modest growth over 7-day intervals and more robust growth over 28- and 90-day

intervals. (B) Plaque growth was less pronounced under thinned-skull preparations in 10

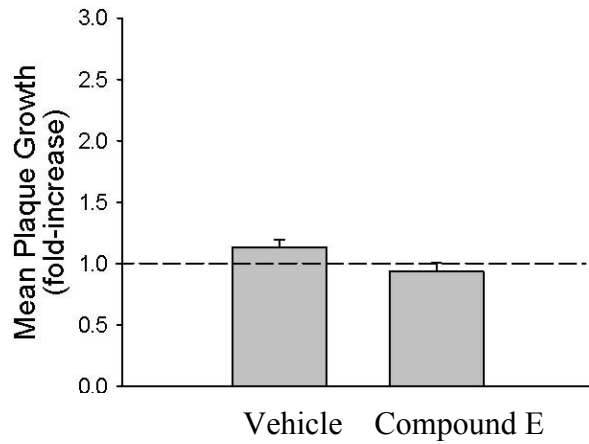
month-old mice. (C) Comparative analysis of plaque growth over a 28-day interval under

thinned- vs. open-skull window preparations in 6 month-old mice suggested that plaques

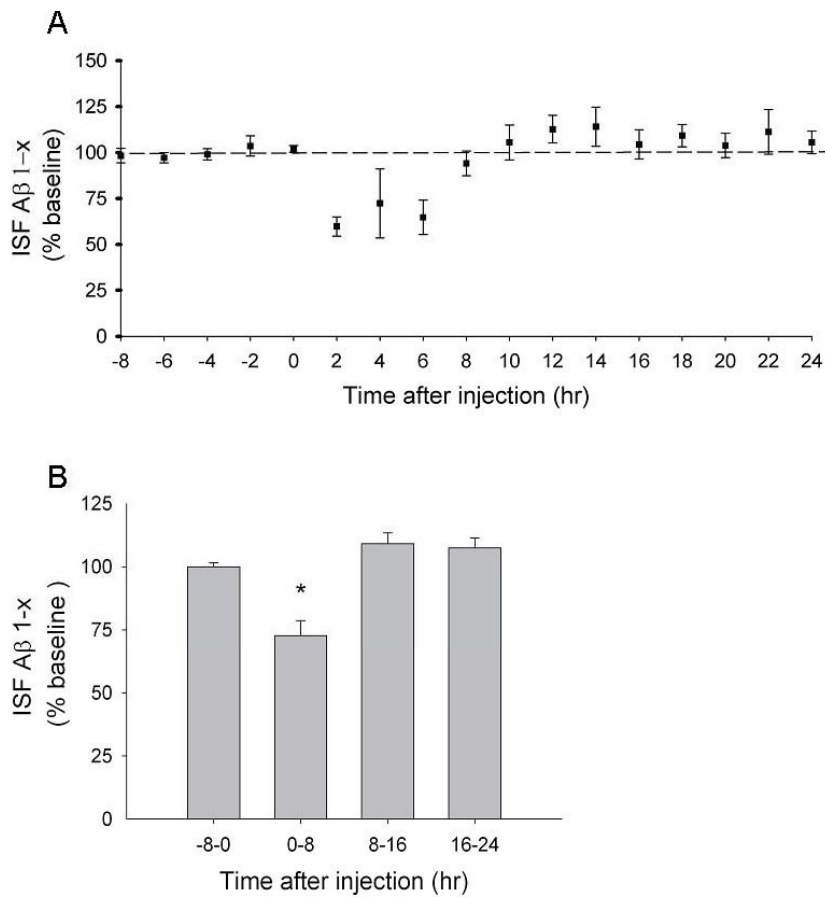
imaged under thinned-skull windows exhibited robust growth with little evidence of

regression. In contrast, plaques imaged under open-skull windows did not exhibit

significant growth but showed a greater frequency of regression.



**Supplemental figure 5.  $\gamma$ -secretase inhibition does not alter plaque growth in 10 month-old APP/PS1 mice.** Ten month-old APP/PS1 mice were treated daily with vehicle or Compound E (3 mg/kg, i.p.) for 7 days ( $n=4$  mice/group). Plaque growth is expressed as a percentage of cross-sectional area at the initial imaging session. No significant difference in average plaque size was present between groups.



**Supplemental figure 6. Compound E transiently reduces ISF Aβ concentration.**

Three month-old APP/PS1 mice were treated with a single dose of Compound E (3 mg/kg, i.p.) while cortical *in vivo* microdialysis was performed to continuously measure ISF Aβ levels in living mice. (A, B) Compound E treatment decreased ISF Aβ<sub>1-x</sub> by 27% during the first 8 hours after treatment and had no effect during the remaining 16 hours of sample collection (n=6).

## **Chapter 3.**

**Neuronal activity regulates the regional vulnerability to amyloid- $\beta$  deposition**

## **PREFACE**

The work in this chapter was published in the June 2011 issue of *Nature Neuroscience*.

The majority of the work was performed by Adam W. Bero with technical assistance from Ping Yan (laboratory of Jin-Moo Lee), Jee Hoon Roh, Floy Stewart and John R. Cirrito (laboratory of John R. Cirrito).

## ABSTRACT

Amyloid- $\beta$  ( $A\beta$ ) plaque deposition in specific brain regions is a pathological hallmark of Alzheimer's disease. However, the mechanism underlying the regional vulnerability to  $A\beta$  deposition in Alzheimer's disease is unknown. Herein, we provide evidence that endogenous neuronal activity regulates the regional concentration of interstitial fluid (ISF)  $A\beta$ , which drives local  $A\beta$  aggregation. Using *in vivo* microdialysis, we show that ISF  $A\beta$  concentrations in several brain regions of APP transgenic mice before plaque deposition were commensurate with the degree of subsequent plaque deposition and with the concentration of lactate, a marker of neuronal activity. Furthermore, unilateral vibrissal stimulation increased ISF  $A\beta$ , and unilateral vibrissal deprivation decreased ISF  $A\beta$  and lactate, in contralateral barrel cortex. Long-term unilateral vibrissal deprivation decreased amyloid plaque formation and growth. Our results suggest a mechanism to account for the vulnerability of specific brain regions to  $A\beta$  deposition in Alzheimer's disease.

## INTRODUCTION

Alzheimer's disease is the most common type of dementia and is characterized by insidious degeneration of brain systems that subserve memory and cognition.

Accumulation and aggregation of the A $\beta$  peptide in the extracellular space of the brain is a pathological hallmark of Alzheimer's disease. A $\beta$  is produced in neurons by sequential proteolytic cleavage of the amyloid precursor protein (APP) by  $\beta$ - and  $\gamma$ -secretase (Selkoe, 2001). Under normal conditions, A $\beta$  is secreted into the interstitial fluid (ISF) of the brain, where it is present in a soluble form throughout life (Cirrito et al., 2003). In Alzheimer's disease pathogenesis, A $\beta$  aggregates into higher-order species such as soluble oligomers and insoluble amyloid plaques in a concentration-dependent manner. As amyloid plaques are extracellular structures, the concentration of A $\beta$  in the ISF is likely to be a key determinant of whether and when A $\beta$  will aggregate (Meyer-Luehmann et al., 2003). Consistent with this hypothesis, we have recently shown that ISF A $\beta$  concentration is closely associated with amyloid plaque growth and formation *in vivo* (Yan et al., 2009).

In Alzheimer's disease-affected brain, amyloid plaque deposition is most prominent in the 'default-mode network'—a network of brain regions that shows elevated metabolic activity and aerobic glycolysis during undirected mentation (Raichle et al., 2001; Buckner et al., 2005; Buckner et al., 2008; Buckner et al., 2009; Vaishnavi et al., 2010; Vlassenko et al., 2010). Indeed, default network dysfunction is present in Alzheimer's disease patients (Greicius et al., 2004) as well as cognitively normal adults who harbor appreciable amyloid burden (Hedden et al., 2009; Sperling et al., 2009). However, the mechanism underlying the vulnerability of specific brain regions to amyloid deposition in

Alzheimer's disease is not known. Given the near direct proportionality between neuronal energy consumption and neurotransmitter cycling *in vivo* (Hyder et al., 2006), this correspondence raises the possibility of a relationship between patterns of neuronal activity throughout life and the topography of amyloid deposition in Alzheimer's disease. Evidence from our laboratory and others suggests that synaptic activity regulates A $\beta$  production and secretion into the ISF *in vitro* (Kamenetz et al., 2003; Wei et al., 2010) and *in vivo* (Cirrito et al., 2005; Cirrito et al., 2008). For example, electrical stimulation of the perforant pathway increases ISF A $\beta$  in hippocampus, whereas blockade of synaptic vesicle exocytosis decreases ISF A $\beta$ . However, the relationship between endogenous regional differences in neuronal activity and amyloid deposition remains unknown. Herein, we provide data suggesting that regional differences in endogenous neuronal activity dynamically regulate A $\beta$  levels and have implications for the development of A $\beta$ -related pathology.

## **MATERIALS AND METHODS**

### **Mice.**

Male and female Tg2576<sup>+/-</sup> (Hsiao et al., 1996) × B6SJL mice (Taconic Farms) were used at 17.5 ± 0.5 months of age for A $\beta$  immunohistochemistry and X-34 staining experiments and 3.5 ± 0.5 months of age for all other experiments. Male and female wild-type (B6SJL) mice were used at 5.5 ± 0.5 months of age. Male and female *APP<sup>swe</sup>; PSEN1 $\Delta$ E9* (Jankowsky et al., 2004) × B6C3 (APP/PS1; The Jackson Laboratory) were used at 7–7.5 months of age. When two or more groups of mice were compared, groups were sex-matched. Mice were given *ad libitum* access to food and water. All experimental protocols were approved by the Animal Studies Committee at Washington University.

### **Plaque deposition analyses.**

Brain tissue was dissected and flash-frozen for 1 min in isopentane chilled with dry ice before sectioning on a cryostat (Leica). Serial coronal sections (30- $\mu$ m section thickness) were collected from the genu of the corpus callosum to caudal hippocampus. Sections (each separated by 180  $\mu$ m) were stained with biotinylated 3D6 antibody (anti-A $\beta$ <sub>1-5</sub>; generous gift from Eli Lilly) to visualize A $\beta$  immunopositive plaques or X-34 dye to visualize fibrillar amyloid plaques. Immunostained sections were scanned using a NanoZoomer slide scanner (Hamamatsu Photonics). X-34-stained sections were imaged using a fluorescence microscope (Nikon) and images were captured using a digital CCD color camera (QCapture Pro version 6.0, QImaging). Quantitative analysis of percentage area covered by immuno- or X-34-positive staining was performed as described

previously (Kim et al., 2009b). Briefly, images of immunostained sections were exported with NDP viewer software (Hamamatsu Photonics), converted to 8-bit grayscale using ACDSee Pro 2 software (ACD Systems), thresholded to highlight A $\beta$ -specific staining and analyzed using ImageJ software (National Institutes of Health). Images of X-34-stained sections were converted to 16-bit grayscale, thresholded to highlight X-34-specific staining and analyzed using ImageJ software. A mouse brain atlas (Franklin and Paxinos, 1996) was used to identify piriform cortex, cingulate cortex, barrel cortex, hippocampus and striatum for quantitative analysis of immuno- and X-34-positive staining.

### ***In vivo* microdialysis.**

*In vivo* microdialysis used to measure A $\beta$  in the brain ISF of awake, freely behaving mice was performed essentially as described (Cirrito et al., 2003). Briefly, guide cannulae (BR-style, Bioanalytical Systems) were stereotaxically implanted into piriform cortex (bregma + 1.0 mm, 3.8 mm lateral to midline, 1.2 mm below the dura at a 21° angle), barrel cortex (at bregma, 2.0 mm lateral to midline, 1.0 mm below the dura at a 32° angle), hippocampus (bregma – 3.1 mm, 2.5 mm lateral to midline, 1.2 mm below the dura at a 12° angle) or striatum (bregma + 0.5 mm, 1.8 mm lateral to midline, 1.4 mm below the dura at a 0° angle) for measurement of steady-state A $\beta$  and lactate. For vibrissal trimming and stimulation experiments, guide cannulae were implanted into posterior barrel cortex (bregma – 1.5 mm, 1.7 mm lateral to midline, 0.7 mm below the dura at a 49° angle). Probe placement in the region of interest was verified by cresyl violet staining. Microdialysis probes (2 mm; 38 kDa molecular weight cut-off; BR-style, BioAnalytical Systems) were connected to a syringe pump (Stoelting) and artificial cerebrospinal fluid,

pH 7.35, containing (in mM) 1.3 CaCl<sub>2</sub>, 1.2 MgSO<sub>4</sub>, 3 KCl, 0.4 KH<sub>2</sub>PO<sub>4</sub>, 25 NaHCO<sub>3</sub> and 122 NaCl was continuously perfused through the microdialysis probe at a constant flow rate. For measurement of A $\beta$ <sub>x-40</sub>, A $\beta$ <sub>1-x</sub> and lactate in Tg2576 mice, a flow rate of 1.0  $\mu\text{l min}^{-1}$  was used. For measurement of A $\beta$ <sub>x-42</sub> in Tg2576 mice, a flow rate of 0.3  $\mu\text{l min}^{-1}$  was used. For measurement of A $\beta$ <sub>x-40</sub> and lactate in wild-type (B6SJL) mice, a flow rate of 0.5  $\mu\text{l min}^{-1}$  was used. For PTX and TTX infusion by means of reverse microdialysis into hippocampi of young Tg2576 mice, a stable baseline of ISF A $\beta$ <sub>x-40</sub> and lactate concentrations was obtained before drug treatment began. PTX (12.5  $\mu\text{M}$ ) was continuously infused for 12 h. After a 5 h washout period, TTX (5  $\mu\text{M}$ ) was continuously infused for 16 h before concluding the experiment. For ISF A $\beta$  half-life experiments, a stable baseline of ISF A $\beta$ <sub>x-40</sub> was obtained before intraperitoneally injecting each mouse with 10  $\text{mg kg}^{-1}$  of the  $\gamma$ -secretase inhibitor compound E (custom synthesis, AsisChem). The plot of the common logarithm of percent baseline ISF A $\beta$ <sub>x-40</sub> concentration versus time after injection was linear in each region, suggesting first-order kinetics. Therefore, the elimination half-life of ISF A $\beta$ <sub>x-40</sub> in each mouse was calculated using the slope of the linear regression from  $\log(\text{percent baseline ISF A}\beta_{x-40})$  versus time as described previously<sup>2</sup>. In vibrissal trimming experiments, stable baseline concentrations of ISF A $\beta$ <sub>x-40</sub> and ISF lactate were obtained before all mystacial vibrissae contralateral to the microdialysis probe were trimmed to within 1 mm of the facial pad using fine surgical scissors (Roboz). Vibrissae ipsilateral to the microdialysis probe remained intact throughout the experiment. In vibrissal stimulation experiments, mice were anesthetized with ketamine-xylazine (130.4 and 20.1  $\text{mg kg}^{-1}$ , respectively) during the microdialysis sampling period. All vibrissae ipsilateral to the microdialysis probe were trimmed to

within 1 mm of the facial pad using fine surgical scissors (Roboz). Mechanical vibrissal stimulation was performed by gently brushing vibrissae contralateral to the microdialysis probe using a cotton-tipped applicator for 30 min (5–7 Hz, 4 s burst, 4 s inter-burst interval). In sleep/wake experiments, guide cannulae were implanted into hippocampus 2 weeks before microdialysis began. Mice were habituated to the microdialysis sampling environment for 3 d and microdialysis samples collected during this period were discarded. On the fourth day, samples were collected and stored for analysis.

### **ELISA.**

Microdialysis samples were analyzed for  $A\beta_{x-40}$ ,  $A\beta_{x-42}$  or  $A\beta_{1-x}$  using a species-specific sandwich enzyme-linked immunosorbent assay (ELISA). Briefly,  $A\beta_{x-40}$ ,  $A\beta_{x-42}$  and  $A\beta_{1-x}$  were captured using monoclonal antibodies targeting amino acids 35–40 (HJ2, generated in-house), 37–42 (HJ7.4, generated in-house) and 13–28 (m266) of  $A\beta$ , respectively. For  $A\beta_{x-40}$  and  $A\beta_{x-42}$  assays, a biotinylated central-domain monoclonal antibody (HJ5.1, generated in-house) followed by streptavidin–poly-horseradish peroxidase-40 (Fitzgerald) was used for detection. For  $A\beta_{1-x}$  assays, a biotinylated N-terminal-domain monoclonal antibody (3D6B) followed by streptavidin–poly-horseradish peroxidase-20 was used for detection (Fitzgerald). The antibodies m266 and 3D6B were generous gifts from Eli Lilly. All assays were developed using Super Slow ELISA TMB (Sigma) and read on a Bio-Tek Synergy 2 plate reader at 650 nm.

### **Intraparenchymal EEG recording.**

Depth EEG recording was performed as previously described (Cirrito et al., 2005).

Briefly, bipolar recording electrodes (A-M Systems) were affixed to the microdialysis

guide cannula and stereotaxically implanted into the hippocampus. Electrodes extended approximately 1 mm from the tip of the guide cannula to position the electrodes near the center of the 2-mm microdialysis membrane. EEG activity was assessed using a P511K A.C. preamplifier (Grass Technologies), digitized with a DigiData 1440A data acquisition system (Molecular Devices) and recorded digitally using pClamp 10.2 (Molecular Devices).

### **Lactate assay.**

An enzymatic lactate assay kit (BioVision) was used to measure lactate present in ISF samples according to the manufacturer's instructions. Assays were read on a Bio-Tek Synergy 2 plate reader at 570 nm.

### **Western blot.**

Dissected tissue from piriform, barrel and cingulate cortices was homogenized in radioimmunoprecipitation assay (RIPA) buffer (150 mM NaCl, 50 mM Tris, 0.5% (wt/vol) deoxycholic acid, 1% (vol/vol) Triton X-100, 0.1% (wt/vol) SDS, 2.5 mM EDTA and a protease inhibitor cocktail (Calbiochem), pH 8.0; 10  $\mu\text{l mg}^{-1}$  tissue wet weight) with a manual wand. Dissected tissue from hippocampus and striatum was homogenized in RIPA buffer by sonication. Tissue homogenates were centrifuged at 13,500g at 4 °C for 15 min and supernatant was saved for analysis. In addition to normalizing western blot results to equal amounts of brain wet weight loaded per lane, a loading control was also performed for each tissue sample. Equal volumes of tissue samples were spiked with 5  $\mu\text{g}$  fluorescein-conjugated BSA (Biosearch Technologies) to serve as a loading control and equal volumes of tissue homogenate were separated by 4–

12% Bis-Tris gel electrophoresis (Invitrogen) under reducing conditions. Nitrocellulose blots (0.2  $\mu$ m pore size, Bio-Rad) were probed for full-length APP using 6E10 antibody (human-specific; Covance) or APP CTFs using CT695 antibody (reactivity with human and mouse; Invitrogen). Normalized band intensity was quantified using ImageJ (National Institutes of Health).

### **Sleep/wake monitoring.**

Polysomnographic sleep-wake cycle analysis of mice was performed as described previously (Kang et al., 2009). Briefly, EEG and electromyogram (EMG) electrodes were implanted simultaneously with the microdialysis guide cannula. For EEG recording, two stainless steel screws attached to wire electrodes were placed over the right frontal bone (bregma + 1.0 mm, 1.5 mm lateral to midline) and the right parietal bone (bregma – 3.0 mm, 2.5 mm lateral to midline). Two wire electrodes were directly inserted into the neck musculature for EMG recording. The ground electrode was placed on the skull over the cerebellum. Insulated leads from the EEG and EMG electrodes were soldered to a mini-connector. After surgery, mice were housed in 12 h light/12 h dark conditions (light phase beginning at 6 a.m.) for 2 weeks before recording began. To monitor the sleep-wake cycle, mice were transferred to recording cages maintained in 12 h light/12 h dark conditions (light phase beginning at 6 a.m.) and the mini-connector was connected to flexible recording cables. Mice were habituated to the recording cages for 3 d. At the conclusion of the habituation period, EEG and EMG recording began simultaneously with microdialysis sample collection. EEG and EMG signals were displayed on a monitor and stored in a computer for off-line analysis of sleep states. EEG and EMG recordings were assessed using a P511K A.C. preamplifier (Grass Technologies), digitized with a

DigiData 1440A data acquisition system (Molecular Devices) and recorded digitally using pClamp 10.2 (Molecular Devices). EEG and EMG signals were filtered (EEG: high pass, 1 Hz; low pass, 30 Hz; EMG: high pass, 10 Hz; low pass, 100 Hz) and used to identify vigilance states. EEG and EMG recordings were scored semiautomatically using sleep scoring software (SleepSign, Kissei Comtec) and binned into 10-s epochs as wakefulness, rapid eye movement (REM) sleep and non-REM sleep per standard criteria of rodent sleep. Semiautomatic sleep scoring was visually inspected and corrected when appropriate.

#### **Thinned-skull cranial window surgery.**

Thinned-skull cranial windows were prepared on the day of the first multiphoton imaging session as described previously (Yan et al., 2009). Briefly, mice were anesthetized under volatile isoflurane and the skin and periosteum were removed to expose the skull. A high-speed drill and microsurgical blade (Surgistar) were used to thin the skull until it was transparent and flexible. One cranial window (2 × 2 mm) was prepared over barrel cortex (bregma – 1.5 mm, 3.5 mm lateral to midline) of each hemisphere.

#### ***In vivo* multiphoton microscopy.**

Longitudinal multiphoton microscopy to monitor amyloid plaque growth was performed as described previously (Yan et al., 2009). Briefly, mice were injected intraperitoneally with the fluorescent amyloid-binding compound methoxy-X04 [(Klunk et al., 2002); 5 mg ml<sup>-1</sup>] 24 h before each multiphoton imaging session. Mice were mounted on a custom-built stereotaxic apparatus and a small ring of molten bone wax was applied to the skull surrounding the perimeter of the window to create a water immersion chamber.

The cranial window was centered under the objective lens on a two-photon microscope (LSM 510 META NLO system (Carl Zeiss) with a Cameleon Ti:sapphire laser (Coherent Inc.)). Two-photon fluorescence was generated with 750 nm excitation and fluorescence emission was detected at 435–485 nm. A 10X water-immersion objective (numerical aperture 0.33, Zeiss) was used to create a site map during initial imaging and a 40X water-immersion objective (numerical aperture 0.75, Zeiss) was used for high-resolution quantification of individual amyloid plaques. Incremental z-stack image series (step distances 10 and 5  $\mu\text{m}$  under 10X and 40X objectives, respectively) were acquired from the skull surface to approximately 200  $\mu\text{m}$  into cortex. To determine the effect of long-term vibrissal deprivation on amyloid plaque formation and growth, the same sites of each hemisphere of barrel cortex in each mouse were imaged on day 0 and day 28. Collapsed z-stack images of each amyloid plaque were measured by cross-sectional area using SigmaScan Pro Image Analysis Software (Systat Software) as previously described (Yan et al., 2009). Plaques were excluded from analysis if they were located at the edge of the window or showed fluorescence intensity less than the mean intensity of an adjacent background region or if the image acquisition was affected by motion artifacts from heartbeat or respiration.

### **Double immunofluorescence.**

To compare astrocytic and microglia activation in barrel cortex after long-term vibrissal deprivation, mice were transcardially perfused with 0.9% saline followed by 4% paraformaldehyde in 0.1 M phosphate buffer immediately after the final multiphoton imaging session. Brains were removed and postfixed in 4% paraformaldehyde for another 4 h. Coronal free-floating sections (50  $\mu\text{m}$  thick) were cut on a cryostat (Leica). Sections

were incubated overnight at 4 °C in a combination of mouse anti–glial fibrillary acidic protein monoclonal antibody (Sigma) and rabbit anti-Iba1 (Wako Chemicals). A secondary antibody mixture of Alexa Fluor 488–conjugated donkey anti–mouse IgG (Invitrogen) and Cy3-conjugated donkey anti–rabbit IgG (Jackson ImmunoResearch Laboratories) was used for detection. Sections were imaged using a confocal microscope (Zeiss LSM).

### **Statistical analysis.**

Statistical significance was determined by two-tailed *t*-test if two groups were compared. When variance differed significantly between groups, Welch's *t*-test was used. One-way ANOVA followed by Tukey's *post hoc* test for multiple comparisons tests were used when more than two groups were compared. Correlation was determined using Pearson product moment correlation test. All statistical analyses were performed using Prism version 4.0 for Windows (GraphPad). Values were accepted as significant if  $P < 0.05$ .

## RESULTS

### Regional plaque deposition in aged Tg2576 mouse brain

In Alzheimer's disease, amyloid deposition is most prominent in brain areas that comprise the default network. Core regions of the default network in human cortex include medial and lateral parietal, posterior cingulate, retrosplenial and medial prefrontal areas, as well as the hippocampal formation. To begin to elucidate the mechanisms that regulate region-specific amyloid deposition, we first characterized the distribution of A $\beta$  deposition in APP transgenic (Tg2576) mice, which express a mutated form of amyloid precursor protein (APP). Brain sections from Tg2576 mice  $17.5 \pm 0.5$  months old were immunostained with biotinylated 3D6 antibody, to A $\beta$  amino acids 1-5 (anti-A $\beta_{1-5}$ ) to determine the percentage area occupied by A $\beta$  plaques in brain regions of interest. We found progressively higher A $\beta$  plaque burden across barrel ( $3.96\% \pm 0.69$ ), cingulate ( $9.00 \pm 1.59$ ) and piriform ( $16.54 \pm 4.07$ ) cortices (Fig. 1a–c). A $\beta$  plaque burden in hippocampus ( $5.51 \pm 1.45$ ) was similar to that in barrel cortex; striatum ( $0.62 \pm 0.11$ ) had the least plaque deposition of all regions examined (Fig. 1a–c). Tg2576 mice thus show region-specific A $\beta$  deposition that is similar to the pattern observed in human Alzheimer's disease.

To determine whether fibrillar amyloid plaques showed a distribution similar to A $\beta$  immunopositive plaques, we stained brain sections from aged Tg2576 mice with the amyloid-specific dye X-34. In accord with the pattern of A $\beta$  immunopositive plaque deposition, we found that the percentage area occupied by X-34–positive amyloid plaque deposition was progressively higher in barrel ( $0.27\% \pm 0.03$ ), cingulate ( $1.22 \pm 0.34$ ) and

piriform ( $2.90 \pm 0.40$ ) cortices. Amyloid deposition in hippocampus ( $0.43 \pm 0.09$ ) was similar to that in barrel cortex. Amyloid was not detected in striatum (Fig. 1d–i). These results suggest that regional differences in A $\beta$  and amyloid plaque deposition are present in aged Tg2576 mouse brain and that Tg2576 mice represent a useful model in which to examine mechanisms underlying regional vulnerability to A $\beta$  and amyloid plaque deposition.

### **ISF A $\beta$ predicts region-specific plaque deposition**

As we have previously demonstrated that the concentration of A $\beta$  in the ISF is closely associated with amyloid plaque growth and formation *in vivo*, we hypothesized that the steady-state concentration of ISF A $\beta$  in each brain region early in life, before plaque deposition, would predict the degree of subsequent plaque deposition in aged mice. To test this hypothesis, we performed *in vivo* microdialysis to measure steady-state ISF A $\beta$  in brain regions of young (age  $3.5 \pm 0.5$  months) Tg2576 mice before the onset of plaque deposition. Using an A $\beta_{x-40}$ -specific ELISA, we found that steady-state ISF A $\beta_{x-40}$  concentrations were greatest in piriform cortex ( $2,296.55 \pm 308.35$  pg ml $^{-1}$ ), intermediate in barrel cortex ( $824.16 \pm 112.81$ ) and hippocampus ( $1,150.10 \pm 130.71$ ) and lowest in striatum ( $184.74 \pm 25.71$ ; Fig. 2a). ISF A $\beta_{x-40}$  concentrations in young mice before plaque deposition therefore predict the amount of both A $\beta$  (Fig. 2b) and fibrillar amyloid (Fig. 2c) plaque deposition in aged mice in a region-specific manner. We next sought to determine whether the concentration of the more amyloidogenic form of A $\beta$ , A $\beta_{x-42}$ , in each brain region of young mice predicts the level of plaque deposition in aged mice. Consistent with our data regarding regional ISF A $\beta_{x-40}$  concentrations, an A $\beta_{x-42}$ -specific ELISA showed that ISF A $\beta_{x-42}$  concentration was greatest in piriform cortex ( $104.94 \pm$

30.21 pg ml<sup>-1</sup>), intermediate in barrel cortex (48.24 ± 6.79) and hippocampus (44.31 ± 8.25) and lowest in striatum (9.47 ± 1.46; Fig. 2d). Therefore, regional ISF Aβ<sub>x-42</sub> concentration in young mice also predicts the degree of regional Aβ (Fig. 2e) and amyloid (Fig. 2f) plaque deposition in aged mice.

Next, we assessed whether regional differences in ISF Aβ levels were present in young wild-type (B6SJL) mice. In accord with our findings in APP transgenic mice, mouse ISF Aβ<sub>x-40</sub> concentrations were significantly greater in hippocampus (148.51 ± 17.93 pg ml<sup>-1</sup>) than in striatum (47.4 ± 11.46; *P* = 0.0032; Supplementary Fig. 1a). This result suggests that regional differences in ISF Aβ concentration are intrinsic to normal brain physiology. Together, these data suggest that steady-state ISF Aβ levels in young mice predict the degree of Aβ and amyloid plaque deposition in a region-specific manner.

### **ISF lactate predicts region-specific ISF Aβ**

As the default network shows elevated cerebral metabolism during resting conditions, one possibility is that elevated metabolic activity in specific brain regions throughout life regulates the ultimate distribution of amyloid deposition. Previous data suggest that synaptic activity regulates soluble extracellular Aβ levels *in vitro* and *in vivo*. As ISF Aβ concentration is closely associated with amyloid plaque growth and formation, we hypothesized that regional differences in baseline neuronal activity would be proportional to regional steady-state ISF Aβ concentration in Tg2576 mice before the onset of plaque deposition. Previous data suggest that neuronal activity directly regulates extracellular lactate concentration *in vitro* (Pellerin and Magistretti, 1994) and *in vivo* (Uehara et al., 2008). To further establish ISF lactate as a marker of neuronal activity, we

pharmacologically manipulated neuronal activity during *in vivo* microdialysis with concurrent intraparenchymal electroencephalogram (EEG) recording in young Tg2576 mice. To determine whether increased neuronal activity increases ISF lactate and A $\beta$ , we administered picrotoxin (12.5  $\mu$ M; PTX), a GABA<sub>A</sub> receptor antagonist, by means of reverse microdialysis. Infusion of PTX into hippocampus increased hippocampal EEG amplitude (Fig. 3a) and ISF lactate compared to basal conditions (PTX, 129.6  $\pm$  6.4% of basal; basal, 100.0  $\pm$  8.76;  $P$  = 0.0342; Fig. 3b and Supplementary Fig. 2a). In accord with previous data (Cirrito et al., 2008), PTX also significantly increased hippocampal ISF A $\beta_{x-40}$  concentration relative to basal conditions (PTX, 125.8  $\pm$  5.16% of basal; basal, 100.0  $\pm$  5.21;  $P$  = 0.0126; Fig. 3c and Supplementary Fig. 2b). To determine whether depression of local neuronal activity reduces ISF lactate and A $\beta$ , we administered the voltage-gated sodium channel blocker tetrodotoxin (5  $\mu$ M; TTX) by means of reverse microdialysis. Compared to basal conditions, TTX reduced EEG amplitude (Fig. 3a) and ISF lactate in hippocampus (TTX, 69.62  $\pm$  2.69% of basal; basal, 100.0  $\pm$  8.75;  $P$  = 0.0160; Fig. 3b and Supplementary Fig. 2a). Consistent with previous data (Cirrito et al., 2005), TTX infusion also reduced ISF A $\beta_{x-40}$  concentration (TTX, 67.11  $\pm$  2.94% of basal; basal, 100.0  $\pm$  5.21;  $P$  = 0.0015; Fig. 3c and Supplementary Fig. 2b). Across basal, PTX treatment and TTX treatment conditions, ISF lactate significantly correlated with ISF A $\beta$  (Pearson  $r$  = 0.7645,  $P$  < 0.0001; Fig. 3d). Together, these data suggest that increasing neuronal activity increases, and decreasing neuronal activity decreases, ISF lactate concentration and suggest that ISF lactate is a marker of neuronal activity *in vivo*.

To test the hypothesis that regional differences in ISF lactate are proportional to regional steady-state ISF A $\beta$  concentration before the onset of plaque deposition, we next

performed *in vivo* microdialysis to measure steady-state ISF lactate in several brain regions of young Tg2576 mice. We found that ISF lactate was greatest in piriform cortex ( $142.47 \pm 10.19\%$  of striatal value), intermediate in barrel cortex ( $124.94 \pm 11.58$ ) and hippocampus ( $119.3 \pm 10.53$ ) and lowest in striatum ( $100.0 \pm 11.93$ ). ISF lactate was thus commensurate with steady-state ISF  $A\beta_{x-40}$  (Fig. 4a) and  $A\beta_{x-42}$  (Fig. 4b) concentrations in young Tg2576 mice. Moreover, steady-state ISF lactate was proportional to subsequent  $A\beta$  (Fig. 4c) and amyloid (Fig. 4d) plaque deposition on a region-specific basis. To test whether the relationship between basal ISF lactate and ISF  $A\beta$  also held in wild-type mice, we measured ISF lactate in hippocampus and striatum of young B6SJL mice. In accord with our data in Tg2576 mice, ISF lactate concentration was closely associated with mouse ISF  $A\beta_{x-40}$  concentration in young B6SJL mice (Supplementary Fig. 1b). These results suggest that regional differences in ISF lactate in young mice before plaque deposition are closely associated with steady-state ISF  $A\beta$  concentration and subsequent plaque deposition in Tg2576 mice.

As steady-state ISF  $A\beta$  concentration is the result of a balance between the rates of  $A\beta$  production and clearance, we next sought to determine whether regional differences in ISF  $A\beta$  clearance rate might be associated with steady-state ISF  $A\beta$  levels in young Tg2576 mice and might therefore contribute to region-specific  $A\beta$  deposition. To assess this possibility, we performed *in vivo* microdialysis in several brain regions of young Tg2576 mice. During the microdialysis sampling period, mice were treated intraperitoneally with compound E (10 mg per kilogram body weight), a potent  $\gamma$ -secretase inhibitor, to rapidly halt  $A\beta$  synthesis and permit determination of ISF  $A\beta$  elimination half-life ( $t_{1/2}$ ) as previously described (Cirrito et al., 2003). ISF  $A\beta_{x-40}$   $t_{1/2}$  did

not differ significantly across barrel cortex ( $0.99 \pm 0.11$  h), hippocampus ( $0.97 \pm 0.03$ ) and striatum ( $1.21 \pm 0.08$ ;  $P = 0.1175$ ) in the brains of young Tg2576 mice (Supplementary Fig. 3a,b), suggesting that regional variation in ISF A $\beta$  clearance rate is not sufficient to account for the pattern of plaque deposition in aged Tg2576 mice.

### **APP processing does not predict regional ISF A $\beta$ levels**

Amyloidogenic processing of full-length APP by  $\beta$ - and  $\gamma$ -secretase is necessary for A $\beta$  generation.  $\beta$ -secretase cleavage of APP holoprotein produces C-terminal fragment (CTF)- $\beta$ , whereas non-amyloidogenic processing of APP by  $\alpha$ -secretase produces CTF- $\alpha$  and precludes A $\beta$  generation. Differential expression or processing of APP holoprotein across brain regions could thus contribute to regional differences in steady-state ISF A $\beta$  concentrations and plaque deposition. To test this possibility, we performed western blot analyses to measure APP holoprotein, CTF- $\beta$  and CTF- $\alpha$  across cortical regions that harbor differential ISF A $\beta$  concentrations and develop differential plaque burden. Despite marked differences in steady-state ISF A $\beta$  concentrations and plaque deposition, expression levels of full-length APP, CTF- $\beta$  and CTF- $\alpha$  were similar in piriform, cingulate and barrel cortices ( $P = 0.9437$ ,  $0.9821$  and  $0.6348$  for APP, CTF- $\beta$  and CTF- $\alpha$ , respectively; Supplementary Fig. 4a–c).

To determine the role of APP expression and processing in region-specific regulation of A $\beta$  concentration in subcortical structures, we next measured APP holoprotein, CTF- $\beta$  and CTF- $\alpha$  in whole cortex, hippocampus and striatum. Relative to hippocampus and striatum, APP holoprotein expression was significantly greater in cortex ( $P = 0.0017$ ; Supplementary Fig. 4d,f). CTF- $\beta$  expression was significantly lower in striatum than in

hippocampus ( $P = 0.0245$ ; Supplementary Fig. 4e,f), whereas CTF- $\alpha$  expression did not differ across cortex, hippocampus and striatum ( $P = 0.9761$ ; Supplementary Fig. 4e,f). Together, these results suggest that regional APP expression and processing profiles are not associated with local differences in steady-state ISF A $\beta$  or plaque deposition and are thus not sufficient to account for the pattern of amyloid deposition observed in Tg2576 mice.

### **Vibrissal activity regulates ISF A $\beta$ levels**

The present data suggest that regional differences in basal ISF lactate concentrations are closely associated with steady-state ISF A $\beta$  concentrations and predict subsequent plaque deposition. We next sought to determine whether a causal relationship between physiological neuronal activity and both steady-state ISF A $\beta$  and lactate concentrations exists *in vivo*. In rodents, each vibrissa is somatotopically mapped onto a defined cluster of neurons termed a 'barrel' in primary somatosensory cortex (Woolsey and Van der Loos, 1970). There, neurons in each barrel respond to stimulation of the vibrissa to which they are synaptically connected. Vibrissal stimulation increases (Melzer et al., 1985), whereas vibrissal removal decreases (Durham and Woolsey, 1978), neuronal activity in barrel cortex. Therefore, the vibrissae-barrel system represents a noninvasive physiological circuit in which to examine the relationship between physiological neuronal activity and ISF A $\beta$  concentrations *in vivo*.

To determine whether a manipulation that causes a physiological reduction in neuronal activity could reduce ISF A $\beta$  concentrations, we performed vibrissal deprivation during *in vivo* microdialysis in barrel cortex of young Tg2576 mice. After establishing stable

basal ISF A $\beta$  concentrations, we trimmed all vibrissae contralateral to the microdialysis probe to within 1 mm of the facial pad. Acute trimming of vibrissae reduced ISF A $\beta$  in barrel cortex by 22% compared to baseline ( $P = 0.0107$ ; Fig. 5a,c). Similarly, trimming of vibrissae reduced ISF lactate in barrel cortex by 19% relative to basal conditions ( $P = 0.0127$ ; Fig. 5b,c).

To determine whether a manipulation that causes a physiological increase in neuronal activity is sufficient to increase ISF A $\beta$  concentrations, we next performed unilateral mechanical vibrissal stimulation during *in vivo* microdialysis in barrel cortex of a separate cohort of young Tg2576 mice anesthetized with ketamine-xylazine. Ketamine-xylazine was chosen as the anesthetic agent because both basal and vibrissal stimulation-induced neurophysiological responses under ketamine-xylazine anesthesia resemble the responses elicited during wake and quiet sleep more closely than under other forms of anesthesia (Rojas et al., 2006). We found that unilateral mechanical vibrissal stimulation (5–7 Hz, 4 s burst, 4 s inter-burst interval) for 30 min increased ISF A $\beta_{x-40}$  in barrel cortex by 31% relative to control conditions ( $P = 0.0446$ ; Fig. 5d).

### **ISF lactate levels show diurnal fluctuation**

The sleep/wake cycle is associated with diurnal fluctuation of ISF A $\beta$ ; ISF A $\beta$  concentration is greater during wakefulness and lesser during sleep (Kang et al., 2009). Previous data from humans and animal models suggest that periods of wakefulness are associated with increased synaptic strength and periods of sleep are associated with decreased synaptic strength (Riedner et al., 2007; Vyazovskiy et al., 2008b; Gilestro et

al., 2009). Therefore, we reasoned that diurnal fluctuation of ISF A $\beta$  might be linked with lactate levels throughout the sleep/wake cycle.

To assess this possibility, we performed *in vivo* microdialysis in hippocampi of young Tg2576 mice housed in 12 h light/12 h dark conditions. Consistent with our previous findings, ISF A $\beta_{1-x}$  concentrations were 21% greater during the dark period than during the light period ( $P = 0.0314$ ; Fig. 6a,c). Moreover, ISF lactate concentrations were 23% greater during the dark period than during the light period ( $P = 0.0066$ ; Fig. 6b,c). ISF A $\beta_{1-x}$  concentrations were thus correlated with ISF lactate concentrations across the sleep/wake cycle (Pearson  $r = 0.6351$ ,  $P < 0.0001$ ; Fig. 6d). As mice spent significantly more time awake during the dark period than during the light period (dark,  $51.32 \pm 1.26$  min awake per hour; light,  $25.02 \pm 2.15$ ;  $P < 0.0001$ ), these findings suggest that wakefulness, ISF lactate and ISF A $\beta$  are co-regulated and are consistent with the hypothesis that diurnal fluctuation in neuronal activity contributes to the diurnal fluctuation in ISF A $\beta$  *in vivo*.

### **Vibrissal deprivation reduces plaque formation and growth**

We have previously demonstrated that the concentration of ISF A $\beta$  is closely related to amyloid plaque growth and formation *in vivo* (Yan et al., 2009). As our present data suggest that acute manipulations that alter neuronal activity modulate ISF A $\beta$  concentration, we hypothesized that manipulations that cause longer-term changes in neuronal activity might modulate amyloid plaque growth and formation *in vivo*. To test this hypothesis, we used 7-month-old *APP<sup>swe</sup>; PSEN1 $\Delta$ E9* [APP/PS1; (Jankowsky et al., 2004)] bitransgenic mice because this strain develops aggressive fibrillar amyloid

deposition beginning at 4–5 months of age. Using *in vivo* multiphoton microscopy, amyloid plaques in barrel cortex of each hemisphere were visualized with methoxy-X04 under thinned-skull cranial windows to obtain basal measures of individual amyloid plaque size. All vibrissae on the right side of the facial pad were subsequently trimmed to within 1 mm of the face every other day for 28 d. At the conclusion of the 28-d vibrissal deprivation period, amyloid plaques in barrel cortex of each hemisphere were reimaged to assess the effect of vibrissal deprivation on individual amyloid plaque growth. We found that plaque growth was decreased by 78% in the vibrissae-deprived relative to the control hemisphere ( $P = 0.0014$ ; Fig. 7a–e). Moreover, new amyloid plaque formation was decreased by 65% in the deprived relative to the control hemisphere ( $P = 0.0367$ ; Fig. 7a–d,f).

To determine whether suppression of amyloid plaque growth and formation upon long-term vibrissal deprivation might be attributable to increased glial activation in barrel cortex, brains were sectioned and stained for glial fibrillary acidic protein and Iba-1 to visualize astrocytic and microglial activation, respectively. Confocal microscopy revealed no qualitative difference in astrocytic (Supplementary Fig. 5a–c) or microglial (Supplementary Fig. 5d–f) activation in the deprived hemisphere compared to the control hemisphere. This result suggests that altered glial activation is not likely to contribute to the observed suppression of amyloid plaque growth and formation upon long-term vibrissal deprivation. Taken together, although long-term vibrissal deprivation results in several changes in the brain, the present data are consistent with the hypothesis that physiological neuronal activity regulates amyloid plaque growth dynamics *in vivo*.

## DISCUSSION

Aggregation of A $\beta$  into higher-order structures such as extracellular amyloid plaques is a necessary event in Alzheimer's disease pathogenesis. A fundamental feature of Alzheimer's disease is the preferential deposition of amyloid plaques in distinct brain regions. However, the mechanism by which specific brain regions are rendered vulnerable to amyloid deposition in Alzheimer's disease has heretofore remained unknown. As A $\beta$  aggregation is closely related to ISF A $\beta$  concentration *in vivo*, elucidating the mechanisms that regulate ISF A $\beta$  concentration has important implications for understanding the etiology of region-specific A $\beta$  deposition in Alzheimer's disease. In the present work, we used *in vivo* microdialysis to show that ISF A $\beta$  concentrations measured in several brain regions of young Tg2576 mice months before plaque deposition are directly proportional to the degree of subsequent plaque deposition. Moreover, ISF A $\beta$  concentrations in young mice are closely associated with concentrations of baseline ISF lactate, a marker of neuronal activity, on a region-specific basis. Furthermore, we show that physiological changes in neuronal activity are sufficient to dynamically modulate ISF A $\beta$  concentrations and amyloid plaque growth *in vivo*. Collectively, our results suggest that regional differences in basal neuronal activity level govern region-specific amyloid deposition through long-term regulation of steady-state ISF A $\beta$  concentration.

As sequential proteolysis of APP by  $\beta$ - and  $\gamma$ -secretase is necessary for A $\beta$  generation, several previous reports have examined the regional distribution of this triad as potential mediators of region-specific A $\beta$  deposition. However, the cerebral distribution of *APP*, *BACE1* and *PSEN1* transcripts is not associated with the topography of A $\beta$  deposition in

human Alzheimer's disease (Bahmanyar et al., 1987; Goedert, 1987; Page et al., 1996; Vassar et al., 1999) or APP transgenic mice (Irizarry et al., 1997; Bigl et al., 2000; Irizarry et al., 2001). Moreover, the regional distribution of  $\gamma$ -secretase activity in APP transgenic mouse brain does not correlate with the pattern of A $\beta$  deposition (Goldstein et al., 2007). Consistent with these previous reports, the present results suggest that although differences in APP expression and processing are present across a subset of brain areas in Tg2576 mice, the pattern of APP expression and processing is not sufficient to account for the pattern of A $\beta$  deposition. Together, these studies suggest that more factors are necessary to drive region-specific A $\beta$  deposition. In addition to region-specific differences in neuronal activity potentially contributing to region-specific differences in A $\beta$  deposition, other possible contributors to the presence of A $\beta$  in specific neural networks include the spread of A $\beta$  aggregates within and into the brain. For instance, exogenous intracerebral (Meyer-Luehmann et al., 2003; Meyer-Luehmann et al., 2006) or peripheral (Eisele et al., 2010) application of A $\beta$  aggregates can seed cerebral  $\beta$ -amyloidosis. Further, reports suggest that selective overexpression of APP in the cell bodies of neurons in the entorhinal cortex of transgenic mice can elevate soluble A $\beta$  and produce amyloid plaque deposition in the synaptic terminal zone of the dentate gyrus (Lazarov et al., 2002; Harris et al., 2010). Thus, transsynaptic propagation mechanisms as well as spread of A $\beta$  pathology through interconnected neural networks might also contribute to the pattern of amyloid deposition observed in Alzheimer's disease.

In the healthy human brain, a specific subset of brain regions—the default network—is preferentially engaged during resting the state. Notably, amyloid deposition in

Alzheimer's disease brain is most prominent in regions that comprise the default network. These findings raise the possibility that patterns of normal cerebral metabolism may influence the distribution of amyloid deposition in Alzheimer's disease. In accord with this hypothesis, recent data suggest that the spatial distribution of resting-state aerobic glycolysis (that is, glucose utilization in excess of that used for oxidative phosphorylation despite sufficient oxygen to oxidize glucose to carbon dioxide and water) in cognitively normal adults overlaps closely with the topography of amyloid deposition in Alzheimer's disease. Our present data demonstrating that pharmacological manipulation of neuronal activity directly regulates ISF lactate abundance are consistent with previous animal and human studies and suggest that neuronal activity stimulates aerobic glycolysis *in vivo*. Given that neuronal activity also increases A $\beta$  production and secretion into the ISF, regional differences in neuronal activity may underlie the spatial relationship between resting-state aerobic glycolysis and amyloid deposition in Alzheimer's disease.

We have previously demonstrated that ISF A $\beta$  concentrations fluctuate diurnally: ISF A $\beta$  concentration is significantly greater during waking conditions than during sleep (Kang et al., 2009). Given that neuronal activity directly regulates ISF A $\beta$  levels, we reasoned that diurnal fluctuation of neuronal activity may contribute to diurnal fluctuation of ISF A $\beta$ . Indeed, previous data suggest that periods of wakefulness are associated with net synaptic potentiation and periods of sleep are associated with synaptic downscaling and depression (Vyazovskiy et al., 2008b). Here we show that ISF lactate concentration fluctuates diurnally in a manner closely associated with the diurnal fluctuation of ISF A $\beta$ . These results are consistent with the notion that fluctuation of neuronal activity during the sleep/wake cycle contributes to the diurnal fluctuation of ISF A $\beta$  *in vivo*. This

observation further supports the hypothesis that physiological neuronal activity dynamically regulates ISF A $\beta$  levels *in vivo*.

More generally, our results suggest that factors that elevate endogenous neuronal activity over prolonged periods may accelerate progression of A $\beta$  deposition. In support of this hypothesis, recent functional magnetic resonance imaging data suggest that cognitively normal apolipoprotein E (*APOE*) allele  $\epsilon$ 4 carriers show elevated resting-state activity in the default network and increased hippocampal activation during a memory encoding task compared to noncarriers (Filippini et al., 2009). Thus, in addition to apoE isoform-dependent differences in apoE-A $\beta$  interactions (Kim et al., 2009a), elevated lifetime neuronal activity may be a complementary mechanism by which  $\epsilon$ 4 expression increases Alzheimer's disease risk. Conversely, factors that reduce activity in vulnerable neural networks may slow the progression of  $\beta$ -amyloidosis and reduce Alzheimer's disease risk. For example, epidemiological evidence suggests that educational attainment is negatively correlated with Alzheimer's disease risk (Flicker, 2010). As default network activity is suppressed during cognitively demanding tasks, one possibility is that education reduces Alzheimer's disease risk by reducing neuronal activity and A $\beta$  generation within the default network.

It is noteworthy that the regional distribution of lesions in mouse models of glutamate-induced excitotoxicity is similar to the distribution of A $\beta$  deposition described herein (Olney et al., 1997). As neuronal activity regulates both A $\beta$  and glutamate release at the synapse, the regional differences in basal neuronal activity described here may also underlie the distribution of glutamate-induced excitotoxic lesions. A more detailed understanding of the regional distribution of pre- and postsynaptic elements may provide

insight regarding the structural basis of neuronal activity patterns in normal brain and how patterns of neuronal and synaptic activity might contribute to a variety of neurological lesions.

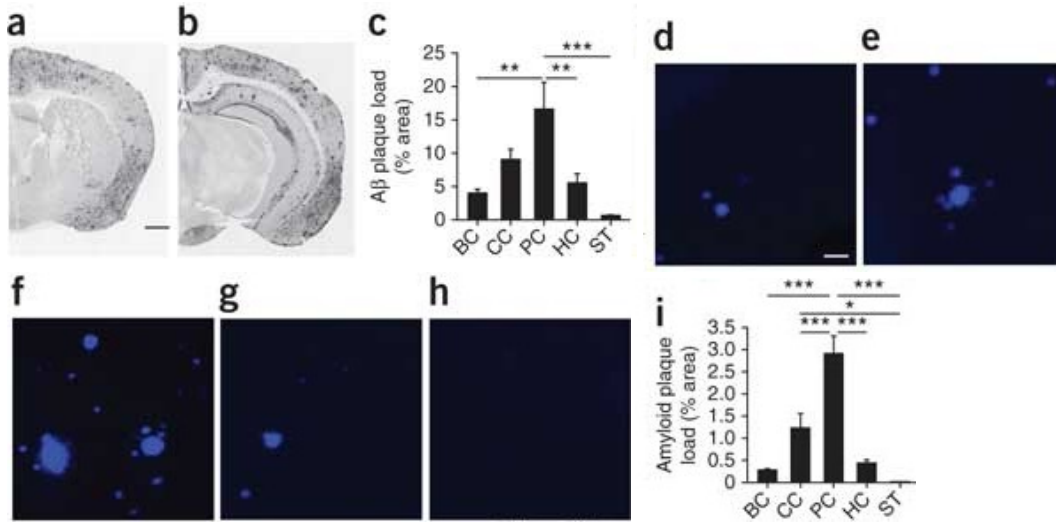


**Figure 1. Distribution of Aβ and amyloid plaque deposition in Tg2576 mouse brain.**

(a,b) Representative brain sections from aged ( $17.5 \pm 0.5$  months old) Tg2576 mice stained with biotinylated 3D6 antibody (anti-A $\beta_{1-5}$ ) to visualize A $\beta$  immunopositive plaques ( $n = 7$  per group). Scale bar, 750  $\mu$ m. (c) Percentage brain area occupied by A $\beta$  deposition in barrel (BC), cingulate (CC) and piriform (PC) cortices and hippocampus (HC) and striatum (ST). (d–h) Representative images of barrel cortex (d), cingulate cortex (e), piriform cortex (f), hippocampus (g) and striatum (h) of aged Tg2576 mice stained with the amyloid-binding dye X-34 ( $n = 6$  per group). Scale bar, 50  $\mu$ m. (i) Percentage area occupied by X-34-positive amyloid deposition in brain regions examined. \* $P < 0.05$ ; \*\* $P < 0.01$ ; \*\*\* $P < 0.001$  (one-way analysis of variance (ANOVA), Tukey's *post hoc* test for multiple comparisons). Values represent mean  $\pm$  s.e.m.

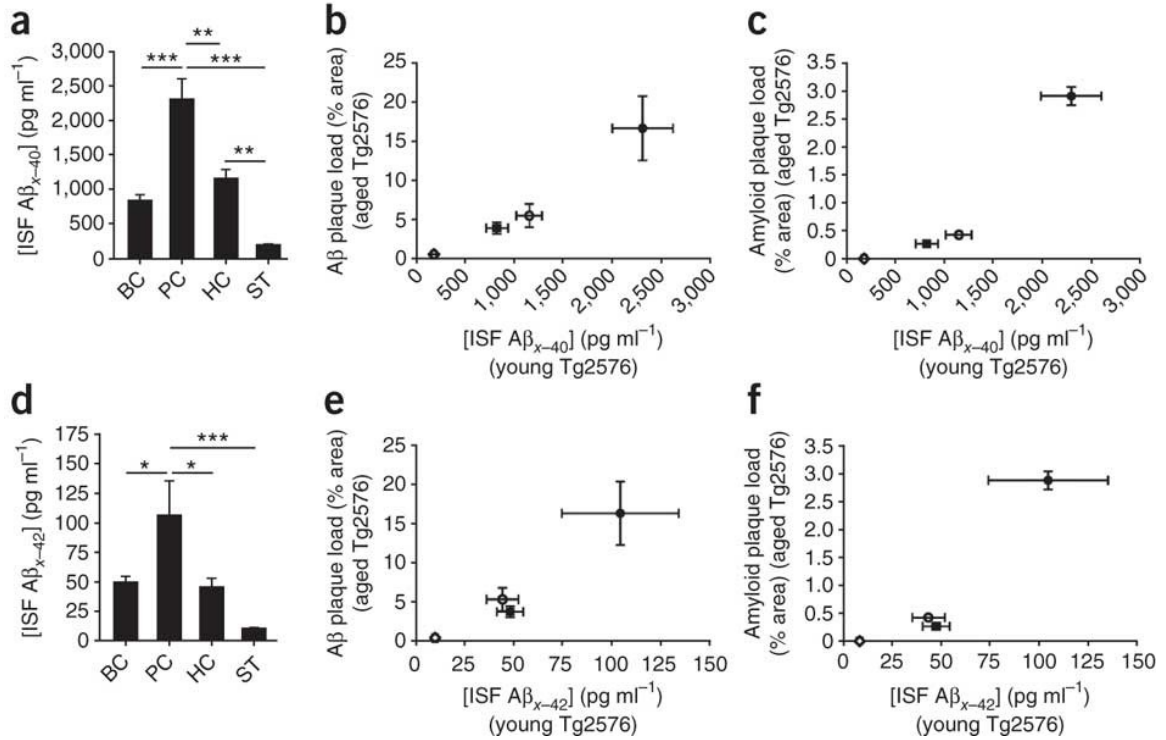


**Figure 2. Steady-state ISF Aβ concentrations in young Tg2576 mice before plaque deposition are associated with the level of region-specific plaque deposition in aged Tg2576 mice.** (a) *In vivo* microdialysis measurements of the steady-state concentrations of ISF Aβ<sub>x-40</sub> in barrel cortex (BC), piriform cortex (PC), hippocampus (HC) and striatum (ST) of 3.5 ± 0.5-month-old Tg2576 mice before the onset of plaque deposition (*n* = 5–6 per group; one-way ANOVA, Tukey's *post hoc* test for multiple comparisons). (b,c) Steady-state concentrations of ISF Aβ<sub>x-40</sub> measured in each brain region of young Tg2576 mice, plotted against subsequent Aβ (b) and amyloid (c) plaque deposition in each brain region of aged Tg2576 mice. (d) *In vivo* microdialysis measurements of the steady-state concentration of ISF Aβ<sub>x-42</sub> in barrel cortex (▪), piriform cortex (●), hippocampus (○) and striatum (◇) of 3.5 ± 0.5-month-old Tg2576 mice before the onset

of plaque deposition ( $n = 5-8$  per group; one-way ANOVA, Tukey's *post hoc* test for multiple comparisons). (e,f) Steady-state concentrations of ISF  $A\beta_{x-42}$  measured in each brain region of young Tg2576 mice, plotted against subsequent  $A\beta$  (e) and amyloid (f) plaque deposition in each brain region of aged Tg2576 mice.  $*P < 0.05$ ;  $**P < 0.01$ ;  $***P < 0.001$ . Values represent mean  $\pm$  s.e.m.

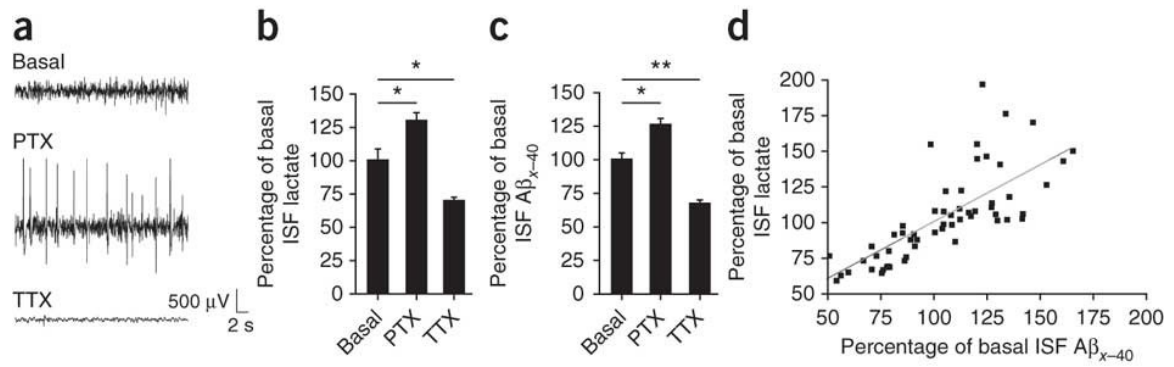


**Figure 3. Neuronal activity regulates ISF lactate concentration *in vivo*.** (a)

Representative intraparenchymal EEG recordings from hippocampus of young Tg2576 mice during basal conditions, picrotoxin (PTX; 12.5 μM) treatment or tetrodotoxin (TTX; 5 μM) treatment by means of *in vivo* microdialysis ( $n = 4$  per group). (b) Effect of local PTX or TTX infusion on ISF lactate in hippocampus of young Tg2576 mice ( $n = 4$  per group; two-tailed *t*-test). (c) Effect of local PTX or TTX infusion on ISF Aβ<sub>x-40</sub> in hippocampus of young Tg2576 mice ( $n = 4$  per group; two-tailed *t*-test). Values in b,c represent analyte concentrations during the final 6 h of drug treatment. (d) ISF lactate concentrations were correlated with ISF Aβ<sub>x-40</sub> concentrations across treatment periods (Pearson  $r = 0.7645$ ;  $P < 0.0001$ ). \* $P < 0.05$ ; \*\* $P < 0.01$ . Values represent mean ± s.e.m.

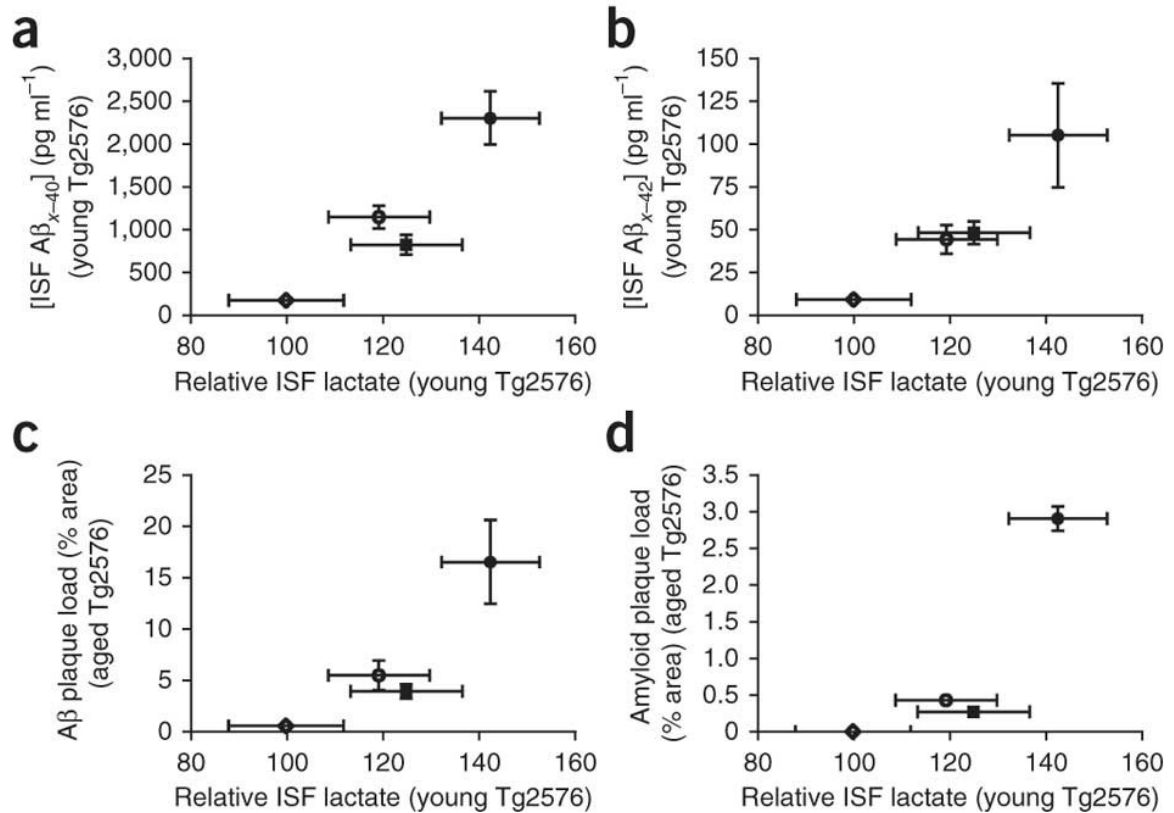


**Figure 4. Steady-state ISF lactate levels in young Tg2576 mice are closely associated with regional ISF Aβ levels in young Tg2576 mice and plaque deposition in aged Tg2576 mice. (a–d) *In vivo* microdialysis measurements of steady-state ISF lactate concentrations (expressed as a percentage of the striatal value) in barrel cortex (▪), piriform cortex (●), hippocampus (○) and striatum (◊) of young Tg2576 mice ( $n = 6–7$  per group). ISF lactate concentration in each brain region is plotted against concentration of ISF Aβ<sub>x-40</sub> (a) and ISF Aβ<sub>x-42</sub> (b) in each brain region of young Tg2576 mice. ISF lactate concentration in each brain region of young Tg2576 mice is also plotted against Aβ (c) and amyloid (d) plaque deposition in each brain region of aged Tg2576 mice. Values represent mean  $\pm$  s.e.m.**

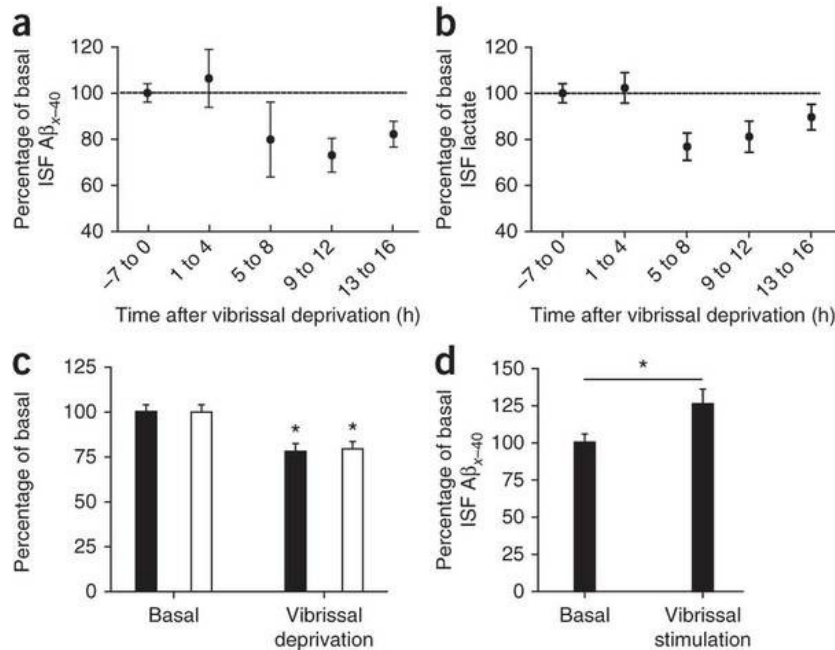


**Figure 5. Vibrissal activity regulates ISF Aβ levels *in vivo*.** (a–c) Effect of vibrissal deprivation on ISF Aβ<sub>x-40</sub> (a, black bars in c) and lactate (b, white bars in c) concentrations relative to baseline ( $n = 6-7$ ; two-tailed  $t$ -test). *In vivo* microdialysis was performed in posterior barrel cortex of young Tg2576 mice. After establishing stable basal ISF Aβ<sub>x-40</sub> and lactate concentrations, all vibrissae contralateral to the microdialysis probe were trimmed to within 1 mm of the facial pad and microdialysis sample collection continued for 16 h. (d) Effect of vibrissal stimulation on ISF Aβ<sub>x-40</sub> concentrations compared to control conditions ( $n = 4$ ; two-tailed  $t$ -test). *In vivo* microdialysis was performed in barrel cortex in a separate cohort of young Tg2576 mice that underwent subsequent unilateral vibrissal stimulation. Baseline Aβ<sub>x-40</sub> values were obtained for a 30-min period. Unilateral mechanical stimulation of vibrissae contralateral to the

microdialysis probe was performed for 30 min. \* $P < 0.05$ . Values represent mean  $\pm$  s.e.m.

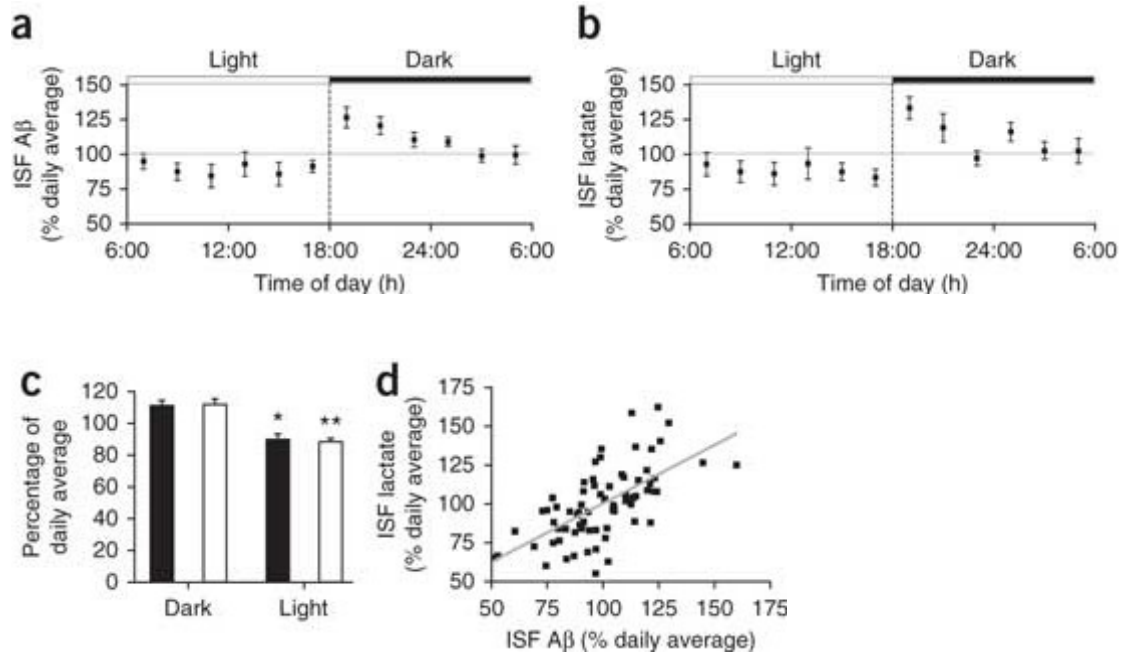


**Figure 6. Diurnal fluctuation of ISF A $\beta$  is closely associated with ISF lactate levels.**

(a–c) *In vivo* microdialysis measurements from hippocampi of young Tg2576 mice housed in 12 h light/12 h dark conditions. ISF A $\beta_{1-x}$  (a; black bars in c) and lactate (b; white bars in c) concentrations were sampled throughout the light/dark cycle ( $n = 6$ ; two-tailed t-test). (d) ISF A $\beta_{1-x}$  concentrations plotted against ISF lactate concentrations throughout the sleep/wake cycle (Pearson  $r = 0.6351$ ;  $P < 0.0001$ ). \* $P < 0.05$ ; \*\* $P < 0.01$ . Values represent mean  $\pm$  s.e.m.

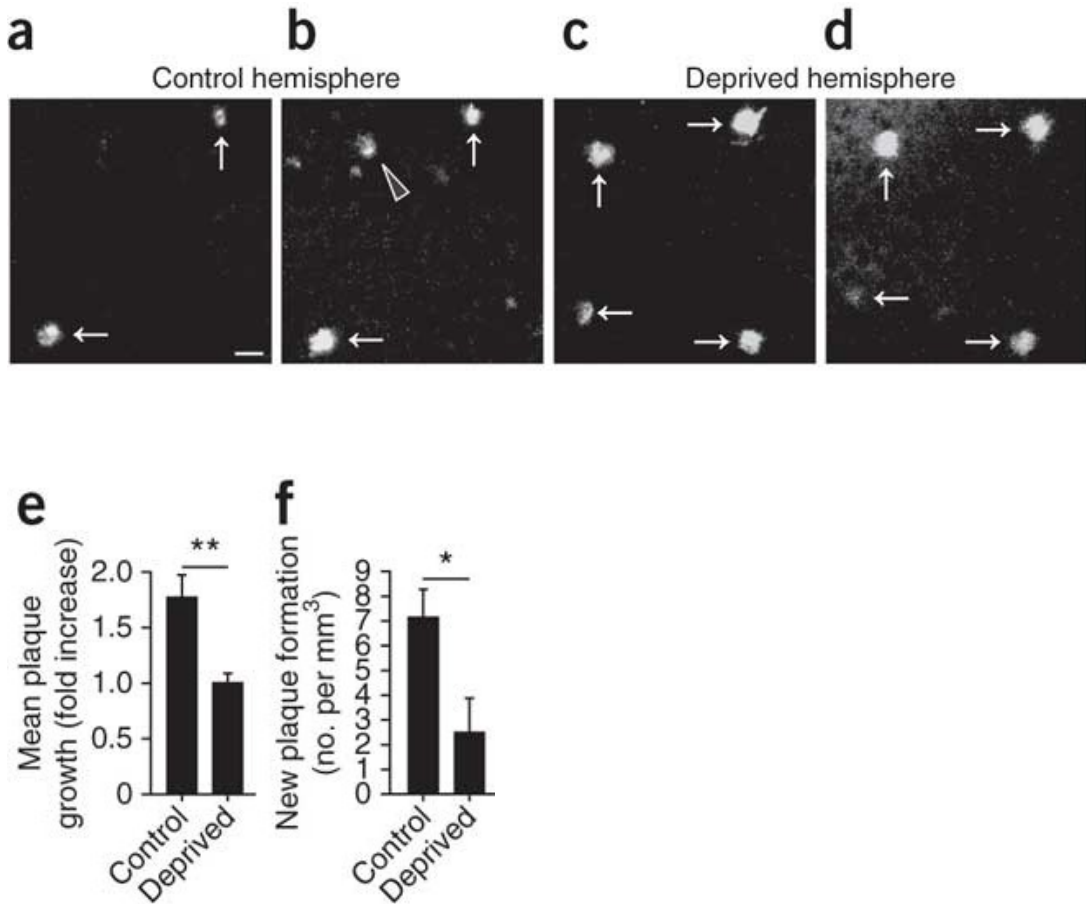
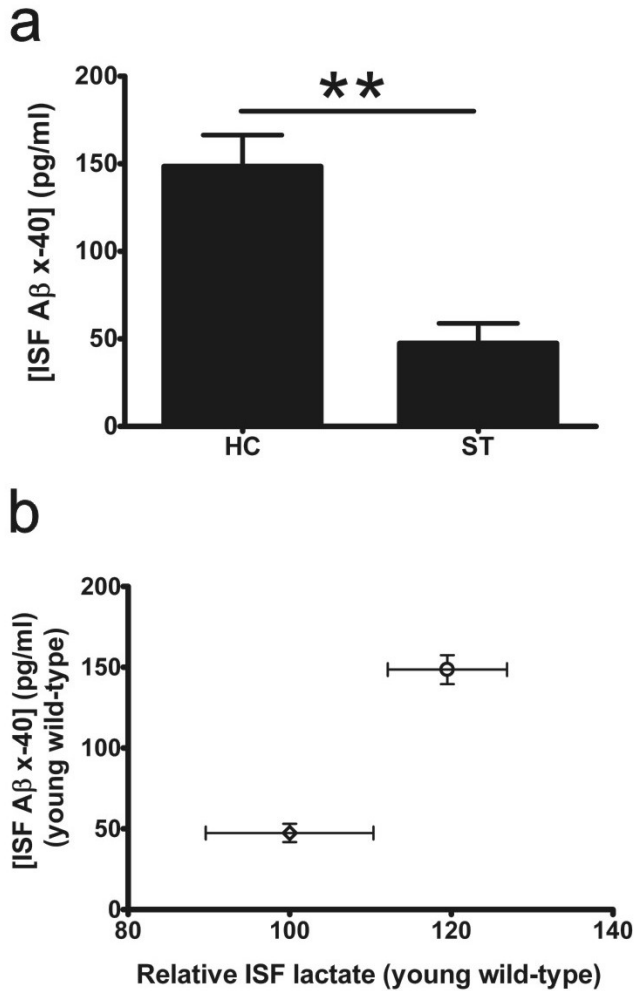
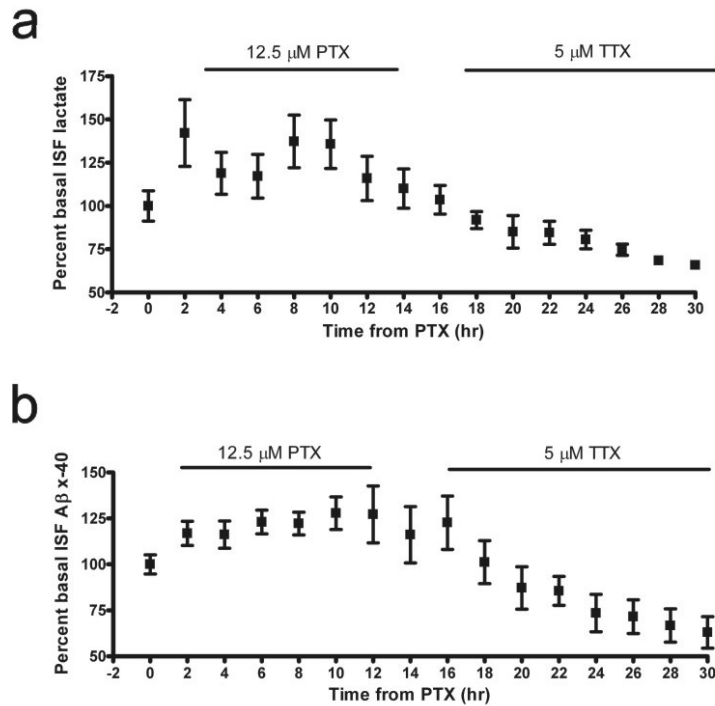


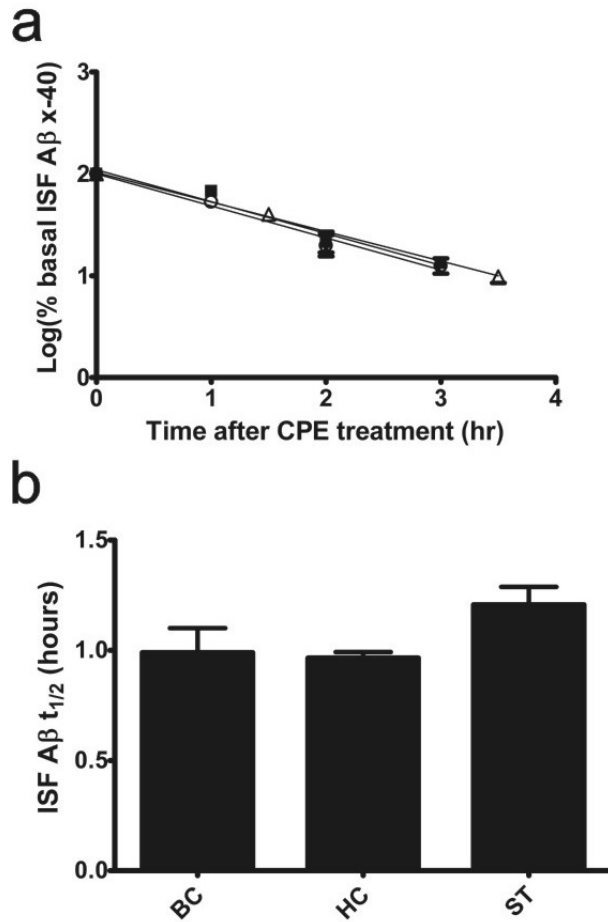
**Figure 7. Vibrissal deprivation reduces amyloid plaque growth and formation *in vivo*.** (a,b) Representative multiphoton micrographs of individual amyloid plaques in barrel cortex in control hemisphere of APP/PS1 mice before (a) and after (b) 28 d of unilateral vibrissal deprivation. (c,d) Representative multiphoton micrographs of amyloid plaques in barrel cortex in vibrissae-deprived hemisphere of APP/PS1 mice before (c) and after (d) 28 d of vibrissal deprivation. (e,f) Quantification of mean plaque growth (e) and new plaque formation (f) in vibrissae-deprived and control hemispheres ( $n = 6$  mice; two-tailed  $t$ -test). Arrows, existing amyloid plaques; arrowhead, newly formed amyloid plaque. Scale bar, 50  $\mu\text{m}$ ;  $*P < 0.05$ ;  $**P < 0.01$ . Values represent mean  $\pm$  s.e.m.



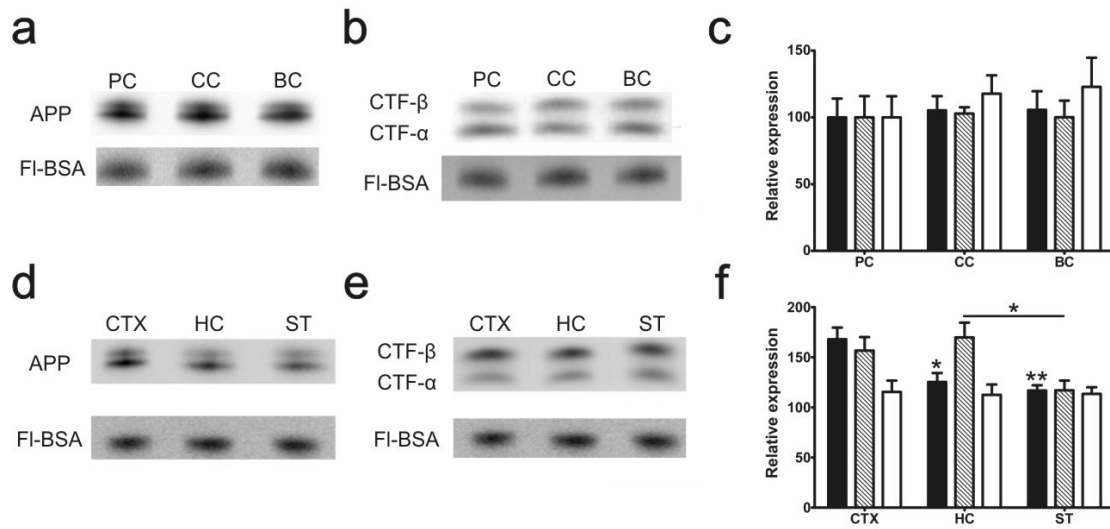
**Supplementary Figure 1. Regional ISF A $\beta$  and lactate levels in wild-type (B6SJL) mice.** (a) *In vivo* microdialysis was performed in hippocampus and striatum of  $5.5 \pm 0.5$  month-old wild-type (B6SJL) mice. Murine ISF A $\beta_{x-40}$  levels were significantly greater in hippocampus compared to striatum ( $n = 4$  per group; two-tailed t-test). (b) Murine ISF A $\beta_{x-40}$  levels were closely associated with ISF lactate levels in a region-specific manner ( $n = 4$ ). ◇, striatum; ○, hippocampus. \*\*,  $P < 0.01$ . Values represent mean  $\pm$  SEM.



**Supplementary Figure 2. Time course of picrotoxin and tetrodotoxin treatment on ISF Aβ<sub>x-40</sub> and lactate levels in hippocampus. (a,b)** Young ( $3.5 \pm 0.5$  month-old) Tg2576 mice were treated sequentially with picrotoxin ( $12.5 \mu\text{M}$ ; PTX) and tetrodotoxin ( $5 \mu\text{M}$ ; TTX) via reverse microdialysis during the microdialysis sampling period. **(a)** ISF lactate and **(b)** Aβ<sub>x-40</sub> levels were increased during PTX treatment and decreased during TTX treatment ( $n = 4$  per group). Values represent mean  $\pm$  SEM.

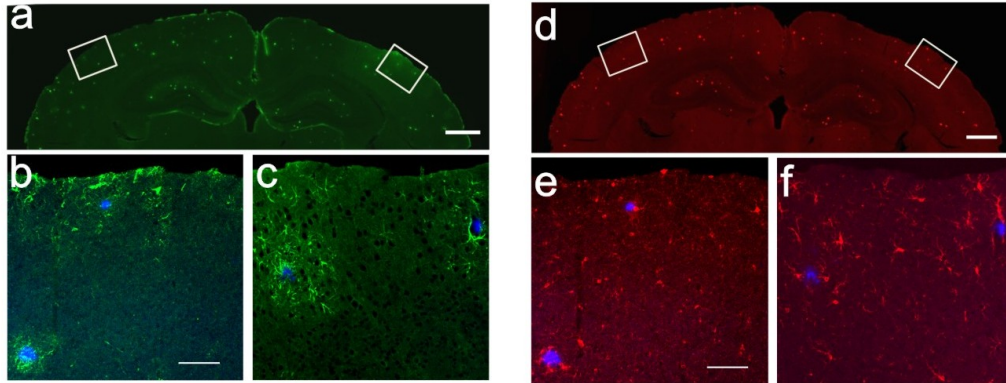


**Supplementary Figure 3. ISF A $\beta_{x-40}$  clearance rates across brain regions of young Tg2576 mouse brain.** (a,b) After baseline ISF A $\beta_{x-40}$  levels were established, young ( $3.5 \pm 0.5$  month-old) Tg2576 mice were treated with a potent  $\gamma$ -secretase inhibitor, Compound E (CPE;  $10 \text{ mg kg}^{-1}$ ), during the microdialysis sampling period to halt A $\beta$  synthesis and permit ISF A $\beta_{x-40}$   $t_{1/2}$  determination. ISF A $\beta_{x-40}$   $t_{1/2}$  did not differ across barrel cortex (BC), hippocampus (HC) and striatum (ST;  $n = 4$  per group; one-way ANOVA, Tukey's post hoc test for multiple comparisons). ○, barrel cortex; ■, hippocampus; Δ, striatum. Values represent mean  $\pm$  SEM.



**Supplementary Figure 4. APP expression and processing are not associated with regional ISF A $\beta$  levels or plaque deposition.** (a–c) Piriform (PC), cingulate (CC) and barrel (BC) cortices were dissected from fresh brain sections (500  $\mu$ m thick) of young (3.5  $\pm$  0.5 month-old) Tg2576 mice. Dissected tissue samples were analyzed for expression of (a) full-length APP, (b) CTF- $\beta$  and CTF- $\alpha$  by western blot analysis. APP and CTF expression in each lane was normalized to fluorescein-conjugated bovine serum albumin (FI-BSA) loading control. (c) Expression of APP, CTF- $\beta$  and CTF- $\alpha$  did not differ across piriform, cingulate and barrel cortices ( $n = 6$  per group; one-way ANOVA, Tukey’s post hoc test for multiple comparisons). (d–f) Whole cortex (CTX), hippocampus (HC) and striatum (ST) were dissected from fresh brain tissue of young (3.5  $\pm$  0.5 month-old) Tg2576 mice. Dissected tissue samples were analyzed for expression of (d) full-length APP, (e) CTF- $\beta$  and CTF- $\alpha$  by western blot analysis. APP and CTF expression in each lane was normalized to FI-BSA loading control. (f) Expression of full-length APP was significantly greater in cortex compared to hippocampus and striatum.

CTF- $\beta$  expression was greater in hippocampus compared to striatum. CTF- $\alpha$  expression did not differ significantly across brain regions ( $n = 7$  per group; one-way ANOVA, Tukey's post hoc test for multiple comparisons). ■, full-length APP; ■, CTF- $\beta$ ; □, CTF- $\alpha$ . \*,  $P < 0.05$ ; \*\*,  $P < 0.01$ . Panels **a,b,d,e** contain cropped blots. Values represent mean  $\pm$  SEM.



**Supplementary Figure 5. Glial activation in barrel cortex following long-term vibrissae deprivation.** (a) Low-power image of a representative brain section from an APP/PS1 (7–7.5 months old) mouse that underwent 28-day unilateral vibrissae deprivation stained with an anti-GFAP antibody to visualize astrocytes (green) and counter-stained with X-34 to visualize amyloid plaque deposition (blue). No clear difference in GFAP staining was evident between vibrissae-deprived (left; **b**) and control (right; **c**) hemispheres ( $n = 6$ ). (d) Low-power image of a representative brain section from an APP/PS1 (7–7.5 months old) mouse that underwent 28 day unilateral vibrissae deprivation stained with an anti-Iba-1 antibody to visualize microglia (red) and counter-stained with X-34 to visualize amyloid plaque deposition (blue). No clear difference in Iba-1 staining was present between vibrissae-deprived (left; **e**) and control (right; **f**) hemispheres ( $n = 6$ ). White rectangles in **a,d** denote barrel cortex. Scale bars in **a,d**, 1 mm; scale bars in **b,e**, 50  $\mu$ M.

## **Chapter 4.**

### **Bidirectional relationship between functional connectivity and amyloid- $\beta$ deposition in mouse brain**

## **PREFACE**

Adam W. Bero and Adam Q. Bauer (laboratory of Joseph P. Culver) contributed equally to the work in this chapter. Floy Stewart provided technical assistance.

## ABSTRACT

Brain region-specific deposition of amyloid plaques principally composed of extracellular aggregates of amyloid- $\beta$  ( $A\beta$ ) peptide is a pathological signature of Alzheimer's disease (AD). Recent human neuroimaging data suggest that resting-state functional connectivity strength is reduced in patients with AD, cognitively normal elderly harboring elevated amyloid burden, and in advanced aging. Interestingly, there exists a striking spatial correlation between functional connectivity strength in cognitively normal adults and the location of  $A\beta$  plaque deposition in AD. However, technical limitations have heretofore precluded examination of the relationship between functional connectivity,  $A\beta$  plaque deposition, and normal aging in mouse models. Using a novel functional connectivity optical intrinsic signal (fcOIS) imaging technique, we demonstrate that the magnitude of regional bilateral functional correlation in young APP/PS1 mice prior to  $A\beta$  plaque formation was proportional to the amount of region-specific plaque deposition seen later in older APP/PS1 mice. Furthermore, we found that  $A\beta$  plaque deposition is associated with significantly reduced bilateral functional connectivity in retrosplenial, frontal, cingulate, and motor cortices of older APP/PS1 transgenic mice. The degree of  $A\beta$  plaque deposition in each brain region was associated with local bilateral functional connectivity decline. Normal aging was associated with reduced bilateral functional connectivity specifically in retrosplenial cortex. Together, these findings suggest that the magnitude of local bilateral functional connectivity predicts regional vulnerability to subsequent  $A\beta$  plaque deposition and that  $A\beta$  plaque deposition and normal aging are associated with region-specific disruption of functional connectivity in mouse brain.

## INTRODUCTION

Alzheimer's disease (AD) is the most common cause of dementia, characterized by progressive structural and functional deterioration of higher-order neural networks. A histopathological hallmark of AD is the presence of extracellular plaques primarily composed of aggregated amyloid- $\beta$  ( $A\beta$ ) peptide. Under normal conditions,  $A\beta$  is produced in neurons and is present in the extracellular space of the brain in soluble form (Selkoe, 2001). During AD pathogenesis, soluble  $A\beta$  aggregates into  $A\beta$  oligomers and insoluble extracellular amyloid plaques in a concentration-dependent manner (Yan et al., 2009; Bero et al., 2011). In AD, amyloid plaque deposition is most prominent in the default-mode network, a network of brain areas in which metabolism is preferentially elevated during undirected mentation (Raichle et al., 2001; Buckner et al., 2005; Raichle and Mintun, 2006; Vaishnavi et al., 2010; Vlassenko et al., 2010). Interestingly, functional connectivity MRI (fcMRI) studies show that multiple regions of the default-mode network exhibit high intrinsic functional connectivity in healthy brain (Hagmann et al., 2008; Buckner et al., 2009). Moreover, recent data suggest that the relationship between functional connectivity and AD is bidirectional, as functional connectivity is disrupted in patients with AD (Supekar et al., 2008; Zhang et al., 2009), cognitively normal elderly with elevated amyloid burden (Hedden et al., 2009; Sheline et al., 2010a; Drzezga et al., 2011), and in advanced aging (Andrews-Hanna et al., 2007).

In mouse models of  $\beta$ -amyloidosis,  $A\beta$  plaque deposition is associated with myriad neurotoxic effects, including neuritic dystrophy, impaired synaptic integration and calcium dyshomeostasis (Knowles et al., 1999; D'Amore et al., 2003; Lombardo et al., 2003; Tsai et al., 2004; Brendza et al., 2005; Garcia-Alloza et al., 2006; Kuchibhotla

et al., 2008; Meyer-Luehmann et al., 2008; Kuchibhotla et al., 2009). However, because technical limitations have precluded examination of systems-level functional connectivity in model systems, the relationship between intrinsic functional connectivity, A $\beta$  plaque deposition and normal aging in mouse brain remains unclear. Given these limitations, we designed a novel functional connectivity optical intrinsic signal (fcOIS) imaging approach (White et al., 2011) wherein changes in reflected light intensity from the surface of the brain are converted to changes in local hemoglobin concentration and used to measure intrinsic functional connectivity. Herein, we utilize fcOIS to determine whether the magnitude of regional bilateral functional connectivity prior to plaque deposition is indicative of subsequent region-specific A $\beta$  plaque deposition. Additionally, we examine whether A $\beta$  plaque deposition or normal aging is associated with functional connectivity disruption in *APP<sup>swE</sup>/PS1 $\Delta$ E9* (APP/PS1) transgenic and wild-type mice, respectively.

## MATERIALS AND METHODS

**Animals.** Male *APP<sup>swe</sup>/PS1<sup>ΔE9</sup>* mice on a B6C3 background [APP/PS1(Jankowsky et al., 2004)] and B6C3 wild-type mice (The Jackson Laboratory) were aged to  $3.0 \pm 0.5$  or  $11.5 \pm 0.5$  months of age for experimentation. Mice were given *ab libitum* access to food and water. All experimental protocols were approved by the Animal Studies Committee at Washington University.

**Animal preparation.** In accord with our previously published animal preparation protocol for fcOIS imaging (White et al., 2011), all mice were anesthetized with ketamine-xylazine and allowed 15 minutes for anesthetic transition. In order to achieve a equivalent depth of anesthesia across groups (as assessed by responsiveness to hind paw pinch, anesthesia duration, respiratory rate, and heart rate), mice were administered the following doses of 86.9 mg/kg ketamine, 13.4 mg/kg xylazine: 3 month-old APP/PS1, 1X; 11.5 month-old APP/PS1, 1.25X; all wild-type, 1.5X. Once induced, the animal was placed on a heating pad maintained at 37°C via feedback from a rectal probe (mTCII, Cell Microcontrols) and its head secured in a stereotactic frame using a nose cone and ear bars. Scalp fur was shaved and cleaned, a midline incision was made along the top of the head and the scalp was reflected, exposing approximately 1 cm<sup>2</sup> of the skull. The skull of each mouse was left intact and kept moist via application of mineral oil prior to the first imaging session. Forty-five minutes of data were collected for 36 out of 37 imaging sessions, with each imaging session consisting of consecutive five-minute data sets. Anesthesia duration was approximately 70 minutes for all groups. Respiratory rate during imaging sessions was monitored to be 3-4 Hz for all groups. Heart rate (measured by Fourier analysis of the OIS time-courses collected from each mouse brain during

imaging sessions) was similar across all groups (3 month-old APP/PS1,  $3.3 \pm 0.4$  Hz; 11.5 month-old APP/PS1,  $4.2 \pm 0.3$  Hz; 3 month-old wild-type,  $3.9 \pm 0.2$  Hz; 11.5 month-old wild-type,  $4.4 \pm 0.3$  Hz).

**Imaging system.** Sequential illumination was provided at four wavelengths by a ring of light emitting diodes (LEDs) placed approximately 10 cm above the mouse's head. Diffuse reflected light was detected by a cooled, frame-transfer EMCCD camera (iXon 897, Andor Technologies); the LED ring and the camera were time-synchronized and controlled via computer using custom-written software (MATLAB, Mathworks) at a full frame rate of 30 Hz. The secured mouse was placed at the focal plane of both the camera and the LED ring and held in place with a stereotactic holder. The field-of-view was adjusted to be approximately  $1 \text{ cm}^2$  square for each mouse resulting in images covering the majority of the convexity of the cerebral cortex.

**Image processing.** Data from all mice were subject to an initial quality check prior to spectroscopic analysis. Data runs (5 minutes) in which reflected light level intensity (mean value over the brain) varied as a function of time by greater than 1% for any wavelength were discarded and excluded from further analysis. This preliminary analysis resulted in 15–45 minutes of data per mouse. For subsequent analysis, image light intensity at each wavelength was interpreted using the Modified Beer-Lambert Law, usually written as:  $\Phi(\mathbf{r},t) = \Phi_0 \cdot \exp(-\Delta\mu_a(\mathbf{r},t) \cdot L)$ . Here,  $\Phi(\mathbf{r},t)$  is the measured light intensity,  $\Phi_0$  is the baseline light intensity,  $\Delta\mu_a(\mathbf{r}, t)$  is the change in absorption coefficient due to hemodynamic changes, and  $L$  is the optical path length factor for photons in the tissue [calculated from Eqn. 34 as described (Arridge et al., 1992)]. As there is no pre-stimulus baseline in resting-state experimentation, we instead normalized

relative to the average light intensity at each pixel, resulting in differential measures of absorption at each wavelength:  $\Delta\mu_{a,\lambda}(\mathbf{r},t) = -\ln(\Phi_{\lambda}(\mathbf{r},t)/\langle \Phi_{0\lambda}(\mathbf{r},t) \rangle)/L_{\lambda}$ . Absorption coefficient data were converted to hemoglobin concentration changes by inverting the system of equations,  $\Delta\mu_{a,\lambda}(\mathbf{r},t) = E_{\lambda,i} \Delta[\text{Hb}_i](\mathbf{r},t)$  (where  $E$  is the extinction coefficient matrix (Prahl, 2002), and  $i$  runs over hemoglobin species). This inversion was performed using least-squares methods, yielding changes in oxy- and deoxy-hemoglobin at each pixel at each time point.

Since previous functional connectivity studies with diffuse optical tomography (White et al., 2009) showed similar maps using either  $\text{HbO}_2$  or  $\text{Hb}_R$  contrast, here we used only  $\Delta\text{HbO}_2$  data for the connectivity analyses. Data were filtered to the functional connectivity band (0.009-0.08 Hz) following previous human functional connectivity algorithms (Fox et al., 2005). After filtering, each pixel's time series was resampled from 30 Hz to 1 Hz, and all further analysis was performed only on those pixels labeled as brain. This procedure is necessary as every mouse's head is shaped differently, and the view of the brain exposed varied slightly between surgeries. Time traces of all pixels defined as brain were averaged to create a global brain signal. This global signal was regressed from each pixel's time trace to remove global sources of variance, as is common in human fMRI algorithms.

**Seed-based functional connectivity measures.** To investigate the strength of network correlations, we focused on bilateral connectivity between homotopic areas in contralateral hemispheres. Twelve seed locations were positioned at coordinates expected to correspond to the left and right, frontal, cingulate, motor, somatosensory, retrosplenial and visual cortices as described previously (White et al., 2011). Seed time-traces for the

full data sets of each mouse (ranging from 15 to 45 minutes) were calculated by averaging the time traces within 0.25 mm of the seed locus (containing approximately 30 pixels) of each seed location. Functional connectivity analysis was performed by correlating these time courses against the time course of every pixel in the brain. This procedure produces twelve functional connectivity maps over the mouse brain (one map per seed). These functional connectivity maps were then compressed to a 12x12 seed-to-seed correlation matrix by correlating each of the 12 seed time traces. Pearson  $r$  values were converted to Fisher  $Z$  measures using:  $Z(r) = \text{arctanh}(r)$ .

The above seed-to-seed correlation approach evaluates the functional connectivity between only six regions of the brain. To further examine the bilateral connectivity across the entire brain of each group of mice, 15 min of data were used from every mouse by concatenating three randomly chosen, five-minute sequences out of a mouse's data set. Each frame of the 15-minute image sequence (as well as the brain mask for that mouse) was then affine-transformed to a common atlas space (Franklin and Paxinos, 1996) determined by the positions of the junction between the coronal suture and sagittal suture (posterior to the olfactory bulb and cerebrum along midline) and the position of lambda. The stretch component for the anterior-posterior stretch was set equal to the medial-lateral stretch. The intersection of the brain masks from all mice was calculated and made symmetric by reflection across the midline allowing all subsequent comparisons across mice to be performed only on brain areas shared between all mice.

To create the bilateral connectivity maps (**Fig. 6**), the 15-minute data sets from all mice within a group were concatenated following transformation to create four larger data sets. Every pixel was then used as a seed (which had a time trace consisting of the

average of the 30 pixels around it as described above) and correlated against its corresponding contralateral pixel, resulting in a symmetric map of correlation strengths for each cohort.

**A $\beta$  plaque deposition.** Animals were transcardially perfused with chilled phosphate-buffered saline (PBS, pH 7.4) with 0.3% heparin immediately following the final fcOIS session. Brains were removed and postfixed in 4% paraformaldehyde at 4°C overnight. Following fixation, brains were cryoprotected in 30% sucrose in PBS at 4°C for 72 hours. Using a freezing sliding microtome (Microm), serial coronal sections (50- $\mu$ m section thickness) were collected from frontal cortex to caudal hippocampus. Sections (each separated by 300  $\mu$ m) were stained with biotinylated HJ3.4 (anti-A $\beta$ <sub>1-13</sub>, mouse monoclonal antibody generated in-house) to visualize A $\beta$  immunopositive plaques. Immunostained sections were scanned using a Nanozoomer slide scanner (Hamamatsu Photonics). Quantitative analysis of percentage area covered by immunopositive staining was performed as described previously (Kim et al., 2009b). Briefly, images of immunostained sections were exported with NDP viewer (Hamamatsu Photonics), converted to 8-bit grayscale using ACDSee Pro 2 software (ACD Systems), thresholded to highlight A $\beta$ -specific staining and analyzed using Image J software (National Institutes of Health). A mouse brain atlas (Franklin and Paxinos, 1996) was used to identify frontal, motor, somatosensory, cingulate, retrosplenial and visual cortices for quantitative analysis of A $\beta$  immunopositive staining.

**Statistical analysis.** Statistical significance was determined by two-tailed *t*-test if two groups were compared. When variance differed significantly between groups, Welch's *t*-test was used. One-way ANOVA followed by Tukey's *post hoc* test for multiple

comparisons were used when more than two groups were compared. All statistical analyses were performed using Prism version 5.00 for Windows (GraphPad). Values were accepted as significant if  $P < 0.05$ .

## RESULTS

### **Bilateral functional connectivity magnitude predicts region-specific A $\beta$ plaque deposition**

In human brain, there exists a striking spatial correlation between areas of elevated resting-state functional connectivity in cognitively normal adults and the topography of A $\beta$  plaque deposition in AD (Buckner et al., 2009). To examine the relationship between intrinsic functional connectivity and A $\beta$  plaque deposition in mouse brain, we utilized a novel fcOIS imaging approach to characterize the magnitude of bilateral functional connectivity in multiple brain systems of young ( $3.0 \pm 0.5$  months of age) APP/PS1 mice prior to the onset of plaque deposition. Seed-based time traces of  $\Delta\text{HbO}_2$  concentration in each region-of-interest were calculated and correlated with every pixel in the brain (Fig. 1A-F). We found that the magnitude of bilateral functional correlation in young APP/PS1 mouse brain was greatest in retrosplenial cortex ( $z(r)$ ,  $1.4 \pm 0.16$ ), intermediate in cingulate ( $0.96 \pm 0.9$ ), frontal ( $0.74 \pm 0.06$ ) and motor ( $0.99 \pm 0.13$ ) cortices, and low in somatosensory ( $0.49 \pm 0.06$ ) and visual ( $0.6 \pm 0.15$ ) cortices (Fig. 1G;  $n = 7$ ). A similar pattern of regional functional connectivity magnitude was observed in age-matched wild-type mice, suggesting that regional differences in bilateral functional connectivity are intrinsic to normal brain physiology ( $n = 13$ ; Fig. 2).

To determine whether regional bilateral functional connectivity magnitude in young APP/PS1 mice prior to plaque deposition was indicative of the regional vulnerability to A $\beta$  plaque deposition in older APP/PS1 mice, we next characterized the distribution of A $\beta$  immunopositive plaque deposition in older ( $11.5 \pm 0.5$  months of age)

APP/PS1 mouse brain. Brain sections were immunostained with biotinylated HJ3.4 antibody, to A $\beta$  amino acids 1-13 (anti-A $\beta_{1-13}$ ) to determine the percentage area occupied by A $\beta$  plaques in each region-of-interest (Fig. 3A-D). We found that A $\beta$  plaque deposition was greatest in retrosplenial cortex ( $18.01\% \pm 3.86$ ), intermediate in cingulate ( $9.04 \pm 2.97$ ), frontal ( $6.63 \pm 1.63$ ), motor ( $7.26 \pm 1.38$ ) cortices, and low in somatosensory ( $3.74 \pm 0.75$ ) and visual ( $5.16 \pm 0.69$ ) cortices (Fig. 2E;  $n = 4$ ). Bilateral functional connectivity magnitude in young APP/PS1 mice prior to plaque deposition was thus proportional to the amount of A $\beta$  plaque deposition in older APP/PS1 mice in a region-specific manner (Fig. 3F).

### **A $\beta$ plaque deposition and normal aging are associated with functional connectivity disruption**

Amyloid plaque deposition is associated with reduced resting-state functional connectivity in patients with AD (Supekar et al., 2008; Zhang et al., 2009) and cognitively normal adults who harbor significant amyloid load (Hedden et al., 2009; Sheline et al., 2010a; Drzezga et al., 2011). Therefore, we utilized fcOIS to determine whether A $\beta$  plaque deposition was associated with decreased functional connectivity in older ( $11.5 \pm 0.5$  months of age) APP/PS1 mice. Relative to 3 month old APP/PS1 mice, 11.5 month old APP/PS1 mice exhibited significant reductions in bilateral functional correlation strength in frontal ( $z(r)$ ,  $0.49 \pm 0.08$ ;  $P = 0.0298$ ), motor ( $0.48 \pm 0.15$ ;  $P = 0.0217$ ), cingulate ( $0.58 \pm 0.13$ ;  $P = 0.0312$ ) and retrosplenial ( $0.46 \pm 0.06$ ;  $P = 0.0009$ ) cortices. No significant differences were observed in somatosensory ( $0.32 \pm 0.12$ ;  $P = 0.2266$ ) or visual ( $0.21 \pm 0.1$ ;  $P = 0.0571$ ) cortices (Fig. 4A-G;  $n = 7$ ).

In humans, normal aging is associated with disruption of functional connectivity in multiple brain areas (Andrews-Hanna et al., 2007). We thus sought to determine whether normal aging was associated with reduced bilateral connectivity in older (11.5 ± 0.5 months old) B6C3 wild-type mice. Compared to young B6C3 wild-type mice, 11.5 month old wild-type mice exhibited a significant reduction in bilateral connectivity in retrosplenial cortex ( $z(r)$ , young,  $1.1 \pm 0.06$ ; 11.5 month,  $0.69 \pm 0.07$ ;  $P = 0.0002$ ). In contrast, comparisons of bilateral functional connectivity between young and 11.5 month old wild-type mice were not significant in frontal (young,  $0.81 \pm 0.1$ ; 11.5 month,  $0.71 \pm 0.09$ ;  $P = 0.4554$ ), motor (young,  $0.68 \pm 0.07$ ; 11.5 month,  $0.83 \pm 0.14$ ;  $P = 0.2954$ ), somatosensory (young,  $0.45 \pm 0.11$ ; 11.5 month,  $0.67 \pm 0.08$ ;  $P = 0.1438$ ), cingulate (young,  $0.99 \pm 0.09$ ; 11.5 month,  $1.0 \pm 0.09$ ;  $P = 0.9370$ ) or visual (young,  $0.42 \pm 0.08$ ; 11.5 month,  $0.52 \pm 0.1$ ;  $P = 0.4383$ ) cortex (Fig. 5A-G;  $n = 10-13$ /group).

To more closely examine the spatial relationship between A $\beta$  plaque deposition and age-related decline in bilateral functional connectivity in APP/PS1 mice, an equal number of fcOIS data sets from each mouse were affine-transformed to a common atlas space and concatenated before calculating the correlation between each bilateral pixel set in the brain. Thus, a single full-field consensus bilateral connectivity map was generated for each cohort (Fig. 6A,B,D,E). Notably, the consensus bilateral connectivity maps generated for each cohort qualitatively reproduce the regional differences in bilateral functional connectivity magnitude reported above. To examine pixel-wise, age-related changes in bilateral functional connectivity magnitude, bilateral correlation consensus values generated from older mice were subtracted from bilateral correlation consensus values generated from young mice of the same genotype. The resultant difference maps

reveal regional differences in the level of age-related functional decline in APP/PS1 (Fig. 6C) and wild-type (Fig. 6F) mice. In APP/PS1 mice, age-related decline in functional connectivity was greatest in retrosplenial cortex and lowest in somatosensory cortex (Fig. 6C). As the level of plaque deposition in older APP/PS1 mice was greatest in retrosplenial cortex and lowest in somatosensory cortex, this finding suggests that the amount of regional plaque deposition is linked with the level of age-related decline in local bilateral functional connectivity. In wild-type mice, retrosplenial cortex exhibited the greatest age-related decline in functional connectivity while subtle increases in bilateral functional correlation were observed in motor and somatosensory cortices (Fig. 6F). Together, these data suggest that bilateral functional connectivity in mouse brain is reduced in normal aging and is markedly exacerbated by A $\beta$  accumulation in the brain in a region-specific pattern.

## DISCUSSION

In human brain, there exists a striking spatial correlation between areas that exhibit disproportionately high resting-state functional connectivity in cognitively normal adults and the distribution of amyloid plaque deposition in AD (Buckner et al., 2009). Moreover, functional connectivity is decreased in AD and cognitively normal individuals who harbor elevated amyloid deposition (Supekar et al., 2008; Hedden et al., 2009; Zhang et al., 2009; Sheline et al., 2010a; Drzezga et al., 2011). Thus, elucidating the mechanisms that underlie the relationship between functional connectivity and A $\beta$  plaque deposition may inform AD pathobiology and potentially reveal novel therapeutic avenues. However, as the small size of mouse brain necessitates an exceptionally high signal-to-noise ratio to achieve sufficient spatial resolution for functional magnetic resonance imaging, the relationship between functional connectivity and A $\beta$  plaque deposition in mouse brain has remained unknown. Here, we utilize a novel fcOIS imaging approach (White et al., 2011) to characterize the relationship between functional connectivity, A $\beta$  plaque deposition, and normal aging in mouse brain. We found that bilateral functional connectivity magnitude varied significantly across brain regions of young APP/PS1 mice and that the magnitude of region-specific bilateral functional correlation in young APP/PS1 mice prior to the onset of A $\beta$  plaque formation was proportional to the density of regional plaque deposition in older APP/PS1 mice. This finding is consistent with human data suggesting that heteromodal association areas of the default-mode network exhibit disproportionately high intrinsic structural and functional connectivity in cognitively normal young adults and are among the brain regions most vulnerable to A $\beta$  deposition in AD (Hagmann et al., 2008; Buckner et al.,

2009). Importantly, as shown here, this OIS imaging approach combined with mouse models of neurodegeneration should allow for novel insights with regard to the role of specific genes/proteins in systems-level neural function.

Several reports have demonstrated that functional connectivity is impaired in AD and in cognitively normal elderly harboring significant amyloid plaque burden (Supekar et al., 2008; Hedden et al., 2009; Zhang et al., 2009; Sheline et al., 2010a; Drzezga et al., 2011). In accord with these human data, the present findings suggest that region-specific A $\beta$  accumulation is associated with significant reductions in bilateral functional connectivity magnitude in multiple brain systems of older APP/PS1 mice. Moreover, we observed that brain regions in which amyloid deposition was most prominent (e.g. retrosplenial cortex) exhibited greater age-related declines in functional connectivity relative to areas of lesser plaque deposition (e.g. somatosensory cortex). As A $\beta$  plaque deposition is associated with local neuritic dystrophy and impaired synaptic integration in APP transgenic mice (Knowles et al., 1999; D'Amore et al., 2003; Lombardo et al., 2003; Tsai et al., 2004; Brendza et al., 2005; Garcia-Alloza et al., 2006; Meyer-Luehmann et al., 2008) future application of fcOIS will permit examination of the molecular mechanisms that underlie the relationship between A $\beta$  plaque deposition and impaired systems-level functional connectivity.

In humans, normal age-related memory deficits are associated with decreased functional correlation between medial prefrontal cortex and posterior cingulate/retrosplenial cortex (Andrews-Hanna et al., 2007). Here, we found that retrosplenial cortex exhibits decreased bilateral functional connectivity in wild-type mice at 11.5 months of age. As age-related memory deficits are not present in wild-type mice

at this age, and given that retrosplenial cortex is important for learning and memory (Keene and Bucci, 2008, 2009; Corcoran et al., 2011), impaired bilateral functional connectivity in retrosplenial cortex may represent an early event in age-related neural dysfunction that ultimately results in memory impairment. In this context, fcOIS may serve as a useful tool to investigate the molecular mechanisms that contribute to decreased functional connectivity and memory dysfunction associated with normal aging.

Our laboratory has recently demonstrated that regional differences in endogenous neuronal activity are closely associated with interstitial fluid A $\beta$  levels and are a key determinant of region-specific A $\beta$  plaque deposition in APP transgenic mice (Bero et al., 2011). As the present data suggest that regional bilateral functional connectivity magnitude in young mice prior to plaque deposition is also associated with the level of subsequent A $\beta$  plaque deposition, it will be important to examine the relationship between neuronal population activity and systems-level functional connectivity and how these mechanisms may independently or coordinately regulate A $\beta$  metabolism.

A major challenge facing the neuroscience community is the paucity of clinically translatable assays that examine neural network function and integrity. Given that resting-state functional connectivity measures have provided valuable information regarding the functional organization of human brain (Fox and Raichle, 2007) and have yielded examples of how such organization is disrupted in disease (Zhang and Raichle, 2010), use of fcOIS in combination with genetic and molecular manipulations in mouse models provides an translational opportunity to elucidate mechanisms that underlie intrinsic functional connectivity in healthy brain and its disruption in models of neurological and neurodegenerative disorders. The clinically translatable nature of fcOIS

also positions this technique as a useful tool with which to examine the efficacy of pharmacological or behavioral interventions aimed to restore neural network integrity in such mouse models.

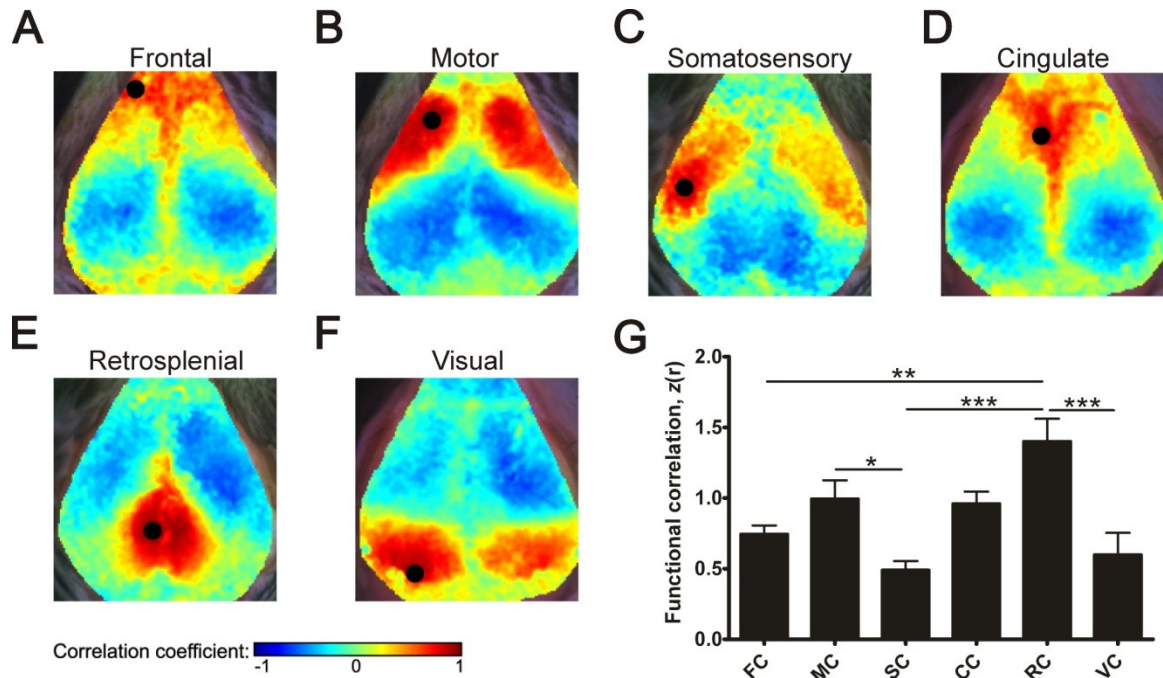


**Figure 1. fcOIS reveals regional differences in bilateral functional connectivity**

**magnitude in APP/PS1 mice prior to A $\beta$  plaque deposition.** *A-F*, Representative seed-based functional correlation maps of frontal (FC; *A*), motor (MC; *B*), somatosensory (SC; *C*), cingulate (CC; *D*), retrosplenial (RC; *E*) and visual (VC; *F*) cortices in  $3.0 \pm 0.5$  month-old APP/PS1 mice. Black circles denote seed position and size. Scale, Pearson  $r = -1$  to 1. *G*, Fisher  $z$ -transformed correlation values of bilateral functional correlation magnitude in each region of interest ( $n = 7/\text{group}$ ). \*,  $P < 0.05$ ; \*\*,  $P < 0.01$ ; \*\*\*,  $P < 0.001$  (one-way analysis of variance (ANOVA), Tukey's post hoc test for multiple comparisons). Values represent mean  $\pm$  s.e.m.

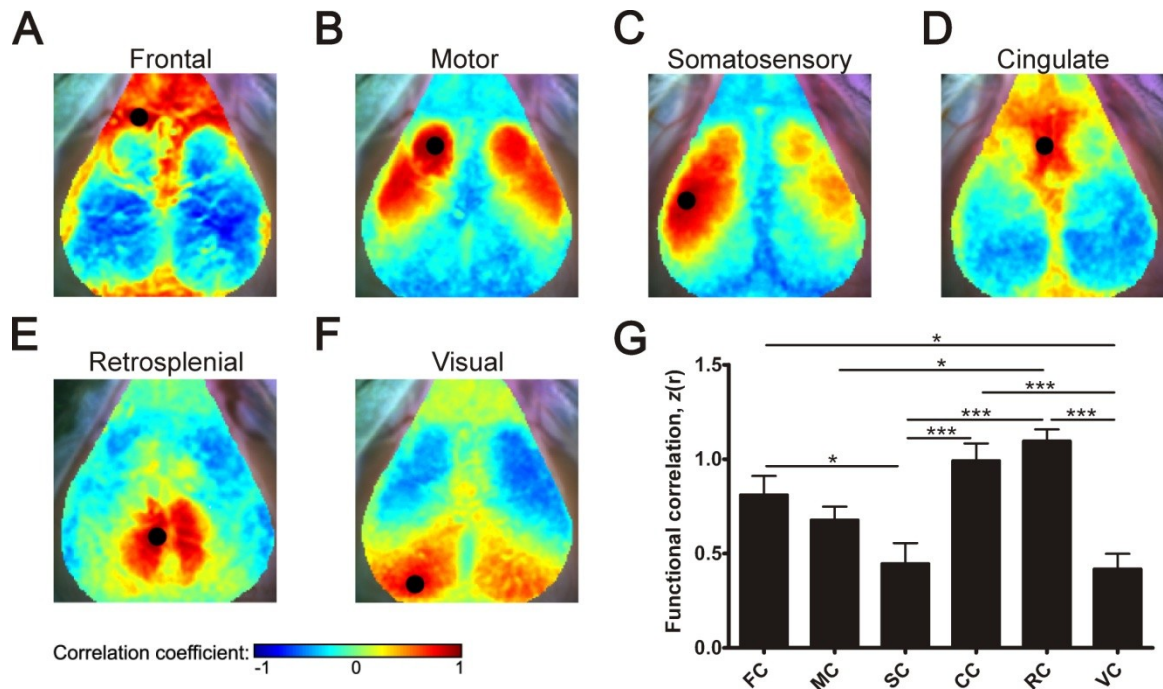


**Figure 2. fcOIS reveals regional differences in bilateral functional connectivity magnitude in young wild-type mice.** *A-F*, Representative seed-based functional correlation maps of frontal (FC; *A*), motor (MC; *B*), somatosensory (SC; *C*), cingulate (CC; *D*), retrosplenial (RC; *E*) and visual (VC; *F*) cortices in  $3.0 \pm 0.5$  month-old wild-type mice. Black circles denote seed position and size. Scale, Pearson  $r = -1$  to  $1$ . *G*, Fisher  $z$ -transformed correlation values of bilateral functional correlation magnitude in each region of interest ( $n = 13/\text{group}$ ). \*,  $P < 0.05$ ; \*\*\*,  $P < 0.001$  (one-way analysis of variance (ANOVA), Tukey's post hoc test for multiple comparisons). Values represent mean  $\pm$  s.e.m.

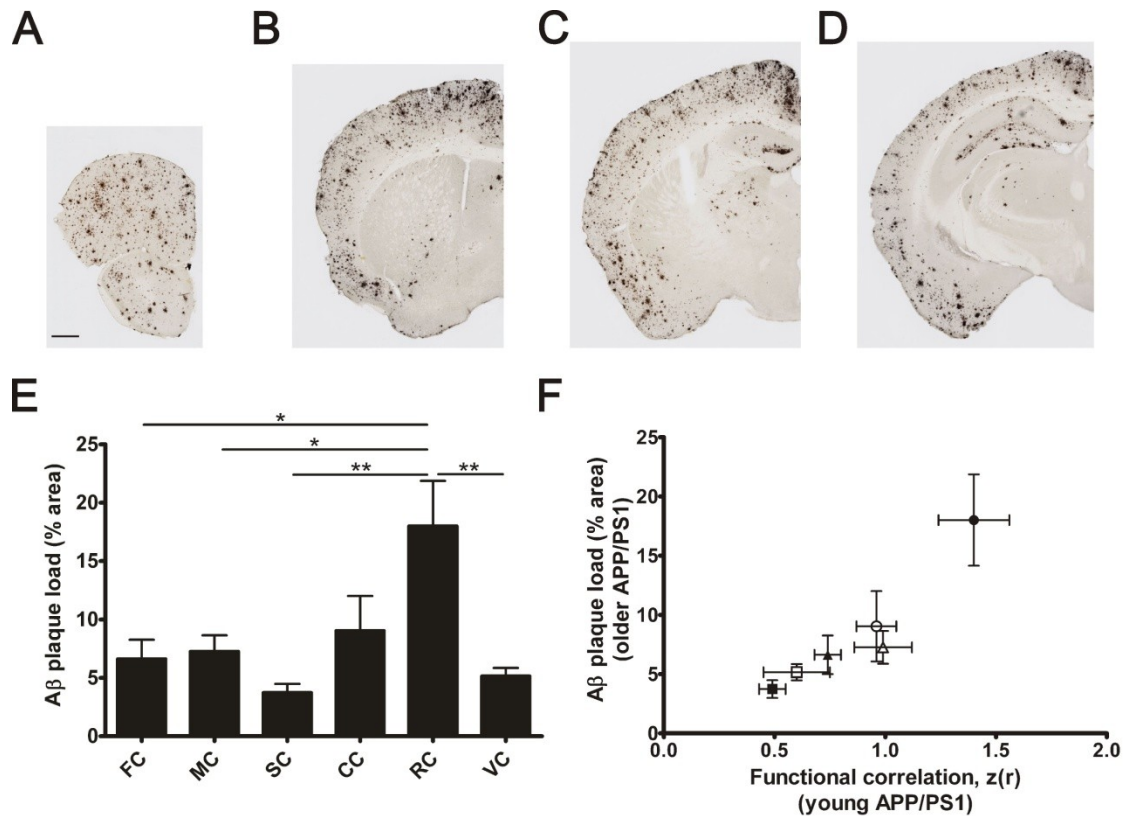


**Figure 3. Regional bilateral functional connectivity magnitude in young APP/PS1 mice is closely associated with regional plaque load in older APP/PS1 mice.** *A-D*, Representative brain sections from aged ( $11.5 \pm 0.5$  month-old) APP/PS1 mice stained with biotinylated HJ3.4 antibody (anti- $A\beta_{1-13}$ ) to visualize  $A\beta$  immunopositive plaques. Scale bar, 500  $\mu\text{m}$ . *E*, Percentage area occupied by  $A\beta$  deposition in frontal (FC), motor (MC), somatosensory (SC), cingulate (CC), retrosplenial (RC) and visual (VC) cortices ( $n = 4$  per group). *F*, Fisher  $z$ -transformed correlation values of bilateral functional correlation magnitude in frontal ( $\blacktriangle$ ), motor ( $\triangle$ ), somatosensory ( $\blacksquare$ ), cingulate ( $\circ$ ), retrosplenial ( $\bullet$ ) and visual ( $\square$ ) cortex of young APP/PS1 mice, plotted against subsequent  $A\beta$  plaque deposition in each brain region of aged APP/PS1 mice. \*,  $P <$

0.05; \*\*,  $P < 0.01$  (one-way ANOVA, Tukey's post hoc test for multiple comparisons).

Values represent mean  $\pm$  s.e.m.

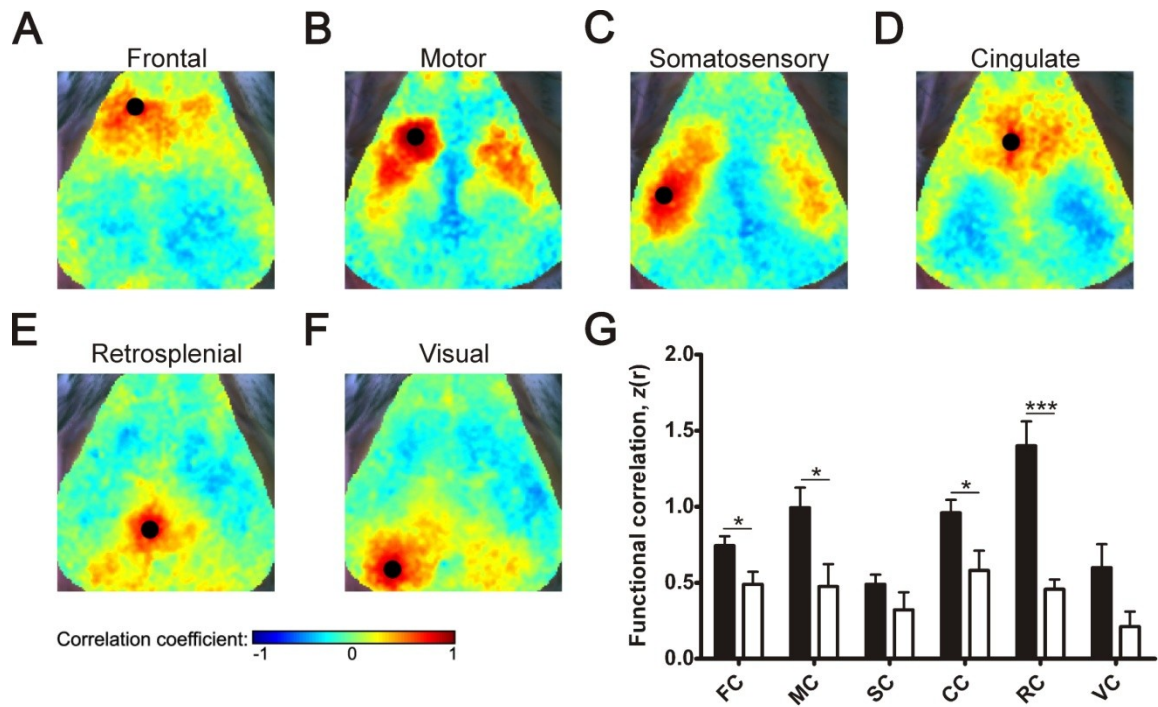


**Figure 4. A $\beta$  plaque deposition is associated with decreased functional connectivity magnitude in multiple brain systems of older APP/PS1 mice.** *A-F*, Representative seed-based functional correlation maps of frontal (FC; *A*), motor (MC; *B*), somatosensory (SC; *C*), cingulate (CC; *D*), retrosplenial (RC; *E*) and visual (VC; *F*) cortices in 11.5  $\pm$  0.5 month-old APP/PS1 mice. Black circles denote seed position and size. Scale, Pearson  $r = -1$  to 1. *G*, Fisher  $z$ -transformed correlation values of bilateral functional correlation magnitude in each region of interest in young (black bars) and older (white bars) APP/PS1 mice ( $n = 7$ /group). \*,  $P < 0.05$ ; \*\*\*,  $P < 0.001$  (one-way ANOVA, Tukey's post hoc test for multiple comparisons). Values represent mean  $\pm$  s.e.m.

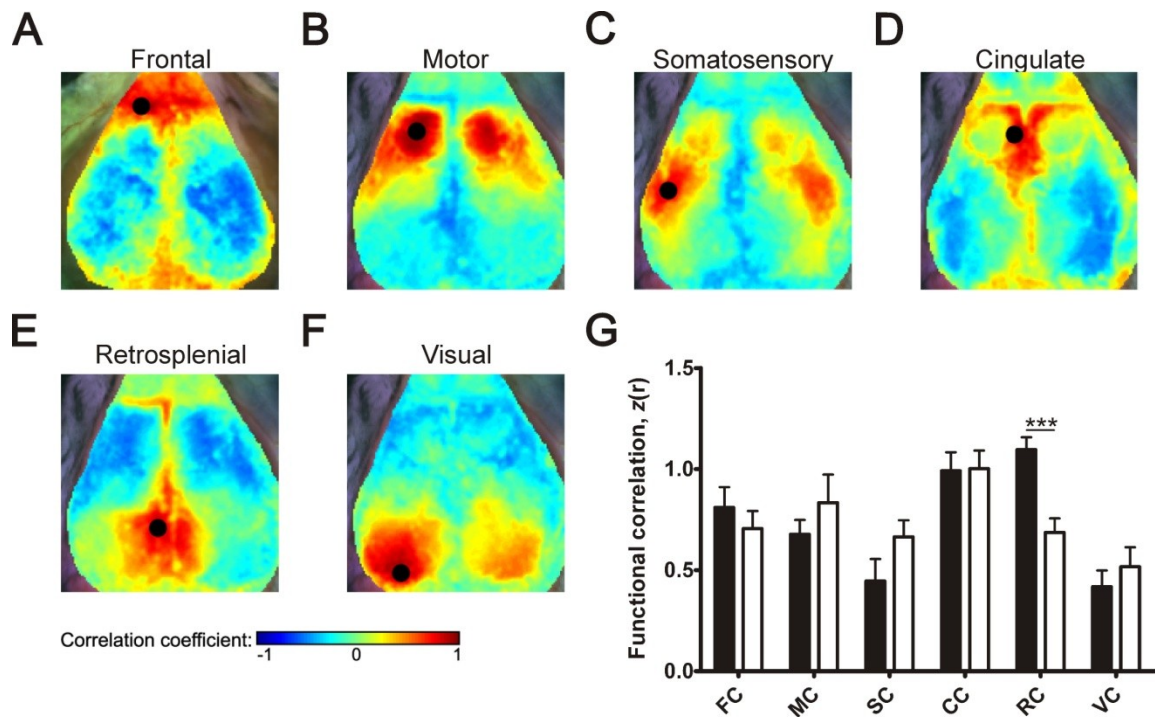


**Figure 5. Normal aging is associated with decreased functional connectivity magnitude in retrosplenial cortex.** *A-F*, Representative seed-based functional correlation maps of frontal (FC; *A*), motor (MC; *B*), somatosensory (SC; *C*), cingulate (CC; *D*), retrosplenial (RC; *E*) and visual (VC; *F*) cortices in  $11.5 \pm 0.5$  month-old wild-type mice. Black circles denote seed position and size. Scale, Pearson  $r = -1$  to  $1$ . *G*, Fisher  $z$ -transformed correlation values of bilateral functional correlation magnitude in each region of interest in young (black bars) and older (white bars) wild-type mice ( $n = 10-13$ /group). \*\*\*,  $P < 0.001$  (one-way ANOVA, Tukey's post hoc test for multiple comparisons). Values represent mean  $\pm$  s.e.m.

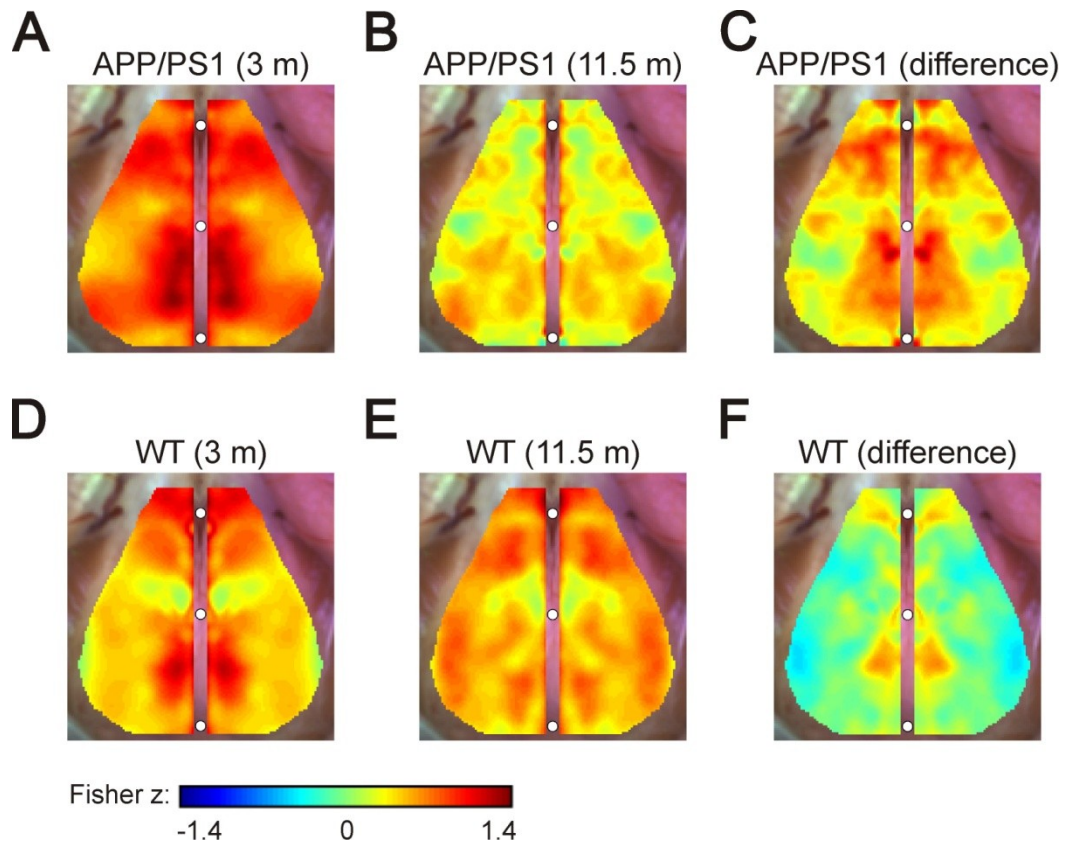


**Figure 6. Regional A $\beta$  plaque deposition is associated with degree of age-related decline in bilateral functional connectivity.** *A,B*, Consensus bilateral functional connectivity maps generated for young (*A*) and older (*B*) APP/PS1 mice. *C*, Difference map reveals region-specific, age-related decline in bilateral functional connectivity magnitude in APP/PS1 mice. *D,E*, Consensus bilateral functional connectivity maps generated for young (*D*) and older (*E*) wild-type mice. *F*, Difference map reveals region-specific, age-related decline in bilateral functional connectivity magnitude in wild-type mice. Scale in *A,B,D,E*, Fisher  $z = -1.4$  to  $1.4$ . Note that in *C,F*, positive values represent age-related decline, while negative values represent age-related increase, in bilateral functional connectivity magnitude.

## **Chapter 5.**

### **Conclusions and future directions**

## Summary

As amyloid plaque deposition is a necessary event in AD pathogenesis, we sought to elucidate the factors that regulate cerebral amyloid plaque growth *in vivo* (Chapter 2 of this dissertation). Using intravital multiphoton microscopy through a thinned-skull cranial window in APP/PS1 bitransgenic mice, we found that amyloid plaques present in cortex of 6 month-old APP/PS1 mice exhibited significant growth over a period of weeks, while significant amyloid plaque growth was not present in 10 month-old APP/PS1 mice. In contrast, plaques imaged through an open-skull cranial window did not exhibit significant growth at either age, likely due to increased cortical gliosis in open-skull window preparations. Under thinned-skull window preparations, plaque growth rate was inversely proportional to initial plaque size in 6 and 10 month-old mice. Amyloid plaque formation and growth were prevented by pharmacological  $\gamma$ -secretase inhibition. *In vivo* microdialysis experiments performed in young APP/PS1 mice showed that reduction of ISF A $\beta$  levels by 20-25% over the course of 24 hours was associated with a dramatic reduction in amyloid plaque formation and growth. Together, these data suggest that amyloid plaque formation and growth *in vivo* occurs over weeks and is closely related to animal age, initial plaque size and ISF A $\beta$  concentration.

Though region-specific deposition of A $\beta$  plaques is a fundamental feature of AD, the mechanisms that regulate the regional vulnerability to A $\beta$  plaque deposition in AD remain unknown. We sought to address this issue in Chapter 3 of this dissertation. Using *in vivo* microdialysis, we found that the steady-state concentrations of ISF A $\beta_{x-40}$  and A $\beta_{x-42}$  in young Tg2576 mice prior to the onset of plaque deposition were closely associated with the spatial distribution of A $\beta$  deposition in aged mice. We found that ISF lactate

level was a valid marker of neuronal activity *in vivo* and that regional ISF lactate levels in young Tg2576 mice were closely associated with regional ISF A $\beta$  levels and subsequent region-specific A $\beta$  and amyloid plaque deposition. We found that region-specific A $\beta$  plaque deposition was not predicted by ISF A $\beta$  clearance rate, full-length APP expression or APP processing. To determine whether physiological neuronal activity directly regulates ISF A $\beta$  levels, we used *in vivo* microdialysis to determine the effect of unilateral vibrissal trimming or stimulation on ISF A $\beta$  levels in contralateral barrel cortex of young Tg2576 mice. We found that unilateral vibrissal trimming acutely reduced, and unilateral vibrissal stimulation acutely increased, ISF A $\beta$  levels in contralateral barrel cortex. Using multiphoton microscopy, we found that long-term unilateral vibrissal trimming significantly reduced amyloid plaque formation and growth in contralateral barrel cortex. The results presented in Chapter 3 thus suggest that regional differences in steady-state neuronal activity regulate region-specific A $\beta$  plaque deposition through long-term modulation of ISF A $\beta$  concentration.

In Chapter 4, we sought to examine the relationship between functional connectivity, A $\beta$  plaque deposition and normal aging in mouse brain. As technical limitations have heretofore precluded examination of systems-level functional connectivity in mouse brain, we utilized a novel fcOIS technique (White et al., 2011) to conduct the first study of systems-level functional connectivity in a mouse model of neuropathology or normal aging. We found that regional differences in bilateral functional connectivity magnitude were present in young APP/PS1 and wild-type mice. Interestingly, bilateral functional connectivity magnitude in young APP/PS1 mice was proportional to region-specific A $\beta$  plaque deposition in aged APP/PS1 mice. The

relationship between functional connectivity and A $\beta$  plaque deposition appeared to be bidirectional, as we found that A $\beta$  deposition was associated with marked reductions in bilateral functional connectivity magnitude in several brain systems of aged APP/PS1 mice. In wild-type mice, normal aging was associated with a specific decrease in bilateral functional connectivity in retrosplenial cortex. Finally, we found that the degree of regional functional connectivity decline in aged APP/PS1 mouse brain was associated with the amount of region-specific A $\beta$  plaque deposition. These data suggest a close relationship between functional connectivity, A $\beta$  deposition and normal aging in mouse brain and provide a foundation for future investigation of the molecular mechanisms that underlie systems-level neural network dysfunction.

## Super-resolution examination of AD pathogenesis

Since the seminal work of Santiago Ramón y Cajal, microscopic analysis of brain tissue has yielded fundamental insights into brain structure, function and the mechanisms by which pathological insults disrupt neural integrity. Until recently however, the diffraction limit of light has prevented molecular-level visualization of specific biomolecules in tissue sections. The advent of super-resolution fluorescence microscopy techniques such as stochastic optical reconstruction microscopy (STORM) now permits nanometer level examination of specific molecules in biological samples (Dani and Huang, 2010; Dani et al., 2010).

In Chapter 3 of this dissertation, we found that regional differences in steady-state neuronal activity regulate brain region-specific ISF A $\beta$  levels and amyloid plaque growth dynamics *in vivo*. However, the mechanisms that regulate intrinsic differences in regional neuronal activity remain unclear. As synaptic vesicle exocytosis is necessary for neuronal activity-dependent A $\beta$  secretion (Cirrito et al., 2005), molecular-level examination of synaptic protein expression across brain regions may provide valuable insights into the mechanisms that regulate region-specific A $\beta$  plaque deposition. To this end, we have begun to use STORM to quantify markers of synapse density and neurotransmitter receptor composition (including GluR1, GluR1-Ser831-P, NR2A and CamKII-P) across cortical regions that exhibit differential susceptibility to A $\beta$  plaque deposition. We hypothesize that synapse density and neurotransmitter receptor expression density in each brain region of young APP transgenic mice prior to the onset of plaque deposition will be proportional to the amount of region-specific A $\beta$  plaque deposition in aged APP transgenic mice. Our *in vivo* microdialysis data suggest that

regional differences in neuronal activity present in young APP transgenic mice are similar to those present in wild-type mice (Chapter 3 of this dissertation). Using STORM, we will also examine synapse density and neurotransmitter receptor expression across brain regions of young wild-type mice to determine whether regional differences in synaptic architecture present in young APP transgenic mice are intrinsic to normal brain physiology or are affected by overproduction of full-length APP or APP cleavage derivatives such as A $\beta$ .

It is well-established that A $\beta$  plaque deposition is associated with synaptic loss in AD brain (Terry et al., 1991; Coleman and Yao, 2003) and mouse models of A $\beta$  deposition (Koffie et al., 2009). However, technical limitations have heretofore precluded molecular-level examination of the effect of A $\beta$  deposition on synaptic architecture in intact tissue. Therefore it will be of interest to use STORM to image synaptic protein expression in brain sections from aged APP transgenic mice that harbor A $\beta$  plaque deposition and age-matched wild-type controls to examine whether A $\beta$  deposition is associated with reduced local synapse density and neurotransmitter receptor expression. Anti-A $\beta$  immunotherapy has been shown to prevent and remove cerebral A $\beta$  deposition in APP transgenic mice (Schenk et al., 1999; Bard et al., 2000; Wilcock et al., 2004; Brody and Holtzman, 2008). Therefore, if A $\beta$  plaque deposition is found to be associated with local reductions in synapse density and neurotransmitter receptor expression, a potential follow-up experiment would be to determine whether systemic anti-A $\beta$  immunotherapy can prevent or reverse synaptic disruption in aged APP transgenic mice.

Moreover, STORM could be used to determine whether regional differences in the level of synaptic structural disruption are present in aged APP transgenic mice. If regional differences in synaptic disruption are present in aged APP transgenic mice, this result would provide an opportunity to link molecular-level structural disruption with systems-level functional dysfunction by examining whether the degree of molecular-level synaptic structural disruption in each brain region assessed by STORM is proportional to the degree of bilateral functional connectivity disruption in aged APP transgenic mice assessed by fcOIS.

### **Mechanisms of functional connectivity disruption in AD**

Using a novel fcOIS approach, we found that A $\beta$  plaque deposition is closely associated with region-specific functional connectivity decline in APP/PS1 mouse brain (Chapter 4 of this dissertation). As the experiments described in Chapter 4 were designed to determine whether A $\beta$  plaque deposition was spatially correlated with decreased functional connectivity magnitude, whether A $\beta$  aggregation is directly responsible for the observed functional connectivity decline in aged APP/PS1 mice remains unclear. Therefore, we have begun experiments to test whether systemic passive anti-A $\beta$  immunotherapy in Tg2576 mice prior to the onset of robust plaque deposition prevents functional connectivity decline relative to vehicle-treated, age-matched Tg2576 mice. Since systemic anti-A $\beta$  immunotherapy has also been suggested to clear existing A $\beta$  plaques from the brain, one potential follow-up experiment would be to begin anti-A $\beta$  immunotherapy in Tg2576 mice that harbor robust plaque deposition to determine whether A $\beta$  plaque removal rescues functional connectivity dysfunction once significant A $\beta$  plaque deposition has occurred.

Since AD is characterized by the presence of multiple neuropathological hallmarks, including amyloid plaque deposition, tau hyperphosphorylation and neurofibrillary tangle formation, one limitation of functional neuroimaging experiments in AD patients is the inability to attribute functional deficits to specific components of the disease process. However, given that we have recently utilized fcOIS to perform the first systems-level functional connectivity experiments in a mouse model of neuropathology (Chapter 4 of this dissertation), it is now possible to examine neural network function in transgenic mice that model specific neuropathological components of the AD process. In this context, it would be of interest to utilize fcOIS to examine whether tau hyperphosphorylation or neurofibrillary tangle formation is associated with decreased functional connectivity magnitude in a transgenic mouse model of tauopathy such as P301S (Yoshiyama et al., 2007). Although a comprehensive examination of regional differences in tau hyperphosphorylation and intracellular inclusion formation in P301S mice has not yet been performed, available data suggest that this model harbors relatively severe tau pathology in hippocampus and select cortical regions. Given the dense projections of hippocampus to retrosplenial cortex (Wyss and Van Groen, 1992), bilateral functional connectivity magnitude may be particularly decreased in retrosplenial cortex of P301S mice. Data suggest that tau immunotherapy can reduce tau hyperphosphorylation and aggregation in a mouse model of tauopathy (Boutajangout et al., 2010). Thus, if tau hyperphosphorylation and neurofibrillary tangle formation are shown to be associated with decreased functional connectivity magnitude, it would be interesting to determine whether tau immunotherapy can prevent or reverse functional connectivity dysfunction in mouse models of tauopathy.

Differential regulation of A $\beta$  clearance is widely hypothesized to represent a principle mechanism by which apoE isoforms differentially modulate susceptibility to AD (Castellano et al., 2011). Interestingly, human functional neuroimaging data suggest that resting-state and task-induced brain activation are upregulated in  $\epsilon$ 4 carriers relative to non-carriers prior to and following cerebral amyloid deposition (Bookheimer et al., 2000; Filippini et al., 2009). Moreover, functional connectivity abnormalities have been reported in cognitively normal  $\epsilon$ 4 carriers relative to noncarriers (Fleisher et al., 2009; Sheline et al., 2010b; Machulda et al., 2011) and human  $\epsilon$ 4 knock-in mice exhibit reduced excitatory synaptic transmission and reduced dendritic spine density in certain brain regions (Wang et al., 2005). Therefore, altered brain activity and functional connectivity may represent an additional mechanism by which  $\epsilon$ 4 modulates AD risk. In this context, it would be of interest to utilize fcOIS to determine whether human  $\epsilon$ 2,  $\epsilon$ 3 or  $\epsilon$ 4 knock-in mice exhibit differential functional connectivity magnitude in the absence of A $\beta$  pathology and whether normal age-related changes in functional connectivity magnitude are altered in an isoform-dependent manner. Moreover, using APP transgenic mice crossed with human  $\epsilon$ 2,  $\epsilon$ 3 or  $\epsilon$ 4 knock-in mice (Bales et al., 2009), it would be interesting to determine whether apoE isoform-dependent differences in steady-state ISF A $\beta$  levels present throughout life and resultant differences in A $\beta$  plaque deposition in aged mice (Castellano et al., 2011) are associated with differential functional connectivity magnitude.

## Concluding remarks

Brain region-specific deposition of extracellular A $\beta$  plaques is a pathological hallmark of AD. However, the mechanisms that regulate the regional vulnerability to A $\beta$  plaque deposition in AD remain unknown. In this thesis, we utilized mouse models of cerebral A $\beta$  deposition to examine molecular, cellular and systems-level mechanisms that regulate brain region-specific A $\beta$  accumulation and aggregation. We found that amyloid plaque formation and growth is closely related to ISF A $\beta$  concentration and that local steady-state neuronal activity levels regulate region-specific ISF A $\beta$  levels and A $\beta$  plaque deposition *in vivo*. Using a novel fcOIS technique, we also provide the first examination of systems-level functional connectivity in a mouse model of neuropathology or normal aging. We found that regional bilateral functional connectivity magnitude in young mice prior to the onset of A $\beta$  deposition was proportional to the amount of region-specific A $\beta$  deposition in aged mice. Moreover, we found that normal aging, and to a greater extent, A $\beta$  deposition, were associated with marked decreases in bilateral functional connectivity. Together, these findings advance our understanding of the mechanisms by which specific brain regions are rendered vulnerable to A $\beta$  plaque deposition in AD and suggest that intrinsic brain metabolism and functional organization may contribute to AD pathogenesis.

## References

- Alzheimer A, Stelzmann RA, Schnitzlein HN, Murtagh FR (1995) An English translation of Alzheimer's 1907 paper, "Über eine eigenartige Erkrankung der Hirnrinde". *Clin Anat* 8:429-431.
- Andrews-Hanna JR, Snyder AZ, Vincent JL, Lustig C, Head D, Raichle ME, Buckner RL (2007) Disruption of large-scale brain systems in advanced aging. *Neuron* 56:924-935.
- Arridge SR, Cope M, Delpy DT (1992) The theoretical basis for the determination of optical pathlengths in tissue: temporal and frequency analysis. *Phys Med Biol* 37:1531-1560.
- Ashe KH, Zahs KR (2010) Probing the biology of Alzheimer's disease in mice. *Neuron* 66:631-645.
- Bahmanyar S, Higgins GA, Goldgaber D, Lewis DA, Morrison JH, Wilson MC, Shankar SK, Gajdusek DC (1987) Localization of amyloid beta protein messenger RNA in brains from patients with Alzheimer's disease. *Science* 237:77-80.
- Bales KR, Liu F, Wu S, Lin S, Koger D, DeLong C, Hansen JC, Sullivan PM, Paul SM (2009) Human APOE isoform-dependent effects on brain beta-amyloid levels in PDAPP transgenic mice. *J Neurosci* 29:6771-6779.
- Bard F et al. (2000) Peripherally administered antibodies against amyloid beta-peptide enter the central nervous system and reduce pathology in a mouse model of Alzheimer disease. *Nat Med* 6:916-919.
- Bero AW, Yan P, Roh JH, Cirrito JR, Stewart FR, Raichle ME, Lee JM, Holtzman DM (2011) Neuronal activity regulates the regional vulnerability to amyloid-beta deposition. *Nat Neurosci*.
- Bigl M, Apelt J, Lushekina EA, Lange-Dohna C, Rossner S, Schliebs R (2000) Expression of beta-secretase mRNA in transgenic Tg2576 mouse brain with Alzheimer plaque pathology. *Neurosci Lett* 292:107-110.
- Biswal B, Yetkin FZ, Haughton VM, Hyde JS (1995) Functional connectivity in the motor cortex of resting human brain using echo-planar MRI. *Magnetic resonance in medicine : official journal of the Society of Magnetic Resonance in Medicine / Society of Magnetic Resonance in Medicine* 34:537-541.
- Bolmont T, Haiss F, Eicke D, Radde R, Mathis CA, Klunk WE, Kohsaka S, Jucker M, Calhoun ME (2008) Dynamics of the microglial/amyloid interaction indicate a role in plaque maintenance. *J Neurosci* 28:4283-4292.
- Bolmont T, Clavaguera F, Meyer-Luehmann M, Herzig MC, Radde R, Staufenbiel M, Lewis J, Hutton M, Tolnay M, Jucker M (2007) Induction of tau pathology by intracerebral infusion of amyloid-beta -containing brain extract and by amyloid-beta deposition in APP x Tau transgenic mice. *Am J Pathol* 171:2012-2020.
- Bookheimer SY, Strojwas MH, Cohen MS, Saunders AM, Pericak-Vance MA, Mazziotta JC, Small GW (2000) Patterns of brain activation in people at risk for Alzheimer's disease. *N Engl J Med* 343:450-456.
- Borchelt DR, Ratovitski T, van Lare J, Lee MK, Gonzales V, Jenkins NA, Copeland NG, Price DL, Sisodia SS (1997) Accelerated amyloid deposition in the brains of

- transgenic mice coexpressing mutant presenilin 1 and amyloid precursor proteins. *Neuron* 19:939-945.
- Boutajangout A, Quartermain D, Sigurdsson EM (2010) Immunotherapy targeting pathological tau prevents cognitive decline in a new tangle mouse model. *J Neurosci* 30:16559-16566.
- Braakman N, Matysik J, van Duinen SG, Verbeek F, Schliebs R, de Groot HJ, Alia A (2006) Longitudinal assessment of Alzheimer's beta-amyloid plaque development in transgenic mice monitored by in vivo magnetic resonance microimaging. *J Magn Reson Imaging* 24:530-536.
- Brendza RP, Bacskai BJ, Cirrito JR, Simmons KA, Skoch JM, Klunk WE, Mathis CA, Bales KR, Paul SM, Hyman BT, Holtzman DM (2005) Anti-Abeta antibody treatment promotes the rapid recovery of amyloid-associated neuritic dystrophy in PDAPP transgenic mice. *J Clin Invest* 115:428-433.
- Brody DL, Holtzman DM (2008) Active and passive immunotherapy for neurodegenerative disorders. *Annu Rev Neurosci* 31:175-193.
- Buckner RL, Kelley WM, Petersen SE (1999) Frontal cortex contributes to human memory formation. *Nat Neurosci* 2:311-314.
- Buckner RL, Andrews-Hanna JR, Schacter DL (2008) The brain's default network: anatomy, function, and relevance to disease. *Ann N Y Acad Sci* 1124:1-38.
- Buckner RL, Sepulcre J, Talukdar T, Krienen FM, Liu H, Hedden T, Andrews-Hanna JR, Sperling RA, Johnson KA (2009) Cortical hubs revealed by intrinsic functional connectivity: mapping, assessment of stability, and relation to Alzheimer's disease. *J Neurosci* 29:1860-1873.
- Buckner RL, Snyder AZ, Shannon BJ, LaRossa G, Sachs R, Fotenos AF, Sheline YI, Klunk WE, Mathis CA, Morris JC, Mintun MA (2005) Molecular, structural, and functional characterization of Alzheimer's disease: evidence for a relationship between default activity, amyloid, and memory. *J Neurosci* 25:7709-7717.
- Burdick D, Soreghan B, Kwon M, Kosmoski J, Knauer M, Henschen A, Yates J, Cotman C, Glabe C (1992) Assembly and aggregation properties of synthetic Alzheimer's A4/beta amyloid peptide analogs. *J Biol Chem* 267:546-554.
- Busche MA, Eichhoff G, Adelsberger H, Abramowski D, Wiederhold KH, Haass C, Staufenbiel M, Konnerth A, Garaschuk O (2008) Clusters of hyperactive neurons near amyloid plaques in a mouse model of Alzheimer's disease. *Science* 321:1686-1689.
- Buxbaum JD, Oishi M, Chen HI, Pinkas-Kramarski R, Jaffe EA, Gandy SE, Greengard P (1992) Cholinergic agonists and interleukin 1 regulate processing and secretion of the Alzheimer beta/A4 amyloid protein precursor. *Proc Natl Acad Sci U S A* 89:10075-10078.
- Buxbaum JD, Thinakaran G, Koliatsos V, O'Callahan J, Slunt HH, Price DL, Sisodia SS (1998) Alzheimer amyloid protein precursor in the rat hippocampus: transport and processing through the perforant path. *J Neurosci* 18:9629-9637.
- Castellano JM, Kim J, Stewart FR, Jiang H, DeMattos RB, Patterson BW, Fagan AM, Morris JC, Mawuenyega KG, Cruchaga C, Goate AM, Bales KR, Paul SM, Bateman RJ, Holtzman DM (2011) Human apoE isoforms differentially regulate brain amyloid-beta peptide clearance. *Science translational medicine* 3:89ra57.

- Christie RH, Bacskai BJ, Zipfel WR, Williams RM, Kajdasz ST, Webb WW, Hyman BT (2001) Growth arrest of individual senile plaques in a model of Alzheimer's disease observed by in vivo multiphoton microscopy. *J Neurosci* 21:858-864.
- Cirrito JR, Kang JE, Lee J, Stewart FR, Verges DK, Silverio LM, Bu G, Mennerick S, Holtzman DM (2008) Endocytosis is required for synaptic activity-dependent release of amyloid-beta in vivo. *Neuron* 58:42-51.
- Cirrito JR, Yamada KA, Finn MB, Sloviter RS, Bales KR, May PC, Schoepp DD, Paul SM, Mennerick S, Holtzman DM (2005) Synaptic activity regulates interstitial fluid amyloid-beta levels in vivo. *Neuron* 48:913-922.
- Cirrito JR, May PC, O'Dell MA, Taylor JW, Parsadanian M, Cramer JW, Audia JE, Nissen JS, Bales KR, Paul SM, DeMattos RB, Holtzman DM (2003) In vivo assessment of brain interstitial fluid with microdialysis reveals plaque-associated changes in amyloid-beta metabolism and half-life. *J Neurosci* 23:8844-8853.
- Coleman PD, Yao PJ (2003) Synaptic slaughter in Alzheimer's disease. *Neurobiol Aging* 24:1023-1027.
- Corcoran KA, Donnan MD, Tronson NC, Guzman YF, Gao C, Jovasevic V, Guedea AL, Radulovic J (2011) NMDA Receptors in Retrosplenial Cortex Are Necessary for Retrieval of Recent and Remote Context Fear Memory. *J Neurosci* 31:11655-11659.
- Corder EH, Saunders AM, Strittmatter WJ, Schmechel DE, Gaskell PC, Small GW, Roses AD, Haines JL, Pericak-Vance MA (1993) Gene dose of apolipoprotein E type 4 allele and the risk of Alzheimer's disease in late onset families. *Science* 261:921-923.
- Craig-Schapiro R, Perrin RJ, Roe CM, Xiong C, Carter D, Cairns NJ, Mintun MA, Peskind ER, Li G, Galasko DR, Clark CM, Quinn JF, D'Angelo G, Malone JP, Townsend RR, Morris JC, Fagan AM, Holtzman DM (2010) YKL-40: a novel prognostic fluid biomarker for preclinical Alzheimer's disease. *Biol Psychiatry* 68:903-912.
- D'Amore JD, Kajdasz ST, McLellan ME, Bacskai BJ, Stern EA, Hyman BT (2003) In vivo multiphoton imaging of a transgenic mouse model of Alzheimer disease reveals marked thioflavine-S-associated alterations in neurite trajectories. *J Neuropathol Exp Neurol* 62:137-145.
- Dani A, Huang B (2010) New resolving power for light microscopy: applications to neurobiology. *Current opinion in neurobiology* 20:648-652.
- Dani A, Huang B, Bergan J, Dulac C, Zhuang X (2010) Superresolution imaging of chemical synapses in the brain. *Neuron* 68:843-856.
- De Strooper B, Saftig P, Craessaerts K, Vanderstichele H, Guhde G, Annaert W, Von Figura K, Van Leuven F (1998) Deficiency of presenilin-1 inhibits the normal cleavage of amyloid precursor protein. *Nature* 391:387-390.
- De Strooper B, Annaert W, Cupers P, Saftig P, Craessaerts K, Mumm JS, Schroeter EH, Schrijvers V, Wolfe MS, Ray WJ, Goate A, Kopan R (1999) A presenilin-1-dependent gamma-secretase-like protease mediates release of Notch intracellular domain. *Nature* 398:518-522.
- Drzezga A, Becker JA, Van Dijk KR, Sreenivasan A, Talukdar T, Sullivan C, Schultz AP, Sepulcre J, Putcha D, Greve D, Johnson KA, Sperling RA (2011) Neuronal

- dysfunction and disconnection of cortical hubs in non-demented subjects with elevated amyloid burden. *Brain* 134:1635-1646.
- Durham D, Woolsey TA (1978) Acute whisker removal reduces neuronal activity in barrels of mouse SmL cortex. *J Comp Neurol* 178:629-644.
- Eisele YS, Obermuller U, Heilbronner G, Baumann F, Kaeser SA, Wolburg H, Walker LC, Staufenbiel M, Heikenwalder M, Jucker M (2010) Peripherally applied Abeta-containing inoculates induce cerebral beta-amyloidosis. *Science* 330:980-982.
- El Khoury J, Toft M, Hickman SE, Means TK, Terada K, Geula C, Luster AD (2007) Ccr2 deficiency impairs microglial accumulation and accelerates progression of Alzheimer-like disease. *Nat Med* 13:432-438.
- Engler H, Forsberg A, Almkvist O, Blomquist G, Larsson E, Savitcheva I, Wall A, Ringheim A, Langstrom B, Nordberg A (2006) Two-year follow-up of amyloid deposition in patients with Alzheimer's disease. *Brain* 129:2856-2866.
- Fagan AM, Roe CM, Xiong C, Mintun MA, Morris JC, Holtzman DM (2007) Cerebrospinal fluid tau/beta-amyloid(42) ratio as a prediction of cognitive decline in nondemented older adults. *Arch Neurol* 64:343-349.
- Fagan AM, Mintun MA, Mach RH, Lee SY, Dence CS, Shah AR, LaRossa GN, Spinner ML, Klunk WE, Mathis CA, DeKosky ST, Morris JC, Holtzman DM (2006) Inverse relation between in vivo amyloid imaging load and cerebrospinal fluid Abeta42 in humans. *Ann Neurol* 59:512-519.
- Filippini N, MacIntosh BJ, Hough MG, Goodwin GM, Frisoni GB, Smith SM, Matthews PM, Beckmann CF, Mackay CE (2009) Distinct patterns of brain activity in young carriers of the APOE-epsilon4 allele. *Proc Natl Acad Sci U S A* 106:7209-7214.
- Fleisher AS, Sherzai A, Taylor C, Langbaum JB, Chen K, Buxton RB (2009) Resting-state BOLD networks versus task-associated functional MRI for distinguishing Alzheimer's disease risk groups. *Neuroimage* 47:1678-1690.
- Flicker L (2010) Modifiable lifestyle risk factors for Alzheimer's disease. *J Alzheimers Dis* 20:803-811.
- Fox MD, Raichle ME (2007) Spontaneous fluctuations in brain activity observed with functional magnetic resonance imaging. *Nat Rev Neurosci* 8:700-711.
- Fox MD, Snyder AZ, Vincent JL, Corbetta M, Van Essen DC, Raichle ME (2005) The human brain is intrinsically organized into dynamic, anticorrelated functional networks. *Proc Natl Acad Sci U S A* 102:9673-9678.
- Franklin KB, Paxinos G (1996) *The Mouse Brain in Stereotaxic Coordinates*, 1st Edition. San Diego: Academic Press.
- Garcia-Alloza M, Dodwell SA, Meyer-Luehmann M, Hyman BT, Bacskai BJ (2006) Plaque-derived oxidative stress mediates distorted neurite trajectories in the Alzheimer mouse model. *J Neuropathol Exp Neurol* 65:1082-1089.
- Garcia-Alloza M, Subramanian M, Thyssen D, Borrelli LA, Fauq A, Das P, Golde TE, Hyman BT, Bacskai BJ (2009) Existing plaques and neuritic abnormalities in APP:PS1 mice are not affected by administration of the gamma-secretase inhibitor LY-411575. *Mol Neurodegener* 4:19.
- Gilestro GF, Togni G, Cirelli C (2009) Widespread changes in synaptic markers as a function of sleep and wakefulness in *Drosophila*. *Science* 324:109-112.

- Goate A, Chartier-Harlin MC, Mullan M, Brown J, Crawford F, Fidani L, Giuffra L, Haynes A, Irving N, James L, et al. (1991) Segregation of a missense mutation in the amyloid precursor protein gene with familial Alzheimer's disease. *Nature* 349:704-706.
- Goedert M (1987) Neuronal localization of amyloid beta protein precursor mRNA in normal human brain and in Alzheimer's disease. *EMBO J* 6:3627-3632.
- Goldstein ME, Cao Y, Fiedler T, Toyn J, Iben L, Barten DM, Pierdomenico M, Corsa J, Prasad CV, Olson RE, Li YW, Zaczek R, Albright CF (2007) Ex vivo occupancy of gamma-secretase inhibitors correlates with brain beta-amyloid peptide reduction in Tg2576 mice. *J Pharmacol Exp Ther* 323:102-108.
- Gordon MN, Holcomb LA, Jantzen PT, DiCarlo G, Wilcock D, Boyett KW, Connor K, Melachrinou J, O'Callaghan JP, Morgan D (2002) Time course of the development of Alzheimer-like pathology in the doubly transgenic PS1+APP mouse. *Exp Neurol* 173:183-195.
- Greicius MD, Srivastava G, Reiss AL, Menon V (2004) Default-mode network activity distinguishes Alzheimer's disease from healthy aging: evidence from functional MRI. *Proc Natl Acad Sci U S A* 101:4637-4642.
- Grimwood S, Hogg J, Jay MT, Lad AM, Lee V, Murray F, Peachey J, Townend T, Vithlani M, Beher D, Shearman MS, Hutson PH (2005) Determination of guinea-pig cortical gamma-secretase activity ex vivo following the systemic administration of a gamma-secretase inhibitor. *Neuropharmacology* 48:1002-1011.
- Haass C, Schlossmacher MG, Hung AY, Vigo-Pelfrey C, Mellon A, Ostaszewski BL, Lieberburg I, Koo EH, Schenk D, Teplow DB, et al. (1992) Amyloid beta-peptide is produced by cultured cells during normal metabolism. *Nature* 359:322-325.
- Hagmann P, Cammoun L, Gigandet X, Meuli R, Honey CJ, Wedeen VJ, Sporns O (2008) Mapping the structural core of human cerebral cortex. *PLoS Biol* 6:e159.
- Hansson O, Zetterberg H, Buchhave P, Londos E, Blennow K, Minthon L (2006) Association between CSF biomarkers and incipient Alzheimer's disease in patients with mild cognitive impairment: a follow-up study. *Lancet neurology* 5:228-234.
- Hardy J, Selkoe DJ (2002) The amyloid hypothesis of Alzheimer's disease: progress and problems on the road to therapeutics. *Science* 297:353-356.
- Harigaya Y, Tomidokoro Y, Ikeda M, Sasaki A, Kawarabayashi T, Matsubara E, Kanai M, Saido TC, Younkin SG, Shoji M (2006) Type-specific evolution of amyloid plaque and angiopathy in APPsw mice. *Neurosci Lett* 395:37-41.
- Harris JA, Devidze N, Verret L, Ho K, Halabisky B, Thwin MT, Kim D, Hamto P, Lo I, Yu GQ, Palop JJ, Masliah E, Mucke L (2010) Transsynaptic progression of amyloid-beta-induced neuronal dysfunction within the entorhinal-hippocampal network. *Neuron* 68:428-441.
- Hasegawa K, Yamaguchi I, Omata S, Gejyo F, Naiki H (1999) Interaction between A beta(1-42) and A beta(1-40) in Alzheimer's beta-amyloid fibril formation in vitro. *Biochemistry* 38:15514-15521.
- Hedden T, Van Dijk KR, Becker JA, Mehta A, Sperling RA, Johnson KA, Buckner RL (2009) Disruption of functional connectivity in clinically normal older adults harboring amyloid burden. *J Neurosci* 29:12686-12694.

- Holcomb L, Gordon MN, McGowan E, Yu X, Benkovic S, Jantzen P, Wright K, Saad I, Mueller R, Morgan D, Sanders S, Zehr C, O'Campo K, Hardy J, Prada CM, Eckman C, Younkin S, Hsiao K, Duff K (1998) Accelerated Alzheimer-type phenotype in transgenic mice carrying both mutant amyloid precursor protein and presenilin 1 transgenes. *Nat Med* 4:97-100.
- Holtzman DM, Morris JC, Goate AM (2011) Alzheimer's disease: the challenge of the second century. *Science translational medicine* 3:77sr71.
- Hsiao K, Chapman P, Nilsen S, Eckman C, Harigaya Y, Younkin S, Yang F, Cole G (1996) Correlative memory deficits, A $\beta$  elevation, and amyloid plaques in transgenic mice. *Science* 274:99-102.
- Hyder F, Patel AB, Gjedde A, Rothman DL, Behar KL, Shulman RG (2006) Neuronal-glial glucose oxidation and glutamatergic-GABAergic function. *J Cereb Blood Flow Metab* 26:865-877.
- Hyman BT, Marzloff K, Arriagada PV (1993) The lack of accumulation of senile plaques or amyloid burden in Alzheimer's disease suggests a dynamic balance between amyloid deposition and resolution. *J Neuropathol Exp Neurol* 52:594-600.
- Irizarry MC, Locascio JJ, Hyman BT (2001) beta-site APP cleaving enzyme mRNA expression in APP transgenic mice: anatomical overlap with transgene expression and static levels with aging. *Am J Pathol* 158:173-177.
- Irizarry MC, McNamara M, Fedorchak K, Hsiao K, Hyman BT (1997) APPSw transgenic mice develop age-related A $\beta$  deposits and neuropil abnormalities, but no neuronal loss in CA1. *J Neuropathol Exp Neurol* 56:965-973.
- Jack CR, Jr., Wengenack TM, Reyes DA, Garwood M, Curran GL, Borowski BJ, Lin J, Preboske GM, Holasek SS, Adriany G, Poduslo JF (2005) In vivo magnetic resonance microimaging of individual amyloid plaques in Alzheimer's transgenic mice. *J Neurosci* 25:10041-10048.
- Jack CR, Jr., Lowe VJ, Weigand SD, Wiste HJ, Senjem ML, Knopman DS, Shiung MM, Gunter JL, Boeve BF, Kemp BJ, Weiner M, Petersen RC (2009) Serial PIB and MRI in normal, mild cognitive impairment and Alzheimer's disease: implications for sequence of pathological events in Alzheimer's disease. *Brain* 132:1355-1365.
- Jankowsky JL, Slunt HH, Gonzales V, Savonenko AV, Wen JC, Jenkins NA, Copeland NG, Younkin LH, Lester HA, Younkin SG, Borchelt DR (2005) Persistent amyloidosis following suppression of A $\beta$  production in a transgenic model of Alzheimer disease. *PLoS Med* 2:e355.
- Jankowsky JL, Fadale DJ, Anderson J, Xu GM, Gonzales V, Jenkins NA, Copeland NG, Lee MK, Younkin LH, Wagner SL, Younkin SG, Borchelt DR (2004) Mutant presenilins specifically elevate the levels of the 42 residue beta-amyloid peptide in vivo: evidence for augmentation of a 42-specific gamma secretase. *Hum Mol Genet* 13:159-170.
- Kamenetz F, Tomita T, Hsieh H, Seabrook G, Borchelt D, Iwatsubo T, Sisodia S, Malinow R (2003) APP processing and synaptic function. *Neuron* 37:925-937.
- Kang JE, Cirrito JR, Dong H, Csernansky JG, Holtzman DM (2007) Acute stress increases interstitial fluid amyloid-beta via corticotropin-releasing factor and neuronal activity. *Proc Natl Acad Sci U S A* 104:10673-10678.

- Kang JE, Lim MM, Bateman RJ, Lee JJ, Smyth LP, Cirrito JR, Fujiki N, Nishino S, Holtzman DM (2009) Amyloid-beta dynamics are regulated by orexin and the sleep-wake cycle. *Science* 326:1005-1007.
- Kawarabayashi T, Younkin LH, Saido TC, Shoji M, Ashe KH, Younkin SG (2001) Age-dependent changes in brain, CSF, and plasma amyloid (beta) protein in the Tg2576 transgenic mouse model of Alzheimer's disease. *J Neurosci* 21:372-381.
- Keene CS, Bucci DJ (2008) Neurotoxic lesions of retrosplenial cortex disrupt signaled and unsignaled contextual fear conditioning. *Behav Neurosci* 122:1070-1077.
- Keene CS, Bucci DJ (2009) Damage to the retrosplenial cortex produces specific impairments in spatial working memory. *Neurobiol Learn Mem* 91:408-414.
- Kim J, Basak JM, Holtzman DM (2009a) The role of apolipoprotein E in Alzheimer's disease. *Neuron* 63:287-303.
- Kim J, Onstead L, Randle S, Price R, Smithson L, Zwizinski C, Dickson DW, Golde T, McGowan E (2007) Abeta40 inhibits amyloid deposition in vivo. *J Neurosci* 27:627-633.
- Kim J, Castellano JM, Jiang H, Basak JM, Parsadanian M, Pham V, Mason SM, Paul SM, Holtzman DM (2009b) Overexpression of low-density lipoprotein receptor in the brain markedly inhibits amyloid deposition and increases extracellular A beta clearance. *Neuron* 64:632-644.
- Klunk WE, Bacskai BJ, Mathis CA, Kajdasz ST, McLellan ME, Frosch MP, Debnath ML, Holt DP, Wang Y, Hyman BT (2002) Imaging Abeta plaques in living transgenic mice with multiphoton microscopy and methoxy-X04, a systemically administered Congo red derivative. *J Neuropathol Exp Neurol* 61:797-805.
- Klunk WE et al. (2004) Imaging brain amyloid in Alzheimer's disease with Pittsburgh Compound-B. *Ann Neurol* 55:306-319.
- Knowles RB, Wyart C, Buldyrev SV, Cruz L, Urbanc B, Hasselmo ME, Stanley HE, Hyman BT (1999) Plaque-induced neurite abnormalities: implications for disruption of neural networks in Alzheimer's disease. *Proc Natl Acad Sci U S A* 96:5274-5279.
- Koffie RM, Meyer-Luehmann M, Hashimoto T, Adams KW, Mielke ML, Garcia-Alloza M, Micheva KD, Smith SJ, Kim ML, Lee VM, Hyman BT, Spires-Jones TL (2009) Oligomeric amyloid beta associates with postsynaptic densities and correlates with excitatory synapse loss near senile plaques. *Proc Natl Acad Sci U S A* 106:4012-4017.
- Kuchibhotla KV, Lattarulo CR, Hyman BT, Bacskai BJ (2009) Synchronous hyperactivity and intercellular calcium waves in astrocytes in Alzheimer mice. *Science* 323:1211-1215.
- Kuchibhotla KV, Goldman ST, Lattarulo CR, Wu HY, Hyman BT, Bacskai BJ (2008) Abeta plaques lead to aberrant regulation of calcium homeostasis in vivo resulting in structural and functional disruption of neuronal networks. *Neuron* 59:214-225.
- Lah JJ, Levey AI (2000) Endogenous presenilin-1 targets to endocytic rather than biosynthetic compartments. *Molecular and cellular neurosciences* 16:111-126.
- Lamb BT, Bardel KA, Kulnane LS, Anderson JJ, Holtz G, Wagner SL, Sisodia SS, Hoeger EJ (1999) Amyloid production and deposition in mutant amyloid precursor protein and presenilin-1 yeast artificial chromosome transgenic mice. *Nat Neurosci* 2:695-697.

- Lammich S, Kojro E, Postina R, Gilbert S, Pfeiffer R, Jasionowski M, Haass C, Fahrenholz F (1999) Constitutive and regulated alpha-secretase cleavage of Alzheimer's amyloid precursor protein by a disintegrin metalloprotease. *Proc Natl Acad Sci U S A* 96:3922-3927.
- Lammich S, Okochi M, Takeda M, Kaether C, Capell A, Zimmer AK, Edbauer D, Walter J, Steiner H, Haass C (2002) Presenilin-dependent intramembrane proteolysis of CD44 leads to the liberation of its intracellular domain and the secretion of an Abeta-like peptide. *J Biol Chem* 277:44754-44759.
- Lazarov O, Lee M, Peterson DA, Sisodia SS (2002) Evidence that synaptically released beta-amyloid accumulates as extracellular deposits in the hippocampus of transgenic mice. *J Neurosci* 22:9785-9793.
- Levy E, Carman MD, Fernandez-Madrid IJ, Power MD, Lieberburg I, van Duinen SG, Bots GT, Luyendijk W, Frangione B (1990) Mutation of the Alzheimer's disease amyloid gene in hereditary cerebral hemorrhage, Dutch type. *Science* 248:1124-1126.
- Li T, Wen H, Brayton C, Laird FM, Ma G, Peng S, Placanica L, Wu TC, Crain BJ, Price DL, Eberhart CG, Wong PC (2007) Moderate reduction of gamma-secretase attenuates amyloid burden and limits mechanism-based liabilities. *J Neurosci* 27:10849-10859.
- Lombardo JA, Stern EA, McLellan ME, Kajdasz ST, Hickey GA, Bacskai BJ, Hyman BT (2003) Amyloid-beta antibody treatment leads to rapid normalization of plaque-induced neuritic alterations. *J Neurosci* 23:10879-10883.
- Lopresti BJ, Klunk WE, Mathis CA, Hoge JA, Ziolkowski SK, Lu X, Meltzer CC, Schimmel K, Tsopelas ND, DeKosky ST, Price JC (2005) Simplified quantification of Pittsburgh Compound B amyloid imaging PET studies: a comparative analysis. *J Nucl Med* 46:1959-1972.
- Machulda MM, Jones DT, Vemuri P, McDade E, Avula R, Przybelski S, Boeve BF, Knopman DS, Petersen RC, Jack CR, Jr. (2011) Effect of APOE  $\epsilon$ 4 Status on Intrinsic Network Connectivity in Cognitively Normal Elderly Subjects. *Arch Neurol* 68:1131-1136.
- Melzer P, Van der Loos H, Dorfl J, Welker E, Robert P, Emery D, Berrini JC (1985) A magnetic device to stimulate selected whiskers of freely moving or restrained small rodents: its application in a deoxyglucose study. *Brain Res* 348:229-240.
- Meyer-Luehmann M, Spires-Jones TL, Prada C, Garcia-Alloza M, de Calignon A, Rozkalne A, Koenigsknecht-Talbot J, Holtzman DM, Bacskai BJ, Hyman BT (2008) Rapid appearance and local toxicity of amyloid-beta plaques in a mouse model of Alzheimer's disease. *Nature* 451:720-724.
- Meyer-Luehmann M, Stalder M, Herzig MC, Kaeser SA, Kohler E, Pfeifer M, Boncristiano S, Mathews PM, Mercken M, Abramowski D, Staufenbiel M, Jucker M (2003) Extracellular amyloid formation and associated pathology in neural grafts. *Nat Neurosci* 6:370-377.
- Meyer-Luehmann M, Coomaraswamy J, Bolmont T, Kaeser S, Schaefer C, Kilger E, Neuenschwander A, Abramowski D, Frey P, Jaton AL, Vigouret JM, Paganetti P, Walsh DM, Mathews PM, Ghiso J, Staufenbiel M, Walker LC, Jucker M (2006) Exogenous induction of cerebral beta-amyloidogenesis is governed by agent and host. *Science* 313:1781-1784.

- Mintun MA, Larossa GN, Sheline YI, Dence CS, Lee SY, Mach RH, Klunk WE, Mathis CA, DeKosky ST, Morris JC (2006) [<sup>11</sup>C]PIB in a nondemented population: potential antecedent marker of Alzheimer disease. *Neurology* 67:446-452.
- Morris JC, Roe CM, Xiong C, Fagan AM, Goate AM, Holtzman DM, Mintun MA (2010) APOE predicts amyloid-beta but not tau Alzheimer pathology in cognitively normal aging. *Ann Neurol* 67:122-131.
- Morris JC, Roe CM, Grant EA, Head D, Storandt M, Goate AM, Fagan AM, Holtzman DM, Mintun MA (2009) Pittsburgh compound B imaging and prediction of progression from cognitive normality to symptomatic Alzheimer disease. *Arch Neurol* 66:1469-1475.
- Ni CY, Murphy MP, Golde TE, Carpenter G (2001) gamma -Secretase cleavage and nuclear localization of ErbB-4 receptor tyrosine kinase. *Science* 294:2179-2181.
- Nitsch RM, Slack BE, Wurtman RJ, Growdon JH (1992) Release of Alzheimer amyloid precursor derivatives stimulated by activation of muscarinic acetylcholine receptors. *Science* 258:304-307.
- Nitsch RM, Farber SA, Growdon JH, Wurtman RJ (1993) Release of amyloid beta-protein precursor derivatives by electrical depolarization of rat hippocampal slices. *Proc Natl Acad Sci U S A* 90:5191-5193.
- Nordstedt C, Caporaso GL, Thyberg J, Gandy SE, Greengard P (1993) Identification of the Alzheimer beta/A4 amyloid precursor protein in clathrin-coated vesicles purified from PC12 cells. *J Biol Chem* 268:608-612.
- Olney JW, Wozniak DF, Farber NB (1997) Excitotoxic neurodegeneration in Alzheimer disease. New hypothesis and new therapeutic strategies. *Arch Neurol* 54:1234-1240.
- Page K, Hollister R, Tanzi RE, Hyman BT (1996) In situ hybridization analysis of presenilin 1 mRNA in Alzheimer disease and in lesioned rat brain. *Proc Natl Acad Sci U S A* 93:14020-14024.
- Pellerin L, Magistretti PJ (1994) Glutamate uptake into astrocytes stimulates aerobic glycolysis: a mechanism coupling neuronal activity to glucose utilization. *Proc Natl Acad Sci U S A* 91:10625-10629.
- Perrin RJ, Fagan AM, Holtzman DM (2009) Multimodal techniques for diagnosis and prognosis of Alzheimer's disease. *Nature* 461:916-922.
- Petersen SE, Fox PT, Posner MI, Mintun M, Raichle ME (1988) Positron emission tomographic studies of the cortical anatomy of single-word processing. *Nature* 331:585-589.
- Prahl S (2002) Optical Absorption of Hemoglobin. Oregon Laser Medical Center.
- Price JC, Klunk WE, Lopresti BJ, Lu X, Hoge JA, Ziolkowski SK, Holt DP, Meltzer CC, DeKosky ST, Mathis CA (2005) Kinetic modeling of amyloid binding in humans using PET imaging and Pittsburgh Compound-B. *J Cereb Blood Flow Metab* 25:1528-1547.
- Raichle ME, Mintun MA (2006) Brain work and brain imaging. *Annu Rev Neurosci* 29:449-476.
- Raichle ME, Snyder AZ (2007) A default mode of brain function: a brief history of an evolving idea. *Neuroimage* 37:1083-1090; discussion 1097-1089.
- Raichle ME, MacLeod AM, Snyder AZ, Powers WJ, Gusnard DA, Shulman GL (2001) A default mode of brain function. *Proc Natl Acad Sci U S A* 98:676-682.

- Reiman EM, Caselli RJ, Yun LS, Chen K, Bandy D, Minoshima S, Thibodeau SN, Osborne D (1996) Preclinical evidence of Alzheimer's disease in persons homozygous for the epsilon 4 allele for apolipoprotein E. *N Engl J Med* 334:752-758.
- Reiman EM, Chen K, Liu X, Bandy D, Yu M, Lee W, Ayutyanont N, Keppler J, Reeder SA, Langbaum JB, Alexander GE, Klunk WE, Mathis CA, Price JC, Aizenstein HJ, DeKosky ST, Caselli RJ (2009) Fibrillar amyloid-beta burden in cognitively normal people at 3 levels of genetic risk for Alzheimer's disease. *Proc Natl Acad Sci U S A* 106:6820-6825.
- Riedner BA, Vyazovskiy VV, Huber R, Massimini M, Esser S, Murphy M, Tononi G (2007) Sleep homeostasis and cortical synchronization: III. A high-density EEG study of sleep slow waves in humans. *Sleep* 30:1643-1657.
- Rojas MJ, Navas JA, Rector DM (2006) Evoked response potential markers for anesthetic and behavioral states. *Am J Physiol Regul Integr Comp Physiol* 291:R189-196.
- Saunders AM, Strittmatter WJ, Schmechel D, George-Hyslop PH, Pericak-Vance MA, Joo SH, Rosi BL, Gusella JF, Crapper-MacLachlan DR, Alberts MJ, et al. (1993) Association of apolipoprotein E allele epsilon 4 with late-onset familial and sporadic Alzheimer's disease. *Neurology* 43:1467-1472.
- Savonenko A, Xu GM, Melnikova T, Morton JL, Gonzales V, Wong MP, Price DL, Tang F, Markowska AL, Borchelt DR (2005) Episodic-like memory deficits in the APP<sup>swe</sup>/PS1<sup>dE9</sup> mouse model of Alzheimer's disease: relationships to beta-amyloid deposition and neurotransmitter abnormalities. *Neurobiol Dis* 18:602-617.
- Schenk D et al. (1999) Immunization with amyloid-beta attenuates Alzheimer-disease-like pathology in the PDAPP mouse. *Nature* 400:173-177.
- Selkoe DJ (2000) Toward a comprehensive theory for Alzheimer's disease. Hypothesis: Alzheimer's disease is caused by the cerebral accumulation and cytotoxicity of amyloid beta-protein. *Ann N Y Acad Sci* 924:17-25.
- Selkoe DJ (2001) Alzheimer's disease: genes, proteins, and therapy. *Physiol Rev* 81:741-766.
- Seubert P, Vigo-Pelfrey C, Esch F, Lee M, Dovey H, Davis D, Sinha S, Schlossmacher M, Whaley J, Swindlehurst C, et al. (1992) Isolation and quantification of soluble Alzheimer's beta-peptide from biological fluids. *Nature* 359:325-327.
- Sheline YI, Raichle ME, Snyder AZ, Morris JC, Head D, Wang S, Mintun MA (2010a) Amyloid plaques disrupt resting state default mode network connectivity in cognitively normal elderly. *Biol Psychiatry* 67:584-587.
- Sheline YI, Morris JC, Snyder AZ, Price JL, Yan Z, D'Angelo G, Liu C, Dixit S, Benzinger T, Fagan A, Goate A, Mintun MA (2010b) APOE4 allele disrupts resting state fMRI connectivity in the absence of amyloid plaques or decreased CSF Aβ<sub>42</sub>. *J Neurosci* 30:17035-17040.
- Sheng JG, Price DL, Koliatsos VE (2002) Disruption of corticocortical connections ameliorates amyloid burden in terminal fields in a transgenic model of Aβ<sub>42</sub> amyloidosis. *J Neurosci* 22:9794-9799.

- Shoji M, Golde TE, Ghiso J, Cheung TT, Estus S, Shaffer LM, Cai XD, McKay DM, Tintner R, Frangione B, et al. (1992) Production of the Alzheimer amyloid beta protein by normal proteolytic processing. *Science* 258:126-129.
- Sokoloff L, Mangold R, Wechsler RL, Kenney C, Kety SS (1955) The effect of mental arithmetic on cerebral circulation and metabolism. *J Clin Invest* 34:1101-1108.
- Sperling RA, Laviolette PS, O'Keefe K, O'Brien J, Rentz DM, Pihlajamaki M, Marshall G, Hyman BT, Selkoe DJ, Hedden T, Buckner RL, Becker JA, Johnson KA (2009) Amyloid deposition is associated with impaired default network function in older persons without dementia. *Neuron* 63:178-188.
- Stern EA, Bacskai BJ, Hickey GA, Attenello FJ, Lombardo JA, Hyman BT (2004) Cortical synaptic integration in vivo is disrupted by amyloid-beta plaques. *J Neurosci* 24:4535-4540.
- Sturchler-Pierrat C, Abramowski D, Duke M, Wiederhold KH, Mistl C, Rothacher S, Ledermann B, Burki K, Frey P, Paganetti PA, Waridel C, Calhoun ME, Jucker M, Probst A, Staufenbiel M, Sommer B (1997) Two amyloid precursor protein transgenic mouse models with Alzheimer disease-like pathology. *Proc Natl Acad Sci U S A* 94:13287-13292.
- Sunderland T, Mirza N, Putnam KT, Linker G, Bhupali D, Durham R, Soares H, Kimmel L, Friedman D, Bergeson J, Csako G, Levy JA, Bartko JJ, Cohen RM (2004) Cerebrospinal fluid beta-amyloid1-42 and tau in control subjects at risk for Alzheimer's disease: the effect of APOE epsilon4 allele. *Biol Psychiatry* 56:670-676.
- Supekar K, Menon V, Rubin D, Musen M, Greicius MD (2008) Network analysis of intrinsic functional brain connectivity in Alzheimer's disease. *PLoS Comput Biol* 4:e1000100.
- Takata K, Kitamura Y, Yanagisawa D, Morikawa S, Morita M, Inubushi T, Tsuchiya D, Chishiro S, Saeki M, Taniguchi T, Shimohama S, Tooyama I (2007) Microglial transplantation increases amyloid-beta clearance in Alzheimer model rats. *FEBS Lett* 581:475-478.
- Terry RD, Masliah E, Salmon DP, Butters N, DeTeresa R, Hill R, Hansen LA, Katzman R (1991) Physical basis of cognitive alterations in Alzheimer's disease: synapse loss is the major correlate of cognitive impairment. *Ann Neurol* 30:572-580.
- Thies W, Bleiler L (2011) 2011 Alzheimer's disease facts and figures. *Alzheimer's & dementia : the journal of the Alzheimer's Association* 7:208-244.
- Tsai J, Grutzendler J, Duff K, Gan WB (2004) Fibrillar amyloid deposition leads to local synaptic abnormalities and breakage of neuronal branches. *Nat Neurosci* 7:1181-1183.
- Uehara T, Sumiyoshi T, Itoh H, Kurata K (2008) Lactate production and neurotransmitters; evidence from microdialysis studies. *Pharmacol Biochem Behav* 90:273-281.
- Vaishnavi SN, Vlassenko AG, Rundle MM, Snyder AZ, Mintun MA, Raichle ME (2010) Regional aerobic glycolysis in the human brain. *Proc Natl Acad Sci U S A* 107:17757-17762.
- Van Broeckhoven C, Haan J, Bakker E, Hardy JA, Van Hul W, Wehnert A, Vegter-Van der Vlis M, Roos RA (1990) Amyloid beta protein precursor gene and hereditary cerebral hemorrhage with amyloidosis (Dutch). *Science* 248:1120-1122.

- Vassar R et al. (1999) Beta-secretase cleavage of Alzheimer's amyloid precursor protein by the transmembrane aspartic protease BACE. *Science* 286:735-741.
- Vlassenko AG, Vaishnavi SN, Couture L, Sacco D, Shannon BJ, Mach RH, Morris JC, Raichle ME, Mintun MA (2010) Spatial correlation between brain aerobic glycolysis and amyloid-beta (A $\beta$ ) deposition. *Proc Natl Acad Sci U S A* 107:17763-17767.
- Vyazovskiy VV, Cirelli C, Tononi G, Tobler I (2008a) Cortical metabolic rates as measured by 2-deoxyglucose-uptake are increased after waking and decreased after sleep in mice. *Brain Res Bull* 75:591-597.
- Vyazovskiy VV, Cirelli C, Pfister-Genskow M, Faraguna U, Tononi G (2008b) Molecular and electrophysiological evidence for net synaptic potentiation in wake and depression in sleep. *Nat Neurosci* 11:200-208.
- Wang C, Wilson WA, Moore SD, Mace BE, Maeda N, Schmechel DE, Sullivan PM (2005) Human apoE4-targeted replacement mice display synaptic deficits in the absence of neuropathology. *Neurobiol Dis* 18:390-398.
- Wei W, Nguyen LN, Kessels HW, Hagiwara H, Sisodia S, Malinow R (2010) Amyloid beta from axons and dendrites reduces local spine number and plasticity. *Nat Neurosci* 13:190-196.
- Wengenack TM, Whelan S, Curran GL, Duff KE, Poduslo JF (2000) Quantitative histological analysis of amyloid deposition in Alzheimer's double transgenic mouse brain. *Neuroscience* 101:939-944.
- West HL, Rebeck GW, Hyman BT (1994) Frequency of the apolipoprotein E epsilon 2 allele is diminished in sporadic Alzheimer disease. *Neurosci Lett* 175:46-48.
- White BR, Bauer AQ, Snyder AZ, Schlaggar BL, Lee JM, Culver JP (2011) Imaging of functional connectivity in the mouse brain. *PLoS One* 6:e16322.
- White BR, Snyder AZ, Cohen AL, Petersen SE, Raichle ME, Schlaggar BL, Culver JP (2009) Resting-state functional connectivity in the human brain revealed with diffuse optical tomography. *Neuroimage* 47:148-156.
- Wilcock DM, DiCarlo G, Henderson D, Jackson J, Clarke K, Ugen KE, Gordon MN, Morgan D (2003) Intracranially administered anti-A $\beta$  antibodies reduce beta-amyloid deposition by mechanisms both independent of and associated with microglial activation. *J Neurosci* 23:3745-3751.
- Wilcock DM, Rojiani A, Rosenthal A, Levkowitz G, Subbarao S, Alamed J, Wilson D, Wilson N, Freeman MJ, Gordon MN, Morgan D (2004) Passive amyloid immunotherapy clears amyloid and transiently activates microglia in a transgenic mouse model of amyloid deposition. *J Neurosci* 24:6144-6151.
- Wong GT, Manfra D, Poulet FM, Zhang Q, Josien H, Bara T, Engstrom L, Pinzon-Ortiz M, Fine JS, Lee HJ, Zhang L, Higgins GA, Parker EM (2004) Chronic treatment with the gamma-secretase inhibitor LY-411,575 inhibits beta-amyloid peptide production and alters lymphopoiesis and intestinal cell differentiation. *J Biol Chem* 279:12876-12882.
- Woolsey TA, Van der Loos H (1970) The structural organization of layer IV in the somatosensory region (SI) of mouse cerebral cortex. The description of a cortical field composed of discrete cytoarchitectonic units. *Brain Res* 17:205-242.

- Wyss-Coray T, Loike JD, Brionne TC, Lu E, Anankov R, Yan F, Silverstein SC, Husemann J (2003) Adult mouse astrocytes degrade amyloid-beta in vitro and in situ. *Nat Med* 9:453-457.
- Wyss JM, Van Groen T (1992) Connections between the retrosplenial cortex and the hippocampal formation in the rat: a review. *Hippocampus* 2:1-11.
- Xu HT, Pan F, Yang G, Gan WB (2007) Choice of cranial window type for in vivo imaging affects dendritic spine turnover in the cortex. *Nat Neurosci* 10:549-551.
- Yan P, Bero AW, Cirrito JR, Xiao Q, Hu X, Wang Y, Gonzales E, Holtzman DM, Lee JM (2009) Characterizing the appearance and growth of amyloid plaques in APP/PS1 mice. *J Neurosci* 29:10706-10714.
- Yoshiyama Y, Higuchi M, Zhang B, Huang SM, Iwata N, Saito TC, Maeda J, Suhara T, Trojanowski JQ, Lee VM (2007) Synapse loss and microglial activation precede tangles in a P301S tauopathy mouse model. *Neuron* 53:337-351.
- Zhang D, Raichle ME (2010) Disease and the brain's dark energy. *Nature reviews Neurology* 6:15-28.
- Zhang HY, Wang SJ, Xing J, Liu B, Ma ZL, Yang M, Zhang ZJ, Teng GJ (2009) Detection of PCC functional connectivity characteristics in resting-state fMRI in mild Alzheimer's disease. *Behav Brain Res* 197:103-108.